END WINDING COOLING IN ELECTRIC MACHINES

Christopher Micallef, BEng (Hons)

Thesis submitted to the University of Nottingham
for the degree of Doctor of Philosophy

September 2006

Abstract

The fluid flow field and temperature distribution within the end region of a Totally Enclosed Fan Cooled (TEFC) induction motor have been investigated both experimentally and using Computational Fluid Dynamics (CFD) techniques, in order to improve the thermal performance.

The flow field and the distribution of heat transfer coefficients over the end windings and internal surfaces (mainly frame and end shield) are characterised for a typical end region configuration. This is then used as a base case in order to investigate the impact configuration changes have on the fluid flow field and heat transfer characteristics in the end region of TEFC induction motors. Common parameters governing the flow field inside the end region are varied, allowing recommendations for improved design and further research recommendations to be made.

CFD techniques are successfully applied to model the end region, including the copper where the heat generated is a function of temperature. Through these numerical techniques a good understanding of the flow field was made possible which enabled the author to propose and test configuration changes which improve the heat transfer characteristics in the region. These changes were validated experimentally.

Acknowledgements

I would like to thank my supervisors, Dr. Stephen Pickering, Dr Kathy Simmons and Dr Keith Bradley, for their guidance and encouragement throughout the duration of the PhD.

The financial support provided by the International Office at the University of Nottingham and the Office of Human Resources at the University of Malta is kindly acknowledged.

I would also like to thank my friends and colleagues I met at the University of Nottingham, who made the duration of my studies enjoyable.

Last, but not least, I give my special thanks to my wife and my daughter for their support and love during the years of my study in the UK.

Table of contents

Nomenclature

A	Area (m^2)
h	Convective heat transfer coefficient $\left(W/m^2K\right)$
k	Turbulent kinetic energy per unit mass $\left(m^2/s^2\right)$
$\hat{n}$	Unit vector perpendicular to a surface
P	Pressure (Pa)
q	Heat flow (W)
Q''	Heat flux $\left(W/m^2\right)$
R	Thermal resistance $\left(K/W\right)$
t	Time (s)
T	Temperature (K)
u_τ	Shear velocity $\left(m/s\right)$
u^+	Dimensionless velocity parallel to wall
v	Velocity $\left(m/s\right)$
x	Length (m)
y	Length (m)
y^+	Dimensionless distance from wall
α	Thermal conductivity $\left(W/mK\right)$
ε	Turbulent dissipation rate $\left(m^2/s^3\right)$
μ	Dynamic viscosity $\left(kg/ms\right)$

ν_t Turbulent kinematic viscosity $\left(m^2/s\right)$

ϖ_i Absolute uncertainty in ‘i’

ρ Density $\left(kg/m^3\right)$

τ_w Shear stress at wall (Pa)

ω Specific turbulent dissipation rate $\left(1/s\right)$

1 Introduction

Electric motors and generators in general and induction machines in particular are becoming more compact due to competitive pressures. The smaller these machines get the greater the heat densities they will generate. Nowadays, with the advancement of power electronics, induction machines are being driven by means of variable speed drive units and this presents an additional heat source due to the harmonics supplied by the inverter. When such machines are operated at low speed the cooling performance is further jeopardised since the effectiveness of any internal fans is highly decreased. All of these factors lead to a temperature rise in the machine which will greatly effect its performance and life expectancy.

1.1 Problem Identification

As electrical motors and generators become smaller, the heat densities increase leading to higher temperature gradients. In induction machines, insulation breakdown is likely to be the problem associated with high temperatures. This problem may be tackled by either improving the insulation material and allowing the temperatures to rise or by improving the cooling performance of the windings and limiting the maximum temperature. In recent years the insulation materials have been improved considerably, and a point has been reached where no additional feasible gain can be achieved by further improvement of the insulation material. Consequently, this work will investigate methods to limit the temperature by improving the cooling performance of the windings.

1.2 Construction of Induction Motors

The major components of a typical induction motor are illustrated in Figure 1.1. The configuration shown in this figure is referred to as a *totally enclosed fan cooled* (TEFC) induction motor since the internal parts are totally isolated from the air surrounding the motor. This is done in order to avoid foreign object damage and contamination of the internal parts. The motor is cooled down by blowing air over the external surfaces of the frame using an external cooling fan arrangement.

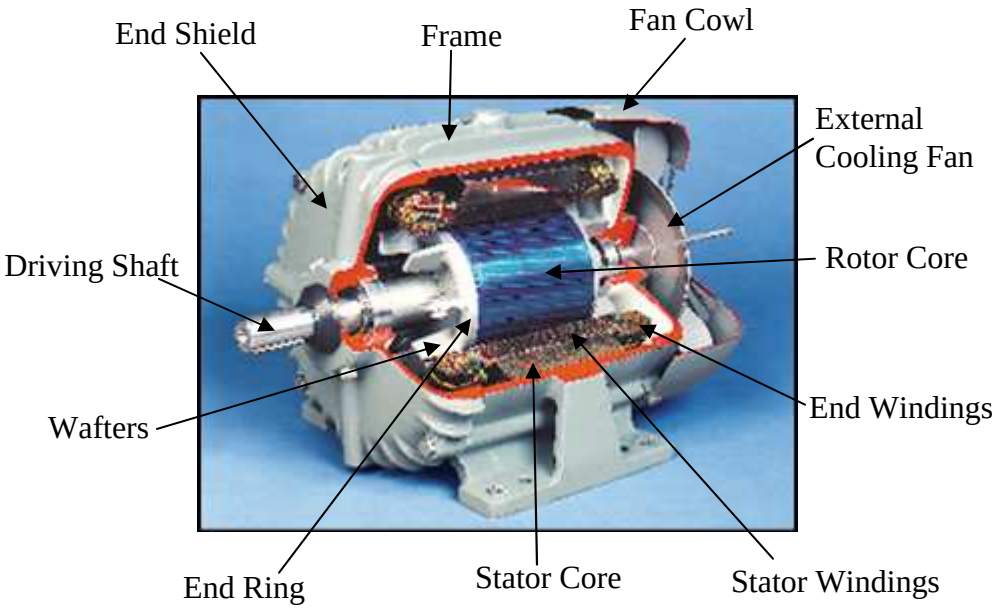

Figure 1.1 – Components of a typical induction motor taken from [1]

The other standard induction motor configuration is “through ventilated” and in this case air is forced to flow through the electrical motor in order to enhance cooling. Generally the only significant differences in the construction of these two machine configurations are inlet and outlet ports in the end shields and ducts in the rotor and the stator to allow air to flow through in the through-ventilated case.

1.3 Losses in Electrical Machines

The heat generated inside the motor originates from two main sources; mechanical and electrical losses. The mechanical losses include frictional losses generated by the bearings as well as windage losses. The electrical losses include the copper losses in the windings (heating effect due to copper resistance) and magnetic losses in the cores, also referred to as core losses (magnetic hysteresis and eddy currents in iron cores).

There are three ways in which heat is transferred from one body to another. These are conduction, convection and radiation. In electric motors the former two dominate over the latter one and therefore the heat flowing through radiation is usually neglected.

In one dimension, conduction is governed by the relation,

$$q = -\alpha A \frac{dT}{dx} \qquad (1.1)$$

and convection in fluids is governed by the relation,

$$q = hA(\Delta T) \qquad (1.2)$$

Figure 1.2 illustrates the major thermal flow paths present in a typical induction motor where the major heat flow routes are illustrated. Some of the heat generated by the rotor core and rotor bars flows through the shaft by conduction. The rest of the heat generated by the rotor core and rotor bars is dissipated by convection to the air surrounding the end region and to the stator through the rotor-stator air gap.

The heat generated by the stator core and stator windings flows to the frame. The heat generated by the end windings has two flow routes. One route travels along the winding copper to the stator while the other route dissipates the heat generated by the end windings to the air surrounding the end region. All the heat flowing to the air surrounding the end region is dissipated through the frame and end shields. The air flowing to the frame and end shields is then dissipated to the ambient generally via forced convection by means of an exterior fan arrangement. Bearing and windage power loss have been omitted from Figure 1.2.

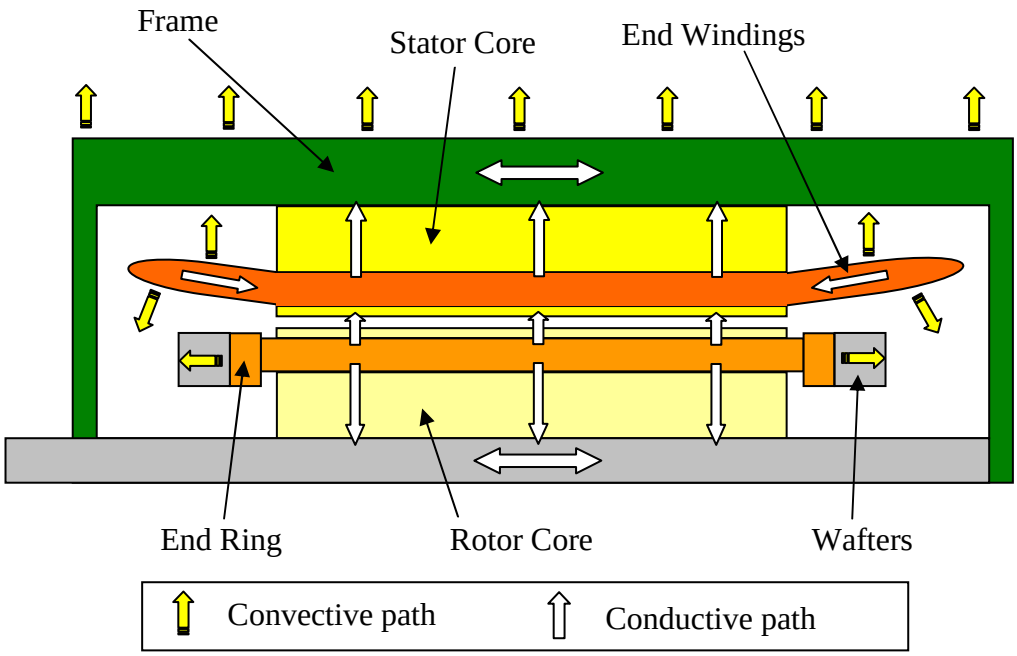

Figure 1.2 – Major thermal flow paths

Usually conduction paths offer less resistance to heat flow than convection paths and so heat transfer by conduction dominates. Additionally, in the case of induction motors, the thermal conductance of the stator core (being made out of insulated laminations) is much higher in the radial direction than it is in the axial direction. For these reasons, the bulk of the heat generated by the electric motor

flows in the radial direction through the stator core. The limiting resistance in the conduction paths is usually the contact thermal resistance between different components (e.g. windings to stator core and stator core to frame), but this is still much lower than the thermal resistance offered by the convective paths.

In motors having long end windings (such as 2-pole induction motors where the amount of copper in the end winding may be half that present in the whole stator winding), the heat generated in the end windings can be substantial. This heat flows to the surrounding end region fluid via convection and to the stator core via conduction. However due to the increased length of the end windings, the temperature difference along the end windings can be large. Hot spots in the end windings may result which if not addressed may lead to insulation breakdown in the end windings. Therefore the convective path plays a major role in such motors and this is the subject of this thesis.

1.4 Objectives of this investigation

The aim of this work is to investigate end winding cooling with a view to identify design changes to the end region that have potential to lead to reduced temperatures and the elimination of hot spots.

This study follows on from an earlier study by Mugglestone[2] in which the basic flow patterns in the end region of a TEFC induction motor were identified. Computational and experimental approaches were applied, but a limitation of that work was that the driving factors for the basic flow patterns were not clearly identified. Consequently the study did not provide the necessary level of

understanding required if heat transfer from the end windings to the end region is to be enhanced.

There are two objectives of this work:

1. To carry out a CFD and experimental study to investigate the air flow patterns in the end region of a large TEFC induction motor in order to further basic understanding of the fluid's behaviour by identifying the driving factors.

2. Using CFD, to model a number of modified end region configurations and assess which give improved heat transfer performance in the end region. CFD was chosen for this part of the work as a substantial number of different end region configurations were investigated and neither the time nor the budget were available for a full experimental study.

1.5 Structure of thesis

The work described in this thesis is put into context with the work of others via a literature survey presented in Chapter 2. The experimental test rig used for validation is described in Chapter 3 and in Chapter 4 the basic theory behind computational fluid dynamics is presented together with special techniques used in modelling electric motors.

The main study consists of three parts:

1. In the first part, a CFD model of the non-connection end of a 2-pole high voltage induction motor was validated by experiment. This is described in Chapter 5.

2. The second part of this work, which is detailed in Chapter 6, was an investigation of how changes in simple CFD models representing the end region of TEFC induction motors affected the flow field and heat transfer characteristics in the region. This was done using only CFD modelling techniques since enough confidence had been gained through the validation exercise performed earlier to make further experimental work unnecessary. This part of the study highlighted important features worth considering when designing end regions of TEFC induction motors.

3. In Chapter 7, the final part of this work is presented. The effects on flow behavior and heat transfer of configuration changes to the existing 2-pole end region model utilized previously were investigated. Additionally comments and suggestions are presented for future design considerations. The final CFD results were also verified by experiment, and details are included in Chapter 7.

General conclusions and recommendations for further work are finally given in Chapter 8.

2 Literature Review

The published literature on thermal analysis of electrical machines is reviewed in this chapter. The review concentrates on literature covering fluid flow and heat transfer in the end region of electrical machines.

2.1 Thermal design of electric motors.

The design process for electric motors and generators involves a series of both electrical and mechanical analyses, such as magnetic, electrical, stress and thermal analysis.

Thermal analysis is usually performed using either the resistance network method or the finite element method. Both of these methods will be described in some detail later in this chapter. Thermal analysis predicts temperatures the individual motor components will attain under maximum operating power (steady state analysis). If an unsteady state thermal analysis is performed (such as overloading the motor for a specific period of time), it can also predict the temperature transients. This is very useful especially when designing a process requiring cyclic loading of the motor where an under-rated motor might be a cheaper option. As highlighted in Section 1.3, temperature is a very important variable in motor design which needs to be limited to a certain value dictated by the insulation material in order to guarantee the life expectancy of the motor or generator.

2.1.1 Resistance networks

The majority of papers on thermal aspects of electrical machines use resistance network methods [1, 3, 4, 5, 6, 7]. This technique employs a network of nodes representing each individual motor component connected by thermal resistances and thermal capacitors (for unsteady state analysis). If the component the node represents generates heat (such as windings, core, etc) a heat sources is applied to that node. This thermal network is able to predict the heat flow and temperature distribution in the electrical motor under investigation. An example is shown in Figure 2.1 in which a number of nodes are depicted representing the various parts of an induction motor taken from the commercially available software MotorCAD™.

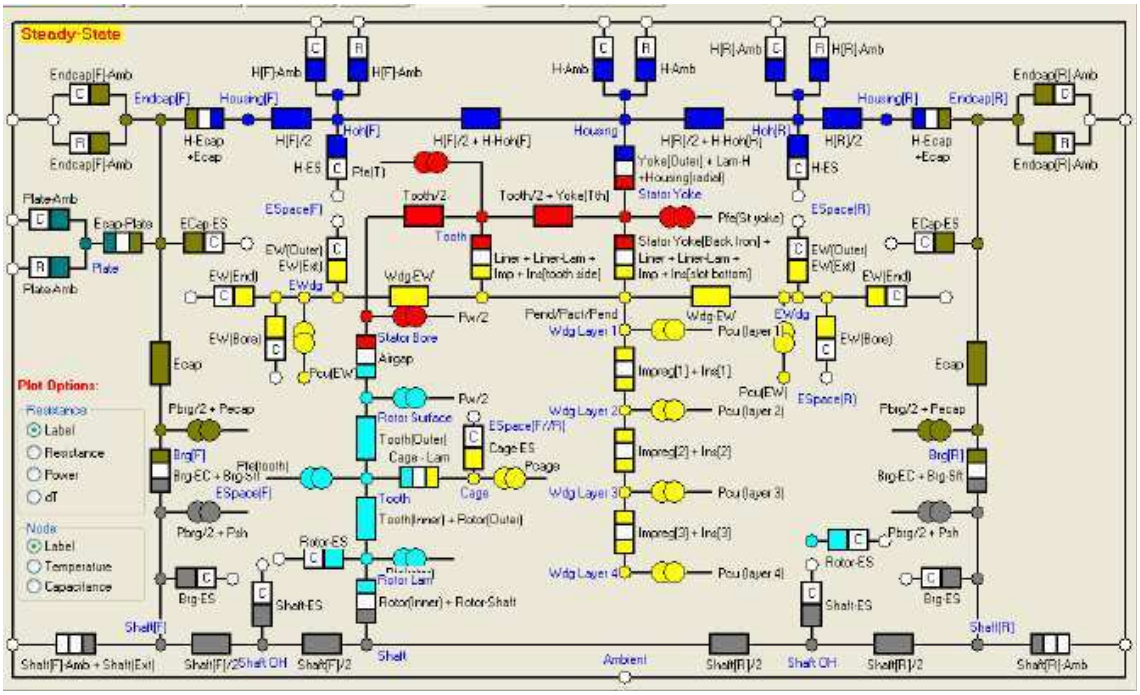

Figure 2.1 - Typical resistance network of an induction motor using Motor-CAD™

Material properties and dimensional characteristics are used to arrive at the conductive resistances and capacitances. Contact thermal resistances (the resistance to heat flow due to the interface between two solids) depend to a great extent on the contact pressure and are therefore more prone to errors. The thermal conductivity of the cores is highly anisotropic due to their laminated nature and the thermal conductivity of the cores in the axial direction is usually calculated by multiplying the thermal conductivity of the cores in the radial direction by a stacking factor (constant less than unity).

The heat transfer coefficients of the convective resistances are either assumed or estimated using published correlations which will be highlighted later on in this chapter. The errors involved here can be quite substantial. However it has been shown through various sensitivity analyses [4, 7] that the influence of these errors on the final results is negligible. Consequently, given that all the information is readily available, a thermal circuit may be solved. If the estimated thermal resistances are accurate enough, the results obtained from this kind of thermal analysis are sufficiently accurate.

The resistance network method is very simple to implement. It requires very little computer resources and any personal computer can do the job. The drawback this method has is that the individual components (each node) are treated as homogenous, and so their temperature is constant all over. In order to arrive at a more detailed analysis, components are usually sub divided into smaller sections in order to be able to resolve to some detail the temperature distribution in the

component itself. Additional nodes in the network provide greater detail. However the complexity of the model increases rapidly with increasing number of nodes.

2.1.2 Finite Element Methods (FEM)

More recently, with the advancement of computers, Finite Element Methods (FEM) have also been employed [3, 8]. FEM divides a solid model into small elements and solves the conduction heat flow equation at each individual element. This usually requires a dedicated software and highly trained users.

FEMs give a more detailed thermal solution, since different parts of the electrical machine are not considered to be homogenous. It requires more computing power and time. Finite Element Analysis (FEA) of electrical machines still requires the user to input values for the convective and conductive terms. Since the error involved in these constants can be considerable, the fine details obtained from such models are correspondingly uncertain. This is one of the reasons why electric motor manufacturers still prefer the resistance network method rather than finite element methods.

2.1.3 CFD Techniques

To date, the only computational method available to accurately predict the convective heat transfer coefficients over surfaces is CFD. This usually employs a finite volume method. CFD techniques solve the set of non linear partial differential equations governing the fluid and heat flow (commonly known as the complete Navier-Stokes equations, refer to chapter 4) in order to arrive at a flow

field. Like FEM, CFD techniques usually require complex software and highly trained users. Such software is even more computationally demanding than FEM and is therefore usually employed to investigate small components of the motor such as the end region or stator/rotor channels rather than the whole motor.

The available literature relevant to the application of CFD to electrical motors addresses only small regions of the electric motor in particular the heat transfer in the end region [9, 10, 11]. This is due to the complexity of the region which makes accurate information regarding associated thermal constants difficult to determine. More recently papers detailing the whole motor have started to appear [12, 13, 14] although such papers still use crude modeling assumptions (such as impermeable material representing the end windings).

2.2 Experimental measurements of heat transfer and air flow in the end region of electrical machines.

Generally thermal models of electrical machines are validated through experiments [4, 1, 6, 7, 8, 9, 10, 11, 13, 14]. Numerous papers have been published detailing experimental work on the thermal aspects of electrical machines. All individual components of the electrical machine have been thermally investigated in some detail. A lot of effort was put on the heat flow on the outside surface of the frame since this is thermally the most critical part [15, 16, 17]. It is recognized, however, that the heat transfer in the end region is the most difficult to predict and understand. The rest of this section will only review papers related to fluid flow and heat transfer in the end region of induction motors.

In the late 1960s, Roberts [18], measured thermal conductivities of laminations and electrical insulation. Heat transfer coefficients in air ducts were also measured. A very brief paragraph was dedicated to the heat transfer coefficient over the end windings. A value of 38.8W/m^{2}K for the mean overall heat transfer coefficient of the end winding was reported. This value was compared to the value of the heat transfer coefficient by natural convection from a plane wall (43W/m^{2}K). Thus it was concluded that the heat transfer over the end winding was largely controlled by natural convection. These values were validated on a thermal model of the stator of large electrical machines and were reported to yield reasonably reliable results. The motors under test are described as being large high voltage electrical machines, the type and size of motors these tests were performed on are not detailed.

Zautner et al. [19] investigated the optimum length of the cooling wafters in the squirrel cage rotor of an explosion proof induction motor (200kW; 6000V; 23.8A; 3000 rpm). It was suggested that in high speed induction motors, since the end windings are generally very long, around sixty nine percent of the copper losses are concentrated on the end windings. The maximum temperature rise in the windings was always located in the middle section of the stator winding just below the wedge (refer to Figure 2.2 below). The quoted thermal conductance of the end sections was in the range of 40W/K to 85W/K depending on the length of the wafters. The windage losses (and thus additional heat input) increased very rapidly for wafter lengths in the range 10mm to 30mm. One of the main conclusions was that the internal ventilation losses exceeds all other losses in this particular motor

and thus plays a major role in the temperature rise of the machine. These windage losses have to be taken into account in the thermal model of the machine. Additionally it was found that there exists a precise optimum length of wafters providing minimum temperature rise on the machine windings. A very interesting point from this work is the effect that wafter length has on the temperature distribution across the stator winding. There is an optimum wafter length corresponding to minimum temperature gradients over the depth of the slot (refer to Figure 2.2 below).

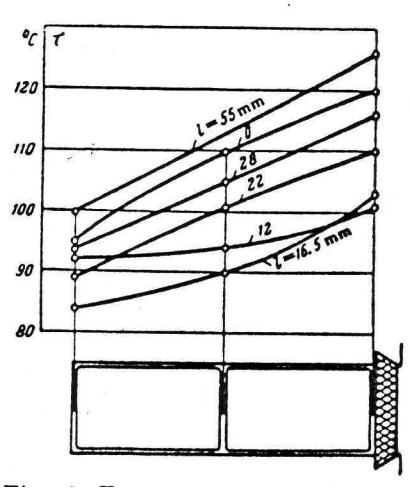

Figure 2.2 - Temperature rise distribution over depth of slot in continuous duty for various wafter lengths l [19]

Schubert [20] investigated the heat transfer coefficients at the end windings and the bearing cover of enclosed machines. The correlations resulting from these experiments were:

$$h_{EndWinding} = 15 + 6v^{0.9} \qquad (3.1)$$

$$h_{BearingCover} = 20 + 8.5v^{0.7} \qquad (3.2)$$

where *v* refers to the peripheral velocity of the rotor vanes. It was proposed that eighty percent of the heat losses flow radially to the housing. The rest flows axially to the bearing covers. It was reported that the number of wafters had no effect on the heat transfer coefficients despite increased air recirculation in the end region. The corresponding heat transfer coefficients were highly dependent on the length of the wafters. When the wafters were extended close to the bearing cover, the heat transfer coefficient on the bearing cover increased considerably, but the heat transfer coefficients on the end winding were decreased. In concluding the author proposed that heat transfer coefficients depend on the motor construction and thus may differ from one machine to the other, and that thermal analysis of electrical machines is much more sensitive to radial coefficients than axial coefficients.

Pickering et al.[21, 22, 23] published a series of papers investigating the heat transfer in different end winding configurations.

Pickering et al. [21] investigated the heat transfer in a C280M through ventilated 4-pole strip wound induction motor. The main finding was that the overall end winding heat transfer coefficients on the fan end were much higher than those at the inlet end (326W/m^2K and 210W/m^2K respectively based on winding envelope area). A substantial temperature variation on the end windings was identified. With an inlet air temperature of 25.3^{o}C, the inlet end end winding surface temperature varied from 28.9^{o}C to 36.2^{o}C. At the fan end the corresponding range was 32.4^{o}C to 42.1^{o}C. The circumferential temperature variation was in the order of 2^{o}C which is quite significant compared to surface to air temperature

differences. The local heat transfer coefficients varied along the end winding (refer to Figure 2.3). The highest heat transfer coefficient was recorded at the side of the straight part of the end winding (the part coming out of the stator core) next to the rotor bar extensions (386W/m^{2}K). The local heat transfer coefficients experienced a gradual decline along the end winding surface (from front lower part to back lower part of the end windings) with the minimum heat transfer recorded being around 58W/m^{2}K. The heat transfer coefficients varied with the relationship (motor speed)$^{0.75}$. Removal of the wafters resulted in a thirty percent increase in the overall heat transfer coefficient at the fan end and a corresponding thirty percent decrease in the heat transfer coefficient at the inlet end. Therefore it was argued that the wafters are beneficial at the inlet end.

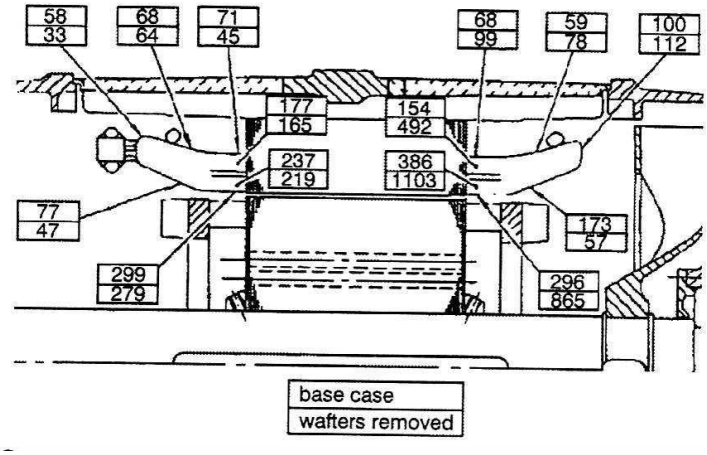

Figure 2.3 - Effect of wafter removal on local end winding heat transfer coefficients (W/m^{2}K) [21]

Another paper by the same authors [22] investigated the heat transfer from the stator end windings of a low voltage lap-wound electric motor, at different speeds, using different wafter lengths and including air guides near the end windings. The motor used in the tests was a C280M with a C280S core. The overall heat transfer

coefficient on the inlet end was around 250W/m^2K. The fan end end winding heat transfer coefficient was about half the inlet end values. The variation in the local heat transfer coefficient was very large, from less than 50W/m^2K on the outer surfaces of the end windings to over 450W/m^2K on the inner surfaces of the inlet end end windings. The overall end winding heat transfer coefficient on both ends was found to vary with the relationship (motor speed)$^{0.78}$. As the air flow increased, the exponent increased slightly for the inlet end and it reduced slightly for the fan end.

Wafters had great influence on the end windings cooling characteristics at the inlet end and almost no influence at the fan end. There was an optimum wafter length for the inlet end. Reversing the direction of rotation had no effect on the air flow, but the heat transfer coefficient showed a reduction of ten percent. Reduction of the distance between the end shield and the end windings at the fan end enhanced the heat transfer at that end. Consequently this reduced the temperature difference between the two end windings. An air guide over the inlet end end windings enhanced the heat flow by about thirty percent despite decreased air through flow by around thirty percent. Flow patterns revealed a recirculation above the wafters at the inlet end which enhanced the heat transfer in the region (refer to Figure 2.4).

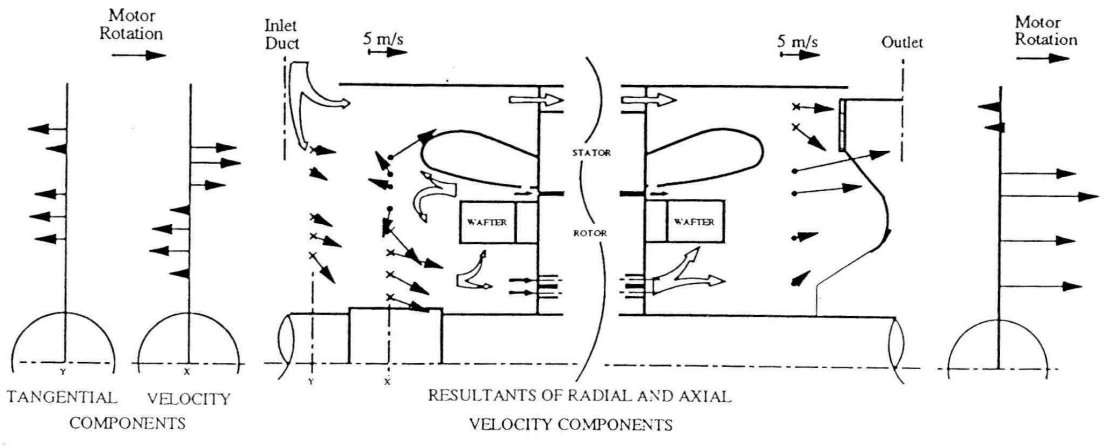

Figure 2.4 - Velocity distributions and flow patterns near the end windings [22]

The last in this series of papers, Pickering et al.[23] investigated the heat transfer from the stator end windings of a low voltage concentric wound induction motor. The motor used in the tests was again a C280M with a C280S core. Compared to the results obtained previously using a low voltage lap wound end winding [22], the temperature distribution over the end windings was more uniform; the difference between the average temperature of each end windings was lower (only 5^{o}C compared to the 10^{o}C on low voltage lap wound induction motors) and the end windings were running at a lower temperature. The overall heat transfer coefficients on the concentric wound end winding were much higher than those on the lap wound end windings. The authors attribute the reported high heat transfer coefficient to the way the envelope area of the end windings was defined.

The overall heat transfer coefficient of the end windings at the inlet end was seventy percent larger than that on the fan end. The air flow inside the induction motor was also investigated using pitot probes. Unlike the lap wound end winding

case, no recirculations were detected in the end region (compare Figure 2.4 with Figure 2.5).

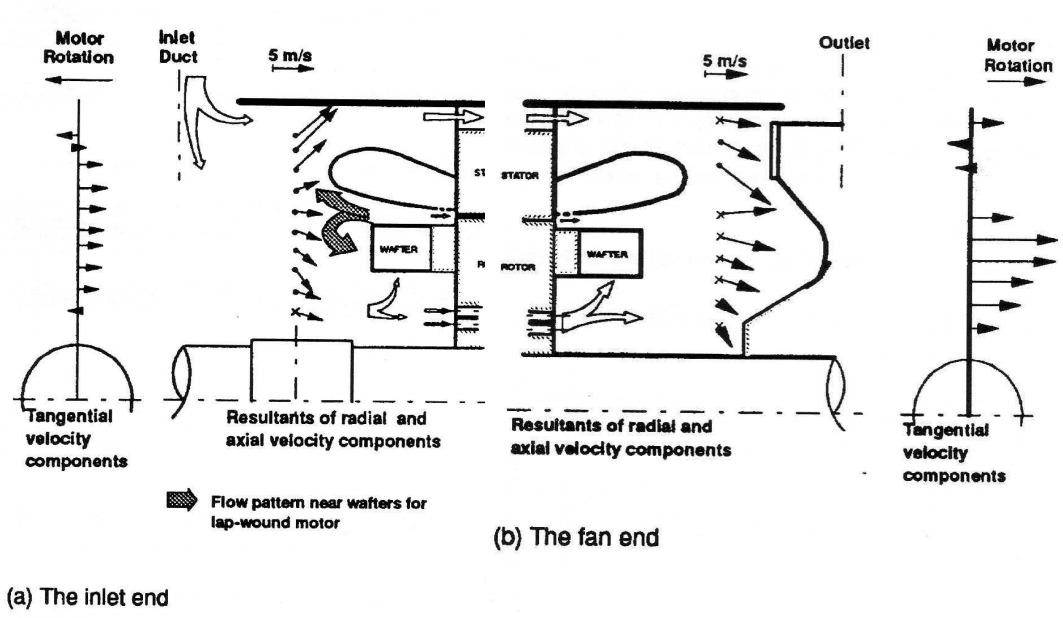

Figure 2.5 - Velocity distributions and flow patterns near the end windings [23]

For the fan end, the end winding heat transfer coefficient varied with the relationship (motor speed)$^{0.80}$, while for the inlet end, the end winding heat transfer coefficient varied as (motor speed)$^{1.11}$. As the flow rate of cooling air was reduced a decrease in the heat transfer coefficient of the end windings at the inlet end was registered while an increase in heat transfer coefficient of the end windings was experienced on the fan end. Increasing the wafter length reduced the total cooling air flow. Increasing the wafter length did not improve the heat transfer at the fan end but a progressive improvement in heat transfer was registered at the inlet end.

Takahashi et al. [24] investigated the internal airflow and the thermal contact conductance between the stator core and frame of a TEFC induction motor. The variation of the heat transfer coefficient of the outer fins of the frame was also

investigated. It was observed that the heat transfer on the frame fins decreased gradually along the frame by as much as fifty percent. The flow field in the end region of a TEFC induction motor was also investigated. The main results showed that behind the end windings the air velocity was very slow. Above the end windings the velocity increased rapidly just above the end winding tips to a maximum value above the wafter. This study did not investigate the air flow patterns inside the end region, and so the velocity plots presented in the paper are difficult to interpret. Finally the authors suggested a method of circulating the air inside the motor via a series of ventilation passages in the rotor and stator (refer to Figure 2.6).

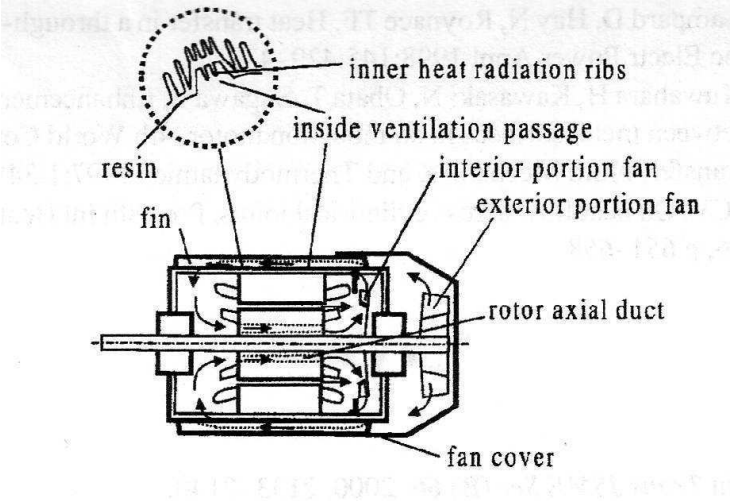

Figure 2.6 – Suggested method of circulating internal air[24].

Hay et al. [25] summarised the correlations which may be employed in thermal models of electrical machines. The part of the paper relevant to the end windings suggested that the use of correlations for stirred vessels can be applied to the end region. In addition, it was suggested that in high voltage machines with formed

end windings correlations for heat transfer from tube banks in a heat exchanger may be used.

Hay et al. found that under comparable conditions using the correlation of a stirred vessel produced results that compared well with the correlation suggested earlier by Oslejsek [26].

Oslejsek [26] suggested that in enclosed induction motors without axial internal ventilation, up to 80% of the heat loss of the end windings is transferred through the swirling air on to the shields and edge of the frame. The flow field reported consisted of two main recirculating flows superimposed on the main swirling flow. Referring to Figure 2.7, a strong recirculating flow was present over the wafters. A weaker recirculating flow passed over the end windings, flowed downwards behind the end windings and through the lower part of the end windings to combine with the other main recirculating flow. It was suggested that the heat transfer coefficient varied as (motor speed)$^{0.80}$.

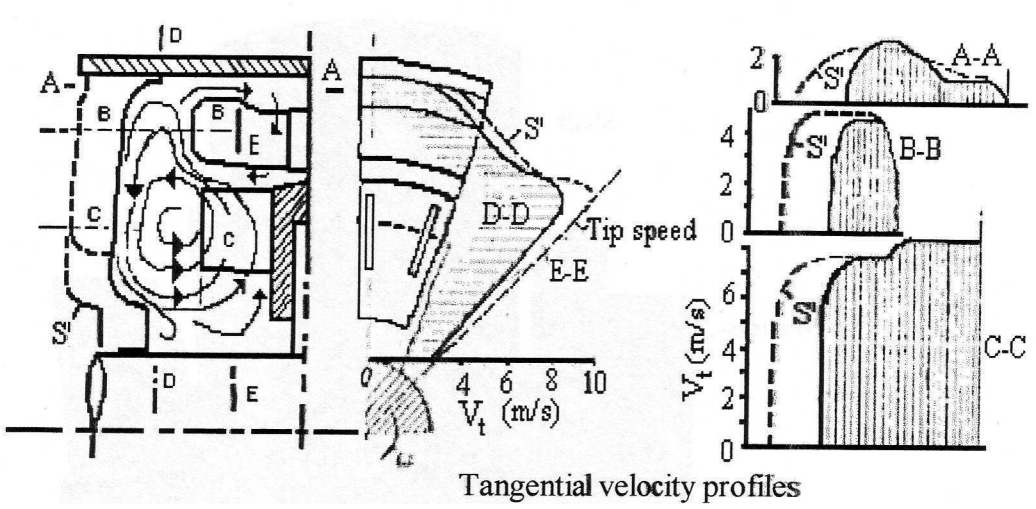

Figure 2.7 – Flow field around end windings as reported by Oslejsek[26].

Oslejsek suggested improvements which may be implemented in the design of end regions of TEFC induction motors:

1. In order to enhance radial flow, the inner surface of the end windings should be sufficiently far away from the wafters and should be inclined to the axes of rotation as much as possible.

2. It is advantageous to place a surface between the wafters and any radial fins on the end shield.

3. The clearance between the end shield and the end windings should not be made too small, in order to prevent blockage of the return flow.

Mugglestone et al. [9] investigated the effects the end winding porosity has upon the flow field and windage losses. A simulated end region of a high voltage induction motor was used where the end windings were replaced by a series of rectangular columns of various widths in order to vary the porosity. Both experimental and CFD techniques were used throughout this investigation. For the CFD investigations the standard k-ε turbulence model and the unsteady sliding mesh technique were used. The porosity was varied from an impermeable end winding (0% open) to an absent end winding (100% open). With an impermeable end winding, the flow was restricted by the end winding and development of a radial flow was inhibited. The majority of the flow took place above the wafters leaving the rotor bar extension fan to starve of cooling air. This configuration generates a reduction in heat transfer at both the base of the end windings and the rotor end.

With 30% porosity an additional recirculation route through the end windings was created. The flow induced by the rotor bar extensions was increased substantially. The predominant velocities were still tangential and as a result the porous end windings still produced a high resistance to flow. Counter swirl vortices were generated behind each of the end windings.

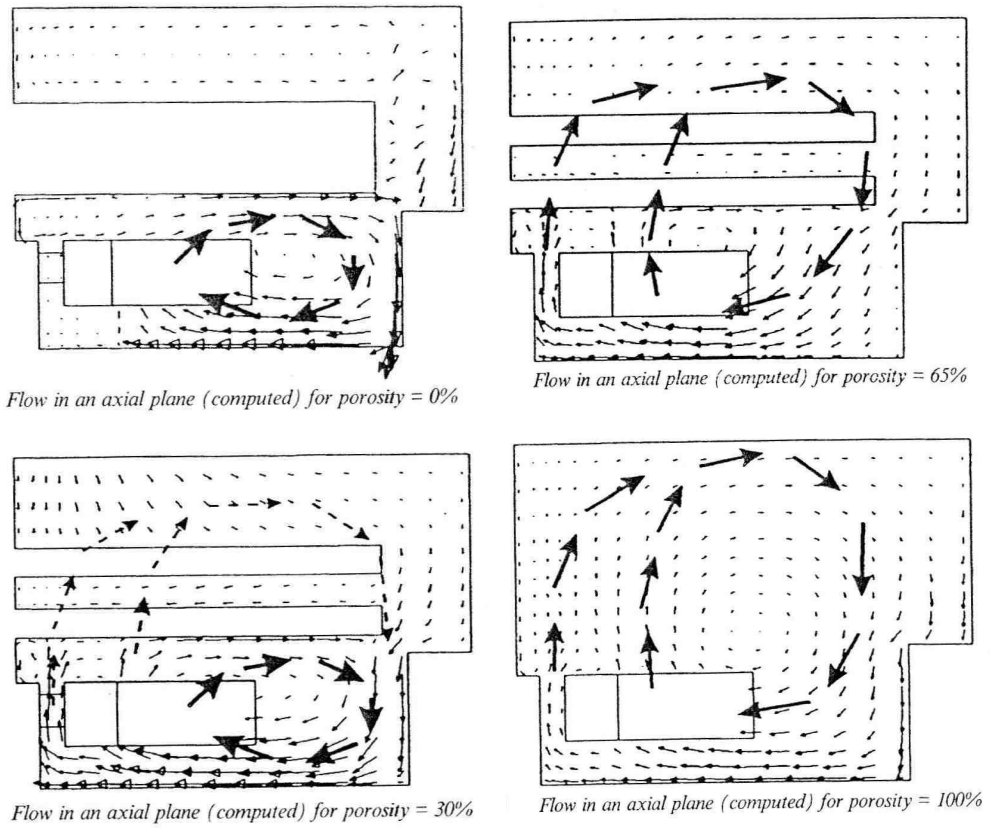

Figure 2.8 – Flow field around simulated end windings as reported by Mugglestone et al.[9].

As the porosity was increased to 65%, the flow through the end winding was further increased. The main flows present were the recirculating flow above the wafters and the recirculating flow from the wafters through the end windings. These combined behind the end windings with a third recirculating flow emerging from the rotor bar extensions and through the lower part of the end windings.

These three flows combined in the area above the end windings. The fully open case behaved like a stirred vessel.

The windage losses increased with increasing porosity except for the 100% porosity case which gave a windage loss a little higher than the 30% open case. The 65% open model gave the biggest windage losses. The authors agree with Zautner's[19] work relating to the balance between heat transfer and windage loss.

Another paper by Mugglestone et al. [27] investigated the flow field and heat transfer in the end region of a TEFC induction motor using experimental and CFD techniques. The flow field identified two circulating flows. One above the wafters and another driven by the rotor bar extension through the end windings, upwards behind the end windings and then combining with the other recirculating flow above the wafter (refer to Figure 2.9). Although CFD predicted the flow field well, the accuracy of the local heat transfer coefficients did not correspond well with experiment. The CFD techniques underestimated the heat transfer coefficients by as much as 30% in some areas. However, the CFD predicted the spatial distribution of the local heat transfer coefficients well.

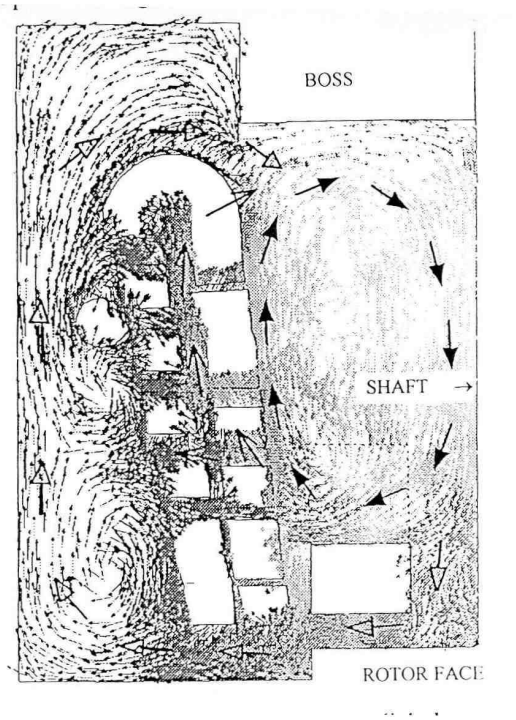

Figure 2.9 - Flow circulation in the end region as reported by Mugglestone et al. [27]

Further investigations by Mugglestone et al.[11] addressed the effect of geometric changes on the flow field and heat transfer in the end region of the TEFC induction motor. These include varying the number of wafters, the wafters' length and width together with the effect of changing the proximity of the wafters to the end windings. Both experimental and CFD techniques were utilised for this work. The local heat transfer coefficients were predicted to within 30% error compared with experiment. Trends of heat transfer coefficients were accurately forecasted. Some CFD models having wafter lengths between 60mm and 120mm failed to converge. This was attributed to the gradual change in the secondary flow field behind the end windings. With short wafters the air flowed upwards behind the end windings while with long wafters it flowed in the opposite direction (refer to Figure 2.10). Thus an unstable flow might have been present when using medium

sized wafters making the CFD models impossible to converge. Generally, longer wafters did not give better heat transfer on the end windings.

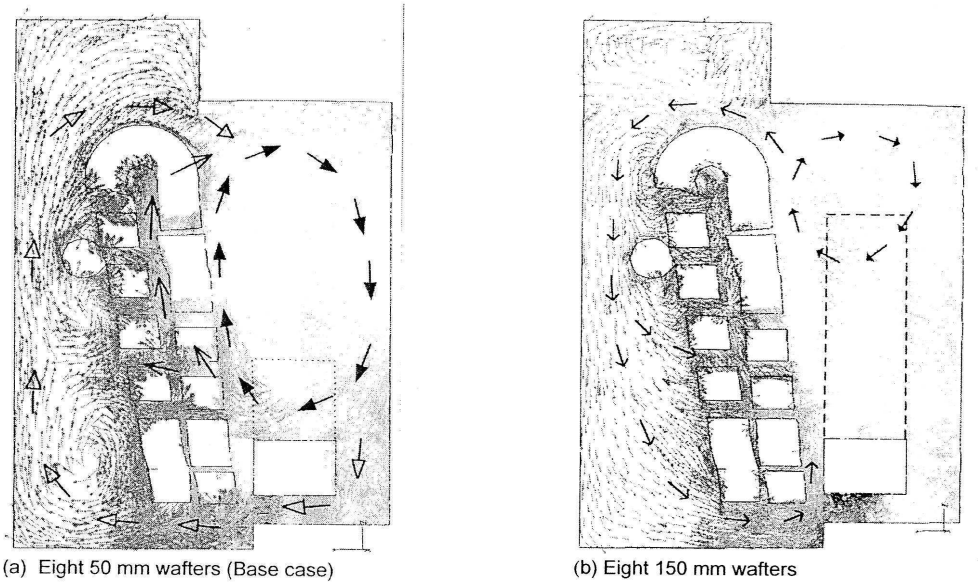

Figure 2.10 - Flow circulation in the end region using different wafter lengths[11]

As the number of wafters was progressively reduced from eight to two, a reduction in the overall end winding heat transfer coefficient was observed when using the standard 50mm long wafters. The number of wafters had no effect on the heat transfer from the end windings when the longer wafters were used. Another finding was that as the width of the wafter was decreased, the heat transfer from the end winding deteriorated. As the wafters were moved away from the end winding proximity, the heat transfer from the end windings deteriorated further. A concluding remark was made on how the CFD accurately predicted trends in local heat transfer coefficients and CFD techniques gave new insights into the fluid flow behaviour in end regions of electrical machines.

Pickering et al. [10] described how CFD techniques may be used in the design of electric motors and generators by collecting results of previous papers by the group identifying how CFD techniques may be employed.

A more recent paper by Schleussinger et al. [28] investigated the heat transfer on orthogonal banks of non-circular bars in cross flow (refer to Figure 2.11). The authors suggested that these results may be used on end windings of electrical machines. The bars were exposed to a constant heat flux and thermocouples and thermometers measured the temperature at the surface of the bars and the inlet temperature respectively. Thus the heat transfer coefficient was defined with respect to the incoming air temperature. It was found that for a single bar that the local heat transfer coefficient varied considerable with the flow angle. The overall heat transfer coefficient was only slightly changed. This also applied to the bars within the crossing bank.

The distribution of the local heat transfer coefficient is very important in today's applications, where often designs are pushed to the limits, as these identify hot spots which may lead to failure. The authors argue that it is difficult to accurately predict the local and overall heat transfer coefficients as these are influenced by several parameters. Further more, CFD is not capable of predicting heat transfer to high levels of certainty without proper validation by comparable geometries.

Figure 2.11 - Experimental setup used by Schleussinger et al.[28]

2.3 Discussion on published literature

A substantial amount of information has been presented through this literature review. The data collected did not provide enough information for a designer to design effectively a better end region.

Correlations which may be used to calculate the overall heat transfer coefficient of the end windings were suggested. These were all of the basic ‘power law’ form, however the constant within the correlation produced a large range of predicted heat transfer coefficients especially at high speeds. These differences are mainly due to fundamental differences with the investigations (such as different machine types and sizes). Thus with the correlations provided it is difficult to draw any specific conclusions regarding the overall heat transfer coefficients especially at high speeds. In fact all this data may sometimes lead to confusion and correspondingly unrealistic assumptions of the heat transfer coefficients. Even though these correlations have been used successfully with established end region designs (that is the ones using wafters positioned over the end rings), they do not necessarily apply to other configurations.

The cause of the fluid's behaviour has not been clearly identified. Flow fields in alternative novel configurations, which may cause the fluid to behave differently, are very difficult to predict. The majority of the literature reviewed did not provide tested alternative cooling arrangements. Therefore a lot of guess work is still unavoidable in end region designs and there is significant scope for further CFD and experimental work to improve the design process. This is the aim of this thesis.

3 Experimental Test Facility

Experimental methods were used to validate the results generated using CFD techniques, which are outlined in Chapter 4. Three distinct validation exercises were performed to validate the data and these are summarised below.

1. Nature of flow field in the end region
2. Heat transfer from the end windings to the frame
3. Windage loss.

An existing experimental facility that was able to record velocity measurements in key locations in the end region under test, heat transfer coefficients over the surface of a heated end winding as well as other locations on the frame and windage loss was configured and re-commissioned.

3.1 The Experimental Rig

An experimental facility used previously for another research program was used to conduct the validation tests. This consisted of a set of end windings from the non connecting end of a 2-pole TEFC induction motor enclosed in a Perspex ‘frame’. A Perspex frame was used rather than a metallic frame in order to visualise the flow and help positioning of the instrumentation. One of the end windings was supplied with an electric current (approximately 50A), to generate heat through Ohmic heating. The current was delivered via a step down transformer, which was in turn supplied using a variable voltage supply. The current was monitored using a digital clamp power analyser.

A model steel rotor (simulating a shaft), rotor bar extensions and an end ring were driven by means of a variable speed drive. The variable speed drive consisted of a separate floating frame induction motor , which was controlled by a pulse width modulation transistor inverter. Wafters and other fan configurations were bolted to the rotor accordingly.

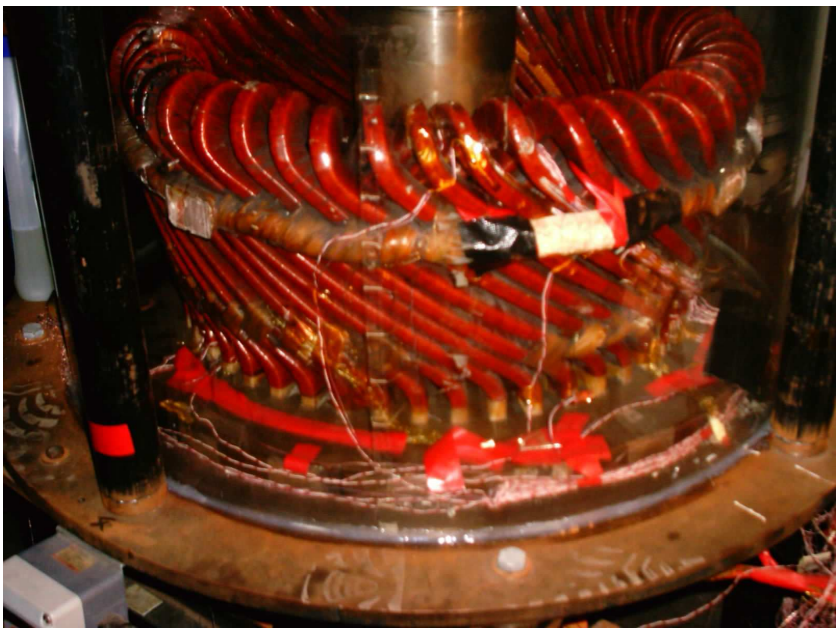

Figure 3.1 - Photo of the experimental rig

Figure 3.1 shows a photo of the rig with the end windings, shaft and perspex casing clearly visible. Figure 3.2 shows a schematic half section of the rig illustrating the location of other key components such as wafters, end ring and rotor bar extensions.

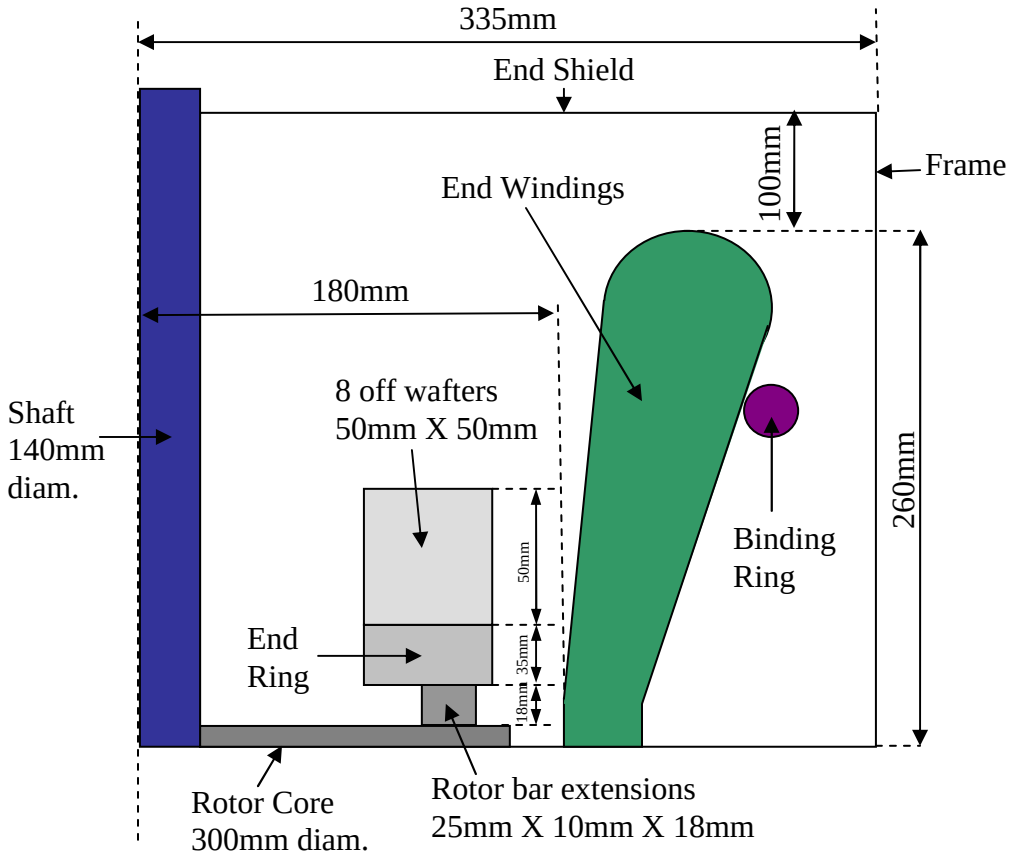

Figure 3.2 – Schematic view illustrating main components of the end region under investigation.

3.2 Instrumentation

3.2.1 Velocity Measurements / Flow Visualisation

Measurements of mean velocities were taken in key locations using a 5 hole pressure probe (Schiltknecht Messtechnik Ag spherical probe type 601). This recorded a mean speed as well as a mean direction of the flow. The probe consisted of an 8mm spherical head, with a total pressure tapping situated on the front of the sphere (port 2 in Figure 3.3) and four static pressure tappings equally spaced along the side of the sphere (ports 1, 3, 4 &5 in Figure 3.3).

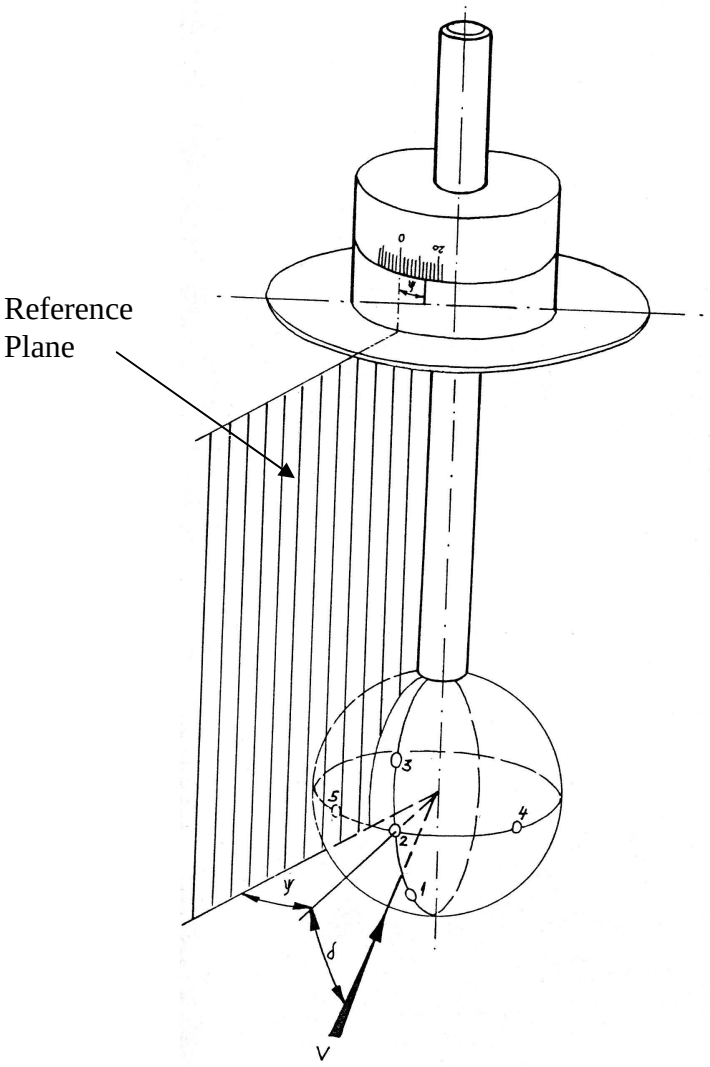

Figure 3.3 - Five hole probe used for velocity measurements

Differential pressure readings from the probe ports were recorded by means of an electronic micromanometer (Furness micromanometer model FCO510). The probe was connected to the micromanometer through a switching box. Both the micromanometer and the switching box (built in-house) were interfaced to a PC using serial ports. The switching sequence was controlled by a program written in

Visual Basic for Applications (VBA), within Microsoft Excel™. Values of differential pressures were recorded on a spreadsheet.

The 5-hole probe was calibrated in a wind tunnel at various angles of attack and speeds. The method used to obtain velocity and direction is given in Appendix A together with the calibration curves.

In addition to the velocity measurements, simple flow visualisation was performed using wool tufts attached to the end of a rod and positioned in appropriate places. This gave an insight to the overall flow field direction.

3.2.2 Heat Transfer Measurements

Micro-foil heat flux sensors (Rdf Corporation type 27036-2), consisting of a thermopile and a T-type thermocouple, were used to measure the heat flux (Q'') and wall temperature (T) at various locations on the heated end winding and frame. Figure 3.4 shows a photo of a heat flux sensor of the type used.

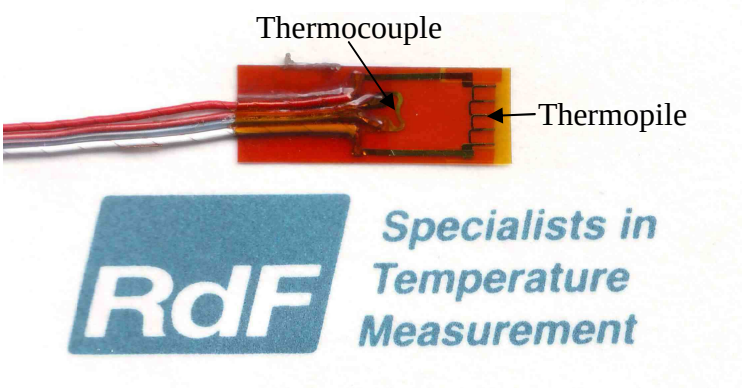

Figure 3.4 - Photograph of heat flux sensors consisting of a thermopile and a thermocouple used to measure heat fluxes and wall temperatures respectively.

A data logger (Campbell Scientific CR10X) recorded readings from these heat flux sensors every 5 seconds. Values of heat fluxes and temperatures were then averaged over periods of five minutes. The averaged values were used for analysis.

Figure 3.5 shows the locations of the heat flux sensors on the casing (26-30) and end winding (1-25).

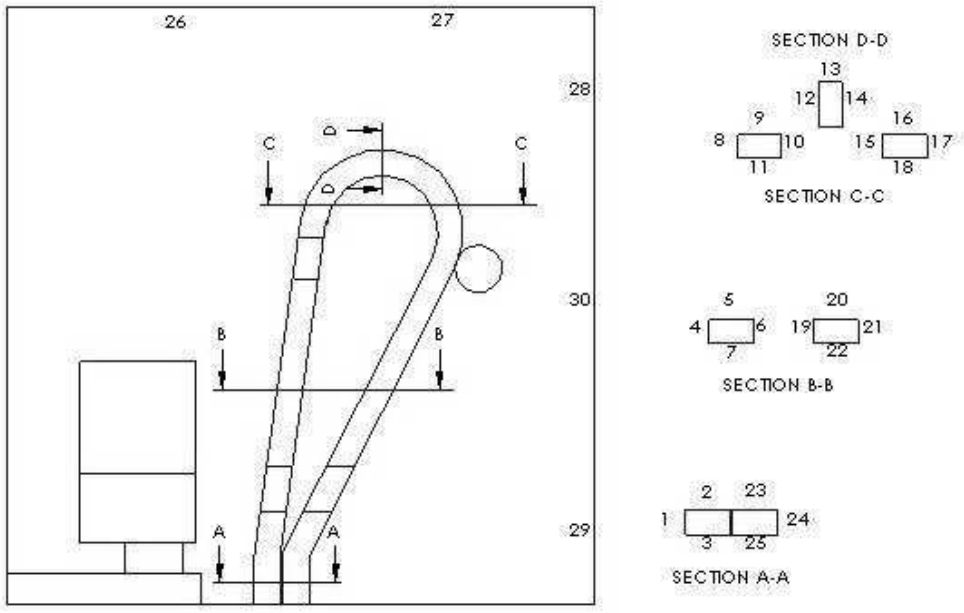

Figure 3.5 - Reference locations of heat flux sensors on end winding and frame

Since a total of 30 heat flux sensors were used together with additional sensors, three multiplexers (Campbell Scientific AM32 and AM416) were required to connect all these sensors to the data logger. Analysis of the data was then done using Microsoft Excel. A representative bulk temperature was measured using a thermocouple that was fixed in space just above the rotating wafters.

A local convective heat transfer coefficient was defined as:

$$h_{local} = \frac{\left(Q''_{gauge} - Q''_{radiation}\right)}{\left(T_{gauge} - T_{bulk\ air}\right)} \qquad (3.1)$$

As shown in the above equation, to compensate for the fact that all CFD analysis in this work did not involve radiation modelling, the heat flux recorded by the sensor was corrected to account for the heat transfer by radiation when comparing experimental and CFD data. The heat transfer by radiation from the sensor was calculated using the equation:

$$Q''_{radiation} = \varepsilon\sigma\left(T^4{}_{gauge} - T^4{}_{bulkair}\right) \qquad (3.2)$$

A value of emissivity for the sensor of 0.7 is assigned. This is in accordance with the manufacturer's data and treats the sensor as a grey body in infinite surroundings.

The heat flux due to radiation was negligible (of the order of 4%) compared to the heat flux due to convection and was only taken into account for completeness.

With the setup described earlier, that is only a heated winding as a heat source, the heat flux through the frame is too small (large surface area). This will result in a temperature difference between the internal frame wall and the enclosed air that is also very small, resulting in large experimental uncertainties. In order to overcome this problem, heater pads were fixed on the external surface of the frame in order to supply the frame with a bigger heat flux in the location of the heat flux gauges and therefore the temperature difference between the frame internal surface and

the enclosed air is large enough so as to minimise uncertainties in the calculated heat transfer coefficients of the frame surface. Also the end windings were not heated when doing heat transfer experiments on the frame.

The results obtained using this method should be equally valid even though the direction of heat flow through the frame is reversed. This is because high Reynolds forced convection was the main mode of heat transfer at the frame surface which is dependent on the fluid flow field rather than the direction of heat flow.

3.2.3 Windage loss measurements

The windage power loss to the system can be obtained by measuring the torque on the driving motor frame. This can be achieved as follows:

The frame of the driving motor was free to rotate but the movement of the frame was restricted by a calibrated beam giving measurements of force proportional to its deflection. Figure 3.6 illustrates the beam deflection method used to obtain torque exerted by the driving motor frame. The beam was calibrated separately using a dead weight technique. The calibration chart is shown in Section 9.1.2 of Appendix A.

The deflection experienced by the beam, due to the force transmitted by the frame, was recorded using a linear position sensor (RS P/N 317-780). Position data was recorded by the same data logger used to collect values of heat fluxes and temperatures.

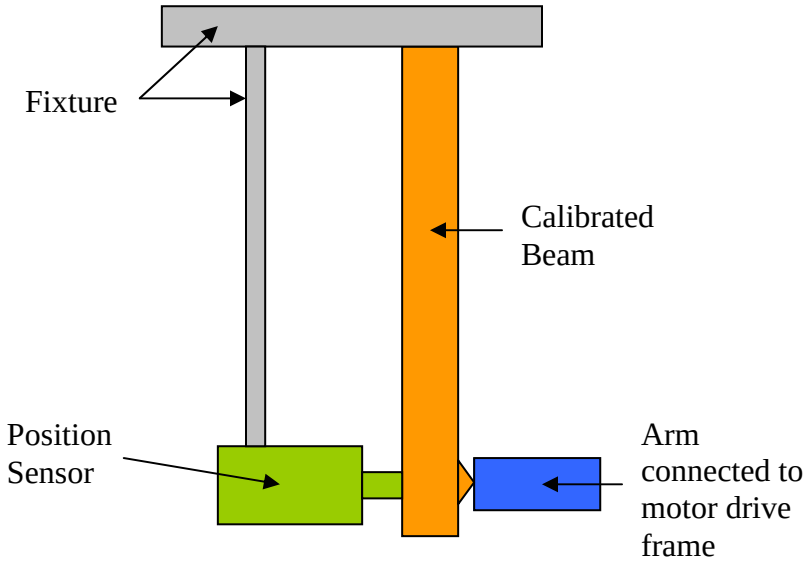

Figure 3.6 – Windage loss measurement arrangement

The force exerted by the frame on the beam was calculated by interpolating the recoded deflections into the calibration data. The power output of the drive was established by multiplying this force by the moment arm and the speed of rotation of the rotor. The latter was simply measured using a digital tachometer (Compact CT6).

The value of the power output by the drive includes the windage loss by the model, frictional losses by bearings and windage losses by the drive unit. Hence in order to eliminate the latter two losses, the rig was run without any wafters installed so that the windage loss due to the wafters alone could be estimated by subtracting the power output of the test without wafters from the power output recorded when the wafters where present.

3.3 Uncertainty Analysis

Results from experiments need to be assessed for their accuracy. The method used in this work is that proposed by Kline and McClintock[29], describing uncertainties in single sample experiments, i.e.

$$\varpi_{\Re} = \left[\left(\frac{\partial \Re}{\partial \nu_1} \varpi_1 \right)^2 + \left(\frac{\partial \Re}{\partial \nu_2} \varpi_2 \right)^2 + \cdots + \left(\frac{\partial \Re}{\partial \nu_n} \varpi_n \right)^2 \right]^{1/2} \qquad (3.3).$$

where $\Re$ is a function dependent on variables ν_i, $\varpi_{\Re}$ is the uncertainty in $\Re$ and ϖ_i is the uncertainty in ν_i.

Then next section describing uncertainties in the velocity measurements is a clear example of how this equation is used in practice.

3.3.1 Velocity measurements

With reference to Appendix A, probe factors K_{1234} and K_{24} were used to calculate local velocity using the 5 hole pressure probe. In order to estimate the uncertainty in K_{1234}, equation 3.3 is applied to relation (9.1) so that

$$\left(\frac{\varpi_{K_{1234}}}{K_{1234}} \right)^2 = \left(\frac{\varpi_{P_{31}}}{P_{31}} \right)^2 + \left(\frac{\varpi_{P_{24}}}{P_{24}} \right)^2 \qquad (3.4).$$

Therefore the uncertainty in factor K_{1234} may easily be estimated using the uncertainties in the pressure readings (which varied with each sample).

The uncertainties in the differential pressure measurements are obtained using sampling theory, where the total error is equal to twice the standard error of the mean of the sample (for 95.5 percent confidence level).

Factor K_{24} and its uncertainty limits were then read off the probe calibration curve (refer to Figure 9.2). The velocity and its uncertainty, is estimated using the uncertainty of factor K_{24}, the uncertainty of the differential pressure P_{24} and applying equation (3.3) to relation (9.2) so that

$$\left(\frac{\varpi_v}{v}\right)^2 = \left(\frac{1}{2}\frac{\varpi_{P_{24}}}{P_{24}}\right)^2 + \left(\frac{1}{2}\frac{\varpi_{K_{24}}}{K_{24}}\right)^2 \qquad (3.5).$$

In order to improve this aspect of the work hot wire anemometry would have been used for velocity measurements. However the time consumed in taking such measurement would have been considerably longer than in the method undertaken here and would therefore have allowed less time for other areas of the research.

3.3.2 Heat Transfer measurements

Factors influencing the accuracy in the heat transfer measurements are:

1. Uncertainty in temperature measurements using thermocouples ($\pm 1^{o}$C according to standard IEC 584-2:1982),
2. Uncertainty in heat flux measurements (±10% according to manufacturer)

Other sources of uncertainties which were not accounted for include:

1. Disturbance of the fluid flow by the heat flux sensor and connecting wires which would affect the local heat transfer coefficient.

2. Contact resistance between sensor and end winding which would affect the surface temperature.

In order to limit the unaccounted errors, the heat flux sensors were fixed to the surfaces in such a way that their connecting wires were behind the sensor relative to the fluid flow. This was done in order to reduce (but not eliminate) interference of the flow by the sensor wiring.

Although there is no feasible means of evaluating these uncertainties, the errors involved due to the above factors should be small due to the highly turbulent nature of the flow field and can therefore be treated as negligible.

3.3.3 Windage Loss measurements

The uncertainties involved in evaluating the windage loss are:

1. Inaccuracy in the moment arm (estimated as ±5 mm).

2. Errors arising from the interpolation in the calibration curve.

Additional uncertainties which were not accounted for include:

1. Fluctuations of the motor speed due to inverter harmonics.

2. Varying friction in the bearings due to temperature rise in the rig.

Even though the frictional losses were eliminated from the windage calculation by running the rig without wafters as described in Section 3.2.3, these losses most probably vary with temperature and load and thus are still an uncertainty. Losses were kept to a minimum by making sure that friction was minimised, that no oscillations were present and that the drive was approximately at a constant temperature.

4 CFD Modeling of End Regions

Although CFD is nowadays widely used in research institutes and industry, a good understanding of the theory associated with it is still essential. Additionally CFD techniques are evolving so quickly that it is difficult for users to keep up to date with current innovative methods. Although it is not the intention of this work to explain methodologies used in CFD, a brief description of CFD is given below. All the theory presented in this chapter is available in standard CFD textbooks such as [30]. In this chapter the fundamental principles of fluid and heat dynamics will be presented together with techniques CFD used to solve these flows.

4.1 Theory behind CFD

Fluid flow is governed by the well known set of equations often referred to as the complete Navier-Stokes equations. This set of equations consists of:

- three distinct momentum equations in three dimensional space
- continuity equation
- energy equation.

These are coupled non-linear second order partial differential equations and there is no general analytical closed form solution to these equations, which leaves no option but to solve them numerically. CFD is a tool whereby the complete Navier-Stokes equations together with other equations (e.g. turbulence equations) are solved numerically.

There are various numerical methods which may be applied to discretize these equations (e.g. finite difference, finite element, finite volume, boundary element, etc); most of the commercially available CFD software uses the Finite Volume Method (FVM). Fluent™, the software which was employed in this work uses FVM. Further information on FVM is provided in Section 4.1.3.

4.1.1 Complete Navier-Stokes equations

The complete Navier-Stokes equations in integral form may be represented by the transport equation for property ϕ:

$$\frac{\partial}{\partial t}\left(\int_{CV}\rho\phi dV\right)+\int_{A}\vec{n}.(\rho\phi\vec{u})dA=\int_{A}\vec{n}.(\Gamma\, grad\,\phi)dA+\int_{CV}S_{\phi}dV \qquad (4.1).$$

In words this equations states that

Rate of increase of ϕ + Net rate of decrease of ϕ due to convection across the boundaries = Rate of Increase of ϕ due to diffusion across the boundaries + Net rate of creation of ϕ

If the property ϕ is replaced by the constant unity, the continuity equation will be formed. Likewise if the property ϕ is replaced by velocities u_i, u_j, u_k in turn, the momentum equations in the x-direction, y-direction and z-direction will be formed respectively. Also if ϕ is replaced by the internal energy *i*, the energy equation is formed.

4.1.2 Turbulence Modelling

In order to be able to solve fluid flow problems using only the complete Navier-Stokes equations, a grid able to resolve all turbulent length scales needs to be set up. The grid length scale must be smaller than the Kolmogorov length scale (defined as $\left(\frac{\nu^3}{\varepsilon}\right)^{1/4}$). This means that a huge grid is required which is unattainable with current technology. Turbulence models are available which assume simplifying rules to effect a numerical solution; the more common models are discussed in the following section.

Reynolds Averaged Navier Stokes (RANS) Turbulence Models

In turbulent flows, velocities may be modelled as consisting of a fluctuating part, having a zero mean value, superimposed on a mean value of the property $\left(\text{that is } \mathrm{u}_\mathrm{i}(t) = \overline{u}_i + u_i'(t)\right)$. If all velocities in the Navier-Stokes equations are replaced by this model and the equations are time averaged, a new set of equations often referred to as the Reynolds Averaged Navier-Stokes (RANS) are obtained. These equations are identical to the Navier-Stokes equations except that now u_i is replaced by $\overline{u}_i$ and additional terms involving products of fluctuating velocities appear. These six extra terms are called Reynolds stresses. A new problem now arises, this being the closure problem (number of unknowns exceed the number of equations).

The majority of turbulence models assume that the effect of turbulence can be represented as an increase in viscosity. This leads to the term turbulent kinematic viscosity which is defined by the Boussinesq relationship:

$$-\overline{u_i' u_j'} = \nu_t \left(\frac{\partial \overline{u}_i}{\partial x_j} + \frac{\partial \overline{u}_j}{\partial x_i} \right) - \frac{2}{3} k \partial_{ij} \qquad (4.2)$$

where ∂_{ij} is the is the Kronecker delta function such that $\partial_{ij} = 1 \text{if } i = j$ otherwise $\partial_{ij} = 0$ and $k = \frac{1}{2}\left(\overline{u_i'^2}\right)$ termed the turbulent kinetic energy per unit mass.

There are a great number of turbulence models available. However the most robust one is undoubtedly the standard two equation *k-ε* turbulence model.

***k-ε* turbulence model**

In the *k-ε* turbulence model *k* is the turbulent kinetic energy and *ε* is the rate of change of $k\left(\text{ that is } \varepsilon = \frac{dk}{dt}\right)$. The turbulent kinematic viscosity in this model is defined by the equation:

$$\nu_t = C_\mu \frac{k^2}{\varepsilon} \qquad (4.3)$$

where C_μ is a dimensionless empirical constant (= 0.09).

In words, the k-ε turbulence model uses the following transport equations for k and ε:

Rate of change of k or ε	+	Transport of k or ε by convection	=	Transport of k or ε by diffusion	+	Rate of production of k or ε	-	Rate of destruction of k or ε

There are various other turbulence models available as standard in commercial CFD software, however generally, the k-ε model is the most reliable since it has been validated thoroughly, and robust since solution is generally very stable.

Several variants of the k-ε model exist (e.g. the RNG k-ε turbulence model which uses the statistical technique known as the renormalization-group theory). These may exhibit better performance for special applications.

***k*-ω turbulence model**

Another turbulence model commonly available in CFD packages is the k-ω turbulence model. Again k stands for the turbulent kinetic energy and ω is the specific dissipation rate which can also be thought of as the ratio of ε to k. The turbulent kinematic viscosity in the k-ω turbulence model is defined by the equation:

$$\nu_t = \alpha^* \frac{k}{\varpi} \qquad (4.4)$$

where α^* is a damping factor causing a low Reynolds number correction.

Both the k-ε and the k-ω turbulence models however are isotropic since they assume the three normal Reynolds stresses to be equal.

RSM turbulence model.

The Reynolds Stress Model (RSM) on the other hand does not assume the turbulence to be isotropic. It models each of the six distinct Reynolds stresses using six different transport equations. Generally the computational costs involved to solve these equations outweigh their benefits, as will be shown in the chapter on the CFD results.

More advanced turbulence models

In recent years, with the development of more powerful computers, researchers have started to investigate how to overcome the limitations of RANS by dispensing the time averaging. Large Eddy Simulation (LES) and Detached Eddy Simulation (DES) were formulated.

By using spatial filtering techniques to filter out eddies which are smaller than the grid scale, these turbulence models resolve large scale eddies. Smaller scale eddies are then modelled. Therefore both of these techniques require a denser grid with respect to the ordinary RANS models. Clearly LES and DES are the stepping stones from RANS to DNS (Direct Numerical Solution).

4.1.3 Discretization and grid alternatives

Spatial discretization is the process of dividing the domain into small elements connected to one another. The collection of elements is often referred to as the

grid. The equations are then solved for each individual element. Most of the commercial CFD software available use the finite volume method (FVM). In the FVM individual elements in the grid are referred to as cells. Cells are constructed out of faces, edges and nodes (refer to Figure 4.1).

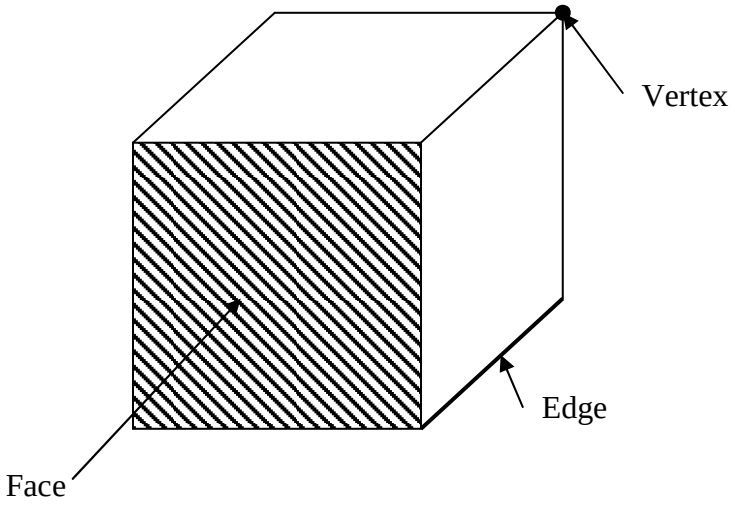

Figure 4.1 – Terminology for describing the features of cells used in FVM

Grids may generally be either structured (consisting of hexahedral cells) or unstructured (consisting of tetrahedral cells). Fluent v6 is an unstructured solver which means that it can handle both structured and unstructured grids. The advantages of one over the other are;

- Structured grids require much less cells than unstructured grids.
- Unstructured grids can be applied also to complex geometry.
- Structured grids are easier to solve.

Due to the complexity of the geometry present in the end region of induction motors particularly the end windings, the only feasible option in this work was the use of an unstructured grid.

4.1.4 Wall functions

Strictly speaking, these turbulence models are valid only in free stream flow (that is far away from the influence of walls). In the vicinity of the wall a boundary layer exists where the fluid's velocity gradually increases from zero at the wall (non slip condition) to the mean stream velocity. Boundary layer theory is a complex subject however the basic principles employed in CFD code may be explained using Figure 4.2, where $u^+ = \frac{u}{u_\tau}$,(u_τ being the shear velocity and is equal to $\sqrt{\frac{\tau_w}{\rho}}$, where τ_w is the shear stress at the wall) and $y^+ = \frac{\rho u_\tau y}{\mu}$ where y is the distance from the wall.

Turbulent boundary layers consist of a laminar part very close to the wall (usually referred to as the laminar sub layer) where (molecular) viscosity plays a major role in momentum and mass or heat transfer. At the outermost layer turbulence plays a major role and thus is generally referred to as the fully turbulent layer. In between both turbulence and viscosity are equally important.

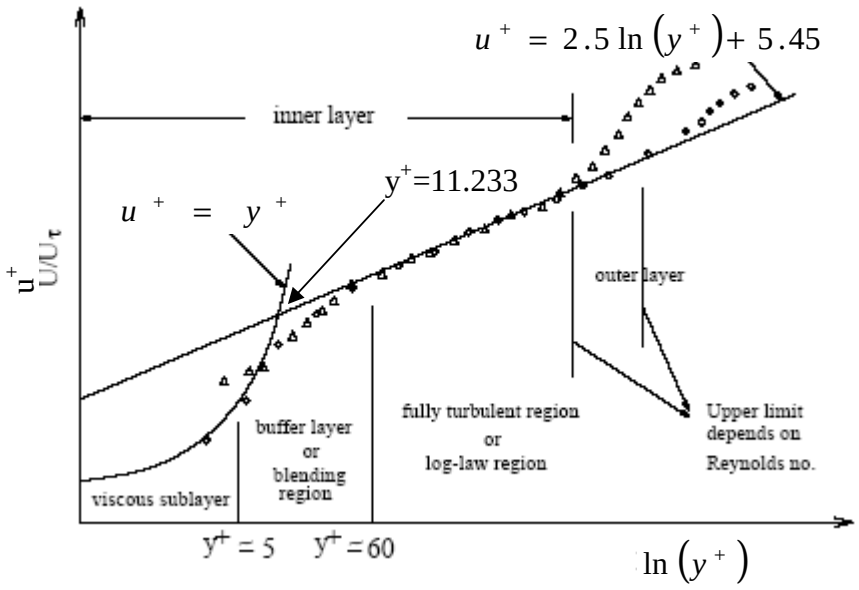

Figure 4.2 - Sub divisions in near wall region of boundary layer adapted from [31]

In CFD there are two approaches which may be used to solve fluid flow in the vicinity of walls. The near wall modelling approach resolves the flow all the way down to the laminar sub layer. In Fluent this approach is referred to as the enhanced wall treatment. This approach requires a large number of cells in the vicinity of the wall and consequently is very demanding in terms of computer power and memory.

The second alternative approach is the use of wall functions. This approach is widely used in CFD applications and instead of resolving the boundary layer, a wall function is applied in the vicinity of the wall and therefore needs much less computer resources (refer to Figure 4.3).

The most widely used wall function is the standard wall function which employs a two layer concept. If the y^+ value for the cells in the vicinity of the walls is less than 11.225 the linear relationship stated in Figure 4.2 is applied (since the cell lies

in the laminar sub layer). Otherwise the log law stated in Figure 4.2 is applied. Strictly speaking the log law applies only in cells where y^+ value lies in the region between $30 > y^+ > 300$ (cell lies in the outer turbulent layer of the boundary layer) and consequently it is highly advisable to have y^+ values between 30 and 300. Consequently the cell size is very critical for the wall function to be successful. Additionally since y^+ is dependent on the flow, its value will change as the solution progresses. This makes the wall functions technically demanding to use and a great deal of care and attention is required to use wall functions properly.

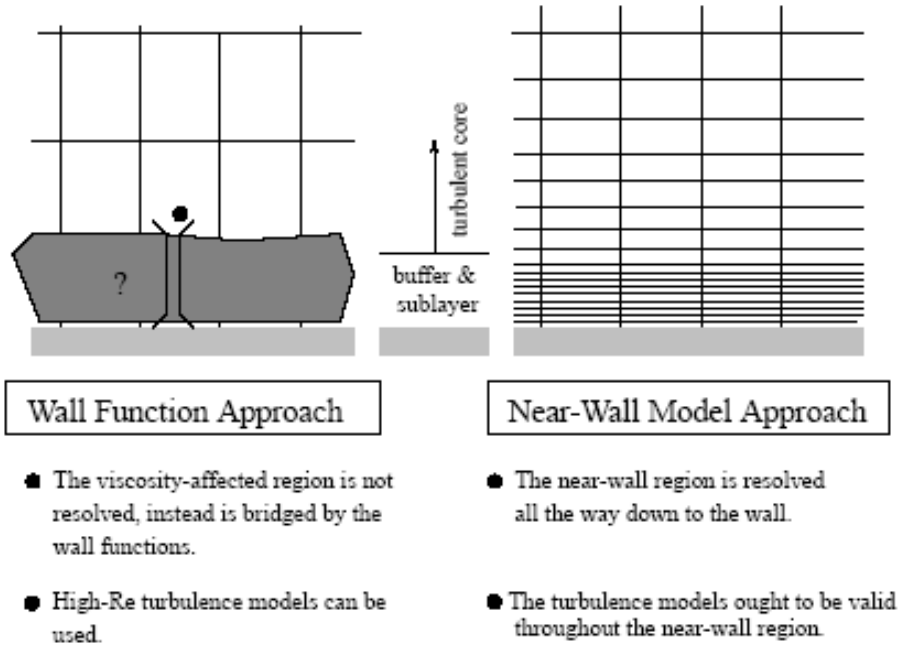

Figure 4.3 - Wall function and near wall modeling approaches [31]

Apart from the standard wall function, other more complicated wall functions are also available (for example the non equilibrium wall function used in Fluent). However these require much more computer resources and the solution process is generally more difficult since the log law is sensitized to pressure gradient effects

and the two layer based concept is also applied to compute the budget of turbulence kinetic energy in the wall-neighbouring cells.

4.1.5 Solution techniques

The solution process employs an iterative technique to arrive at a solution. At each iteration step a solution is obtained. Residuals (which are a measure of error in the solution) are used to assess convergence. For example the residual for the continuity equation is defined as

$$R = \sum_{\text{cells P}} \left| \text{Rate of mass creation in cell P} \right| \qquad (4.5)$$

Residuals are generally monitored during the solution process to assess the stability of the solution apart from its convergence.

Relaxation factors control the amount of change between successive iterations in order to prevent the solution from becoming unstable (leading to divergence). Thus a relaxation factor (α), for a variable ϕ, is defined as

$$\alpha = \frac{\phi' - \phi_n}{\phi_{n+1} - \phi_n} \qquad (4.6)$$

Where ϕ' is the adjusted value of ϕ to be used in the n+1 iteration.

4.2 CFD analysis of Electric Motors

Sections of electrical motors, in which fluid flow is important such as the end region, may benefit from CFD techniques. However some special techniques must be employed. These special modelling techniques will be discussed next.

4.2.1 Modelling technique

Due to the rotating nature of electric motors special modelling techniques must be employed. There are two ways in which rotating machines may be modelled. If a steady state (time averaged) solution is required the Multiple (Rotating) Reference Frame (MRF) technique is used otherwise if a time dependent analysis is required, the Sliding Mesh (SM) technique is used.

The rotating reference frame technique includes the acceleration of the coordinate system in the flow equations so that the fluid is steady with respect to the rotating (non-inertial) reference frame. Therefore a steady state analysis may be performed.

The Multiple Reference Frame technique divides the domain into sub domains (refer to Figure 4.4). In each of these sub domains the rotating reference frame technique is employed. Each sub domain may rotate at a different speed. Thus a typical end region configuration will consist of two frames of reference, a stationary reference frame for the stator domain and a rotating reference frame for the rotor domain. Despite this technique being an approximation, it gives reasonably accurate results especially when the interaction between the domains is minimal (such as the case in induction machines where the end windings are

circumferentially evenly distributed and the gap between the wafters and the end windings is considerable). It is suggested however that the boundary is positioned in such a way that all rotating walls are contained in the rotating domain while all stationary walls are contained in the stationary domain. The boundary separating the two domains is made as an interior zone common to the two domains so that continuity is automatically preserved through the boundary.

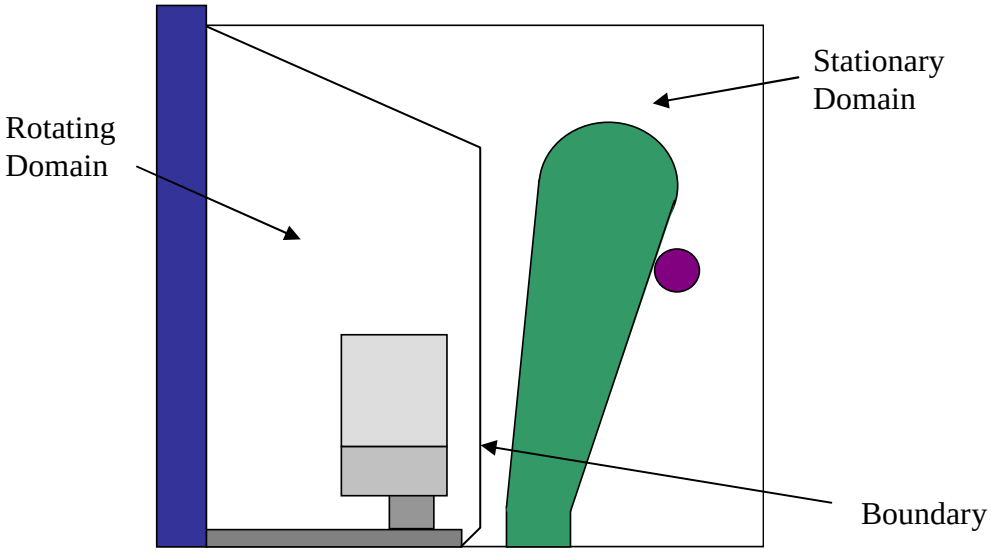

Figure 4.4 – Domain subdivision used in MRF technique in Fluent™ [31]

If a time dependent model is required the sliding mesh (SM) technique must be employed. Here the rotating reference frame is physically rotating. This is done by rotating the rotor domain in small increments at each time step. Thus the two domain interfaces slide relative to one another. Since this technique requires a lot more resources than the MRF technique, it is usually used as a last resort when steady state analysis does not converge (indicating that most probably an unstable flow exists).

If the interaction between the rotor and the stator is high (such as salient pole machines) then the SM technique will give better results compared to the MRF technique. However the domains in the models investigated in this work did not exhibit strong interaction and so the MRF technique gave sufficiently accurate results.

4.2.2 Features worth modelling

As highlighted in Section 4.1.4, cells near walls must meet the y^+ criteria imposed by the wall functions. Additionally since the grid ultimately consists of straight edges, curved edges must be approximated by a series of straight lines. Clearly there is a contradiction between the two requirements since on one hand the wall functions require a course grid in the vicinity of the wall and on the other hand the complex geometry requires a fine grid to preserve its features. Consequently a balance has to be found. Small details which have no influence on the fluid flow should be avoided. It is advisable to model only the major features and disregard features such as bolts and nuts. Features influencing the fluid flow, such as spacers between the end windings, are significant and should be included.

4.2.3 Meshing and grid independence

Due to the complex geometry present in the end region of induction motors (particularly the end windings), the grid is constrained to contain only tetrahedral cells. The initial grids of the models described in this work use a grid size of the order of 3mm. The model is then solved to arrive at an initial solution. Monitors of total heat flow, windage loss and bulk fluid temperature together with the standard

residual plots of mass, velocities, turbulence quantities and energy were used to assess convergence (refer to Figure 4.5).

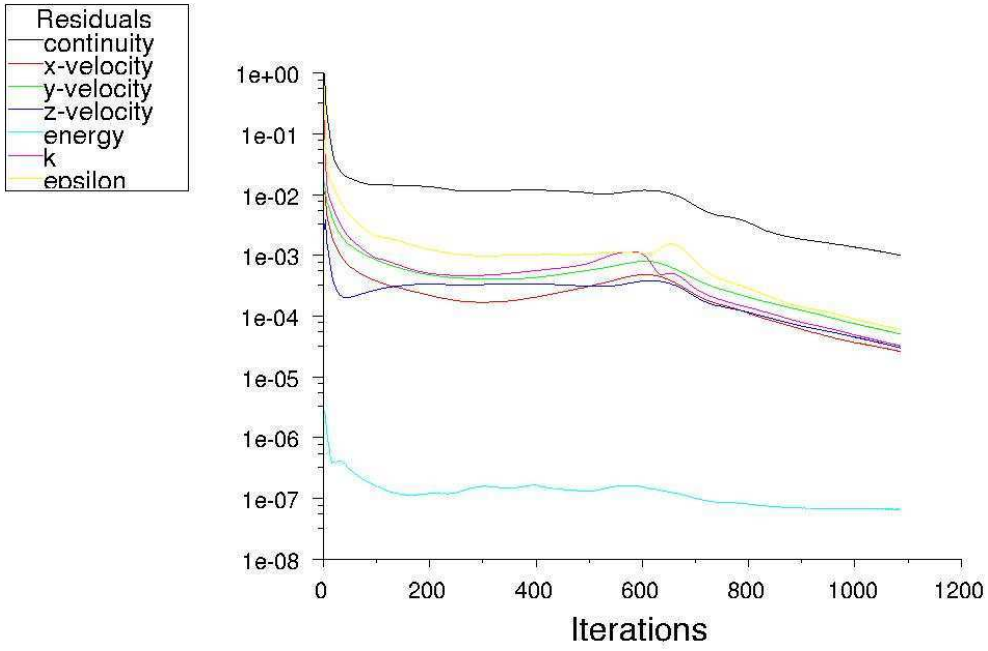

Figure 4.5 – Typical residual monitors

Next the grid is adapted on volume of cells and velocity gradients to generate an even finer mesh. The model is again solved using this new generated mesh using the same monitors used previously. If the results obtained by the two meshes are comparable (to within 10%), then the solution is assumed to be grid independent. Otherwise the adaption process is again repeated. Generally, the final grids in this work contain around 800,000 cells.

4.2.4 Validation of the CFD model

Although commercial CFD techniques do not always predict heat transfer very accurately [28], trends predicted by CFD can be very useful. Therefore in order to

guarantee good CFD predictions, the model must be validated. Validation is generally done by experiment where key features of the flow field and heat transfer are measured and compared with the experimental results. Values of heat transfer coefficients (on both the end windings and the frame) and velocities around the end region, obtained by CFD and experimental techniques, were compared in this work to validate the CFD models.

5 Experimental Validation of CFD Models

In this chapter experimental results are presented. These are used to validate the CFD model, by comparing them with the CFD data. Velocity profiles, local and overall heat transfer coefficients and windage losses are used for the validation.

Through this validation exercise the best method of using CFD to model the end regions of TEFC induction motors is selected. The strengths and weaknesses of the modeling techniques are highlighted. Thus CFD models employing different turbulence models, solution methodologies, boundary conditions, etc are compared against experimental data and the most practical modeling technique chosen for the rest of the CFD modeling in this thesis.

For this validation phase an experimental rig having eight 50mm long square wafters is used as the basic ‘validation’ model. The heated end winding dissipates 50W of heat. The model runs at a constant speed of 1700 rpm. Another two models, one having no wafters and another having eight 100mm long by 50mm wide wafters are also used to complement this validation phase.

Additionally a section is dedicated to analyzing the flow field present in a typical end region of a TEFC induction motor.

5.1 Experimental results

Experiments were conducted as outlined in Chapter 3. The five hole probe was traversed axially at two locations:

1. Between the rotor end and the end windings at a radius of 160mm (referred to as reference plane 1 in Figure 5.1)

2. Behind the end windings at a radius of 305mm (referred to as reference plane 2 in Figure 5.1).

Results of velocity magnitudes from this experiment are presented below.

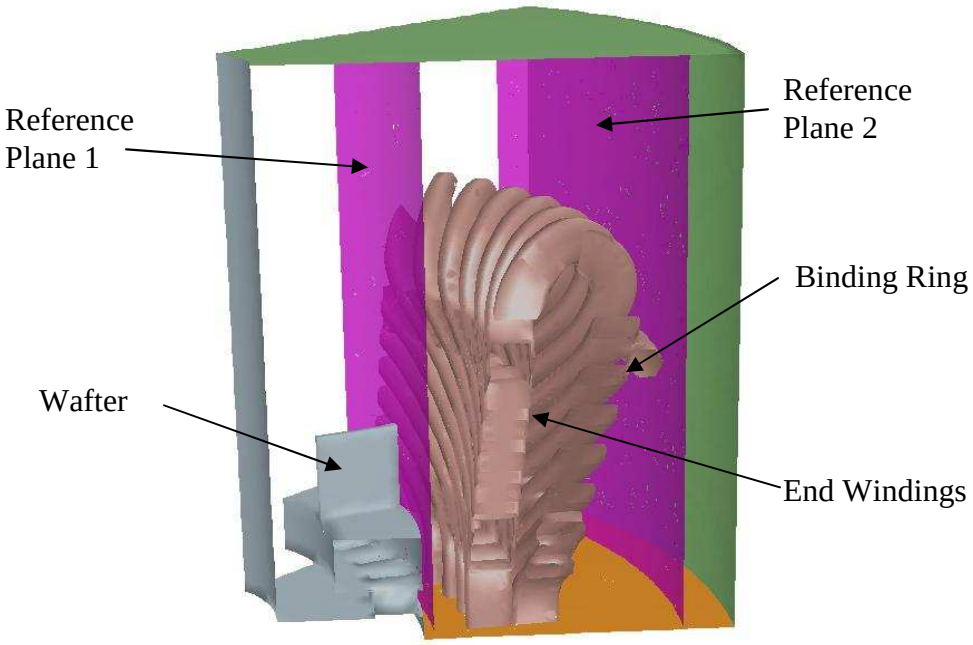

Figure 5.1 - CFD model used for validation exercise showing the two referenced planes where velocity magnitudes were measured using a 5 hole probe.

5.1.1 Velocity profile between rotor end and end windings

Since this study did not investigate turbulence intensities, the code controlling the time interval between readings taken from the 5 hole probe was designed with the intension to lower the uncertainty levels of the mean velocities by taking time averaged samples. Although this method increased the accuracy of the velocity magnitudes, the accuracy of the direction of the velocity was considerably

negatively affected especially in areas where large scale eddies were present (such as the area behind the end windings). This was justifiable because the 5 hole probe's frequency response is not fast enough to capture such unsteadiness. Therefore speed rather than velocity was used to validate the CFD model.

Results of velocity magnitudes measured on reference plane 1 are plotted against axial position in Figure 5.2. The locations of major features of the end region are also shown. There are two drivers forcing the air to recirculate around the end region and these are the wafters and the rotor bar extensions. The wafters exert the major influence, while the rotor bar extensions are a minor driver.

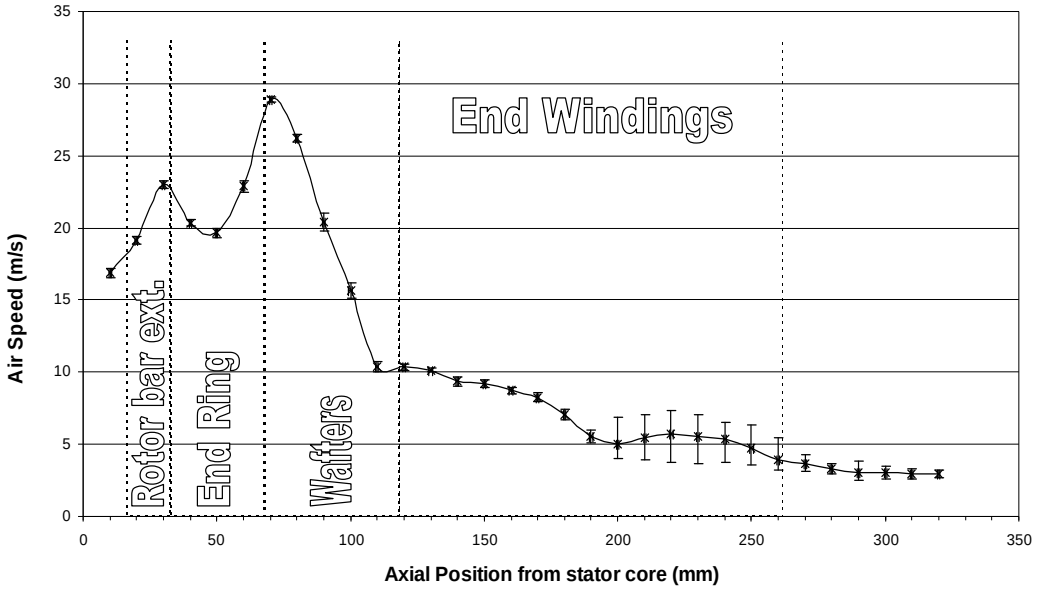

Figure 5.2 – Experimental velocity plots taken midway between the wafters and the end windings along reference plane 1

The graphs shows that the highest velocity is present at a point level with the base of the wafters. The velocity magnitude decays rapidly along the wafter length from around 29 m/s down to 10 m/s at the wafter tip. Velocities continue reducing, but

at a much slower rate, above the wafters in the end winding region. Midway along the end windings, the velocities experience a small increase in their magnitude.

Uncertainty bars have been added to each of the data points on the graph. These values were obtained as discussed in Section 3.3. Uncertainty analysis shows that velocities are quite stable everywhere except the area just below the end winding tips where, at these locations, the uncertainties are reasonably large. This coincides with the region where velocity magnitudes increased slightly. This increased uncertainty may be attributed to the mixing of air coming from behind the end windings with the wake above the wafters. This is considered in greater detail in Section 5.1.6.

5.1.2 Velocity profile behind the end windings

Results of velocity magnitudes measured on reference plane 2 (see Figure 5.1) are plotted against axial position in Figure 5.3

Velocities behind the end windings are substantially smaller than those present on the other side of the end windings in the area enclosed by them with a maximum value of 4.7m/s compared to 29m/s in the core. At the base of the end windings the velocity is higher than further away towards the end shield and this is due to the jet of air that emerges from the base of the end windings. This jet is driven mainly by the rotor bar extensions. Velocities decrease gradually along the end winding and then they start to increase again. This seems to happen due to the blockage effect the binding ring presents (see Figure 5.1 for binding ring location), forcing the air to accelerate as it flows past. In fact the highest velocity is present in the vicinity

of the binding ring. The velocity magnitude decays rapidly in the area above the end windings.

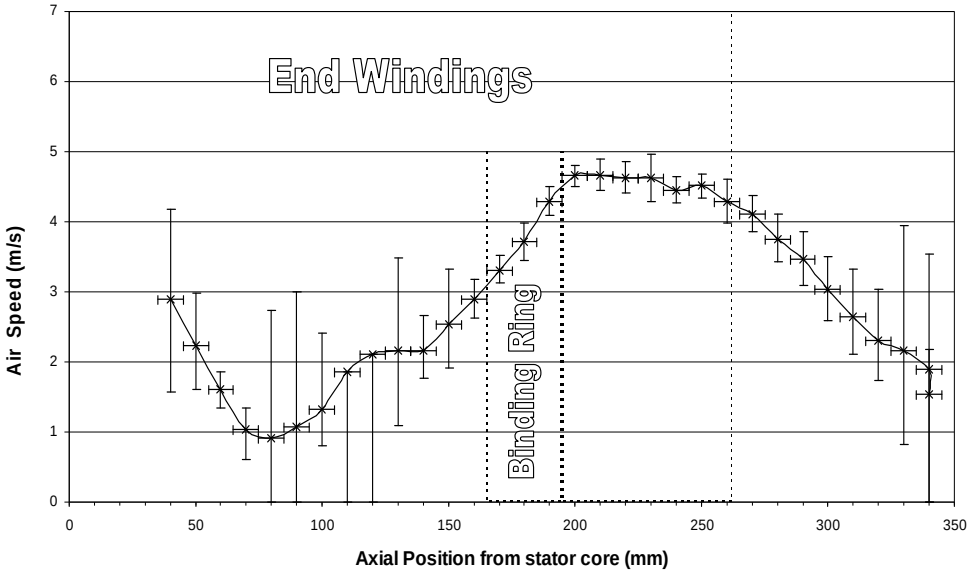

Figure 5.3 -Experimental velocity plots taken behind end windings along reference plane 2

Uncertainty analysis shows that velocities are quite unsteady in the lower area behind the end windings (relatively large uncertainties). This is due to the jet of air emerging from the base of the end windings being deflected by the frame along the end windings towards the end shield. In doing so it creates an area rich in large eddies.

5.1.3 Local Heat Transfer Coefficients

The distribution of the heat transfer coefficients over the whole surface of the end windings exposes the deficiencies of the flow field. Twenty five heat flux sensors were glued to the heated end winding at locations shown in Figure 3.5. Another 5 heat flux sensors were glued to the frame. Figure 5.4 shows the distribution of the

heat transfer coefficients on the heated end winding. Heat transfer coefficient was defined as shown in Section3.2. It is worth noticing the very high heat transfer coefficients on the surfaces where the air jet emerging from the rotating wafters, impinges on the surface of the end winding (locations 1, 3, 4 & 7).

It is also worth noticing the areas where the heat transfer coefficients are very low. In these areas the fluid velocity is also low as can be seen in Figure 5.2 and Figure 5.3 (top part of the end windings, locations 8-18).

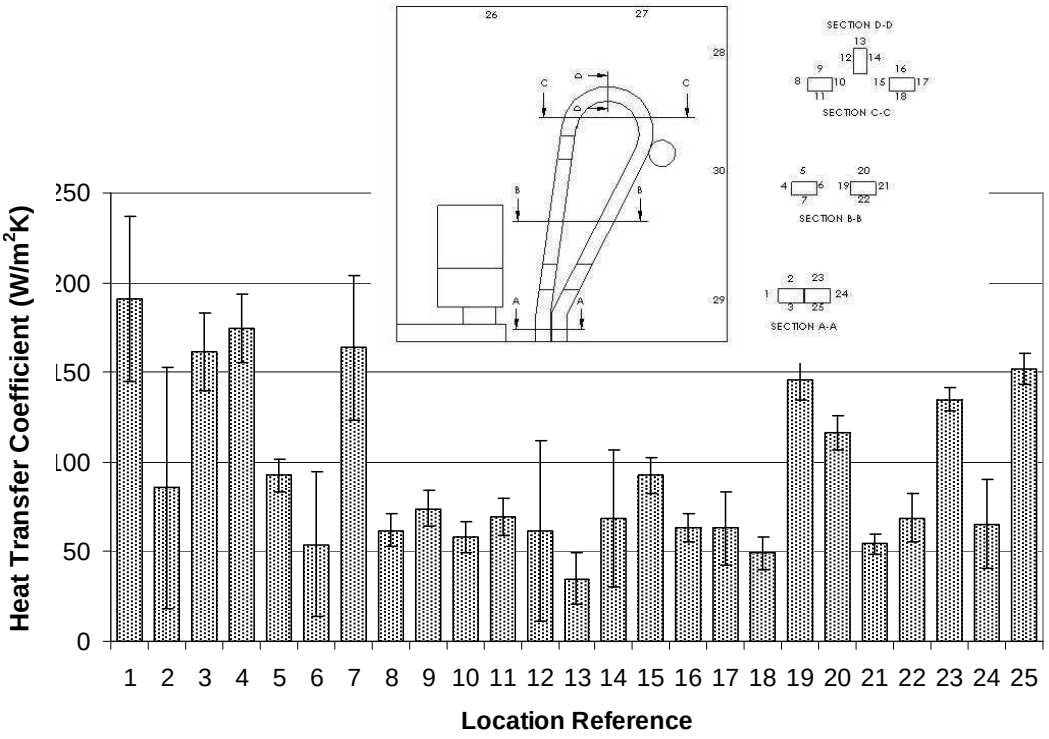

Figure 5.4 – Experimental values of local heat transfer coefficients on end windings

Figure 5.5 shows the heat transfer coefficients over the frame and endshield. The heat transfer coefficient is high where the jet of air penetrating the end windings impinges on the lower part of the frame (location 29).

In both of these figures, the heat transfer coefficients include the heat transfer by radiation ($Q''_{radiation}$ included). However when heat transfer coefficients are compared with CFD results, the heat transfer by radiation is removed from the measured heat transfer value in order to compare like with like (since radiation is not modelled in CFD).

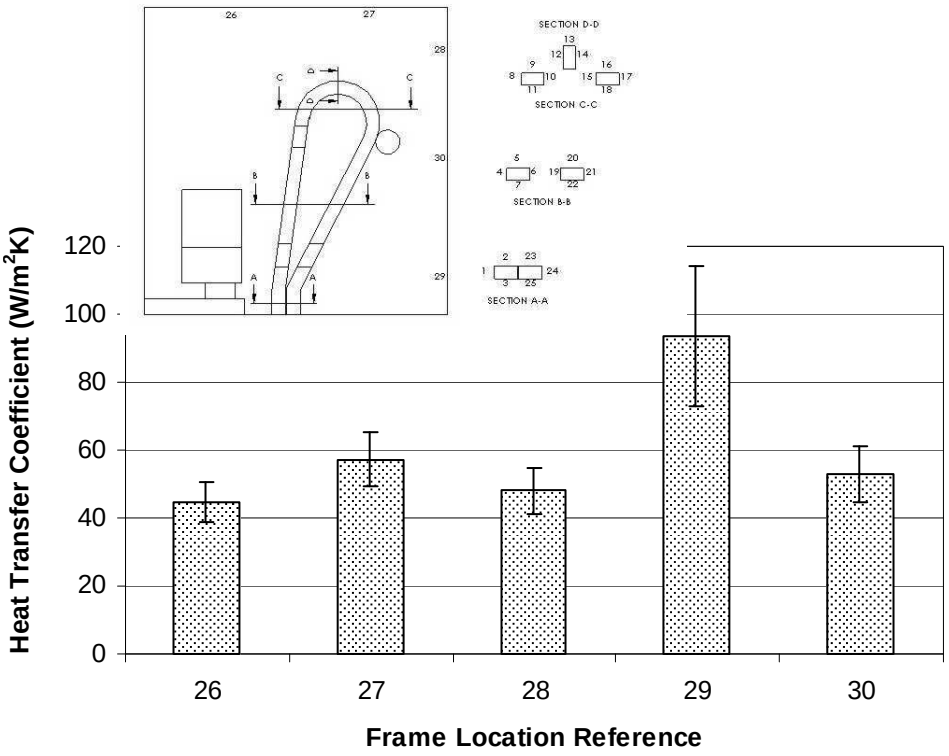

Figure 5.5 – Experimental values of local heat transfer coefficients on frame and end shield

As explained in Section 3.2.2, in order to reduce the uncertainty levels in the readings of the heat transfer coefficients over the frame and endshield, heater pads were used. These heater pads were glued to the frame's outside surface so as to provide a substantial heat flux and temperature difference between the frame surface and the bulk air. In order to further improve the uncertainty levels, the end winding was not heated at all during this experiment so as to keep the temperature

difference between the air surrounding the end region and the frame wall as high as possible. The impact this change brings about was investigated in detail using CFD modelling and is detailed in Section 5.2.3.

5.1.4 Overall Heat Transfer Coefficients

Although local heat transfer coefficient values are beneficial from a research point of view, an overall heat transfer coefficient may be the best guide to overall performance.

Overall heat transfer coefficients may be estimated by applying an area weighted averaging scheme but there are potentially several different approaches to this. A direct approach could be an area weighted average of the local heat transfer coefficients (i.e. $h = \frac{\sum (A_i h_i)}{\sum A_i}$).

Another approach is to calculate the overall heat transfer coefficient using area weighted averages of heat flux and surface temperature (i.e. $h = \frac{\sum (A_i Q^{"}_i)}{\left(\sum (A_i T_{w_i}) - T_{bulk} \sum A_i\right)}$).

The overall heat transfer coefficient may also be estimated by using the measured power input to the end windings and an area weighted average of surface temperature of the end winding (i.e. $h = \frac{P}{\left(\sum (A_i T_{w_i}) - T_{bulk} \sum A_i\right)}$).

It was established by experiment that the second method (that using area weighted averages of heat flux and surface temperature) gives more consistent results and consequently this method was used throughout.

The area weighted averaging scheme is still not a straight forward exercise. Due to the large differences in the local heat transfer coefficients, an appropriate area weighting scheme which assigned an appropriate area to each heat flux and temperature value had to be implemented . Since the geometry of the computer model was very accurately constructed, it was decided to use areas taken from the computer model rather than estimating areas from the end windings themselves. Thus the end windings were divided into twenty five zones, each zone surrounding each of the twenty five heat flux sensors as shown in Figure 5.6 .

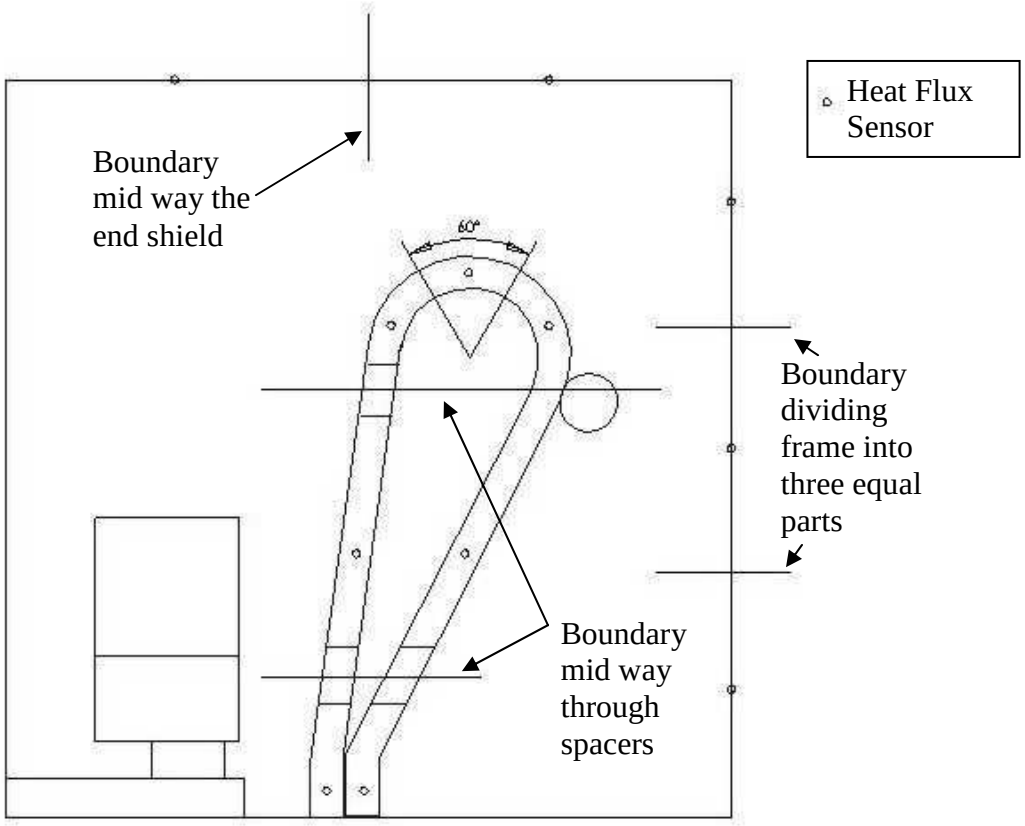

Figure 5.6 - Schematic showing boundary lines used to calculate areas in the area weighted averaging scheme for calculating the overall heat transfer coefficients of the end winding and the frame

Using the above area weighted averaging scheme the overall heat transfer coefficient of the end windings was calculated to be approximately 86±15W/m^{2}K.

The frame and endshield were equipped with a total of five heat flux sensors. A similar area weighted average scheme was used to arrive at an overall heat transfer coefficient of 58±9W/m^{2}K for the frame and endshield.

5.1.5 Windage Loss

The experimental rig has non-linear losses. Losses, such as frictional losses in the bearings vary with the temperature of the bearing. Thus it was very important to

measure the frictional losses in the initial stage of the experiment when the rig temperature was approximately equal to the ambient temperature. The other option was to measure the frictional losses when the temperature stabilises, however the time the rig takes to be thermally stable is very long (after three hours running, the rig still did not reach steady state conditions), which makes this option impractical.

Figure 5.7 shows a typical graph of mechanical power loss (frictional and windage losses) recorded along time. It shows that the mechanical power loss registered when the rig was cold was at a maximum value and therefore leads to an overestimate of the 'true' value.

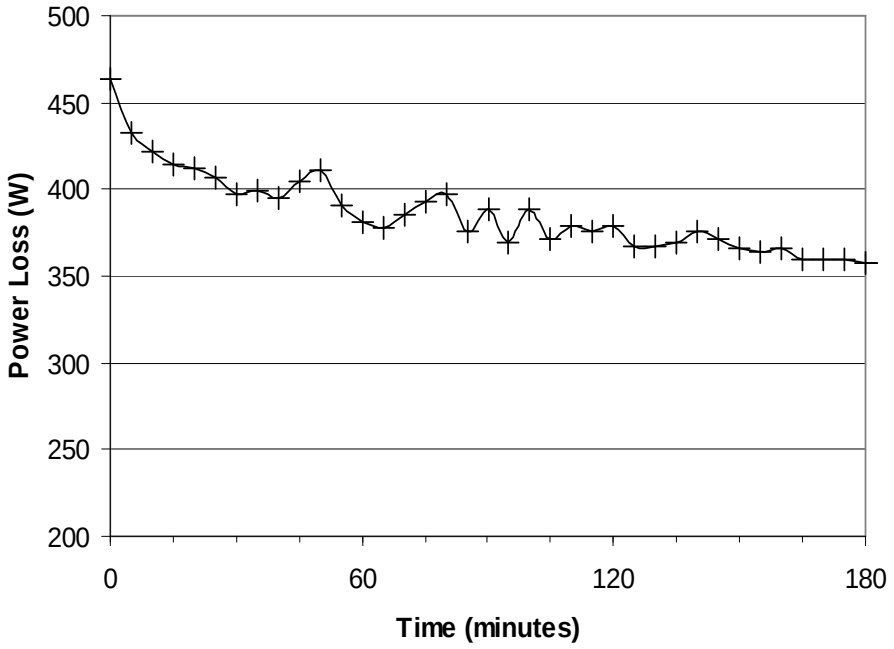

Figure 5.7 - Experimental value of mechanical power loss variation with time.

Additionally since the rig had to be disassembled and assembled again for every configuration change, it was practically impossible to obtain identical friction in

each experiment. Therefore a series of experiments had to be performed in order to arrive at the most realistic value of windage loss.

The average mechanical loss recorded for the basic validation model was approximately 405W ± 39W including frictional losses. To eliminate these extra losses and be able to assess windage losses due to the wafters alone, the experiment was re-run with the wafters removed. A mechanical power loss of 190W ± 22W was recorded. This means that the windage loss due to the wafters is 215W ± 32W. This is a substantial loss which should not be neglected when designing an electric motor and should be given proper attention.

5.1.6 Overview of Flow Field in end region

Figure 5.8 shows the general flow field as visualised using cotton tufts attached to a stick and positioned inside the end region. Apart from the strong circumferential swirl, there is a strong secondary recirculation above the wafters. Furthermore there is a weaker recirculation emerging from the rotor bar extensions, penetrating the lower parts of the end windings and flowing upwards behind the end windings to combine with the main recirculating air above the wafters.

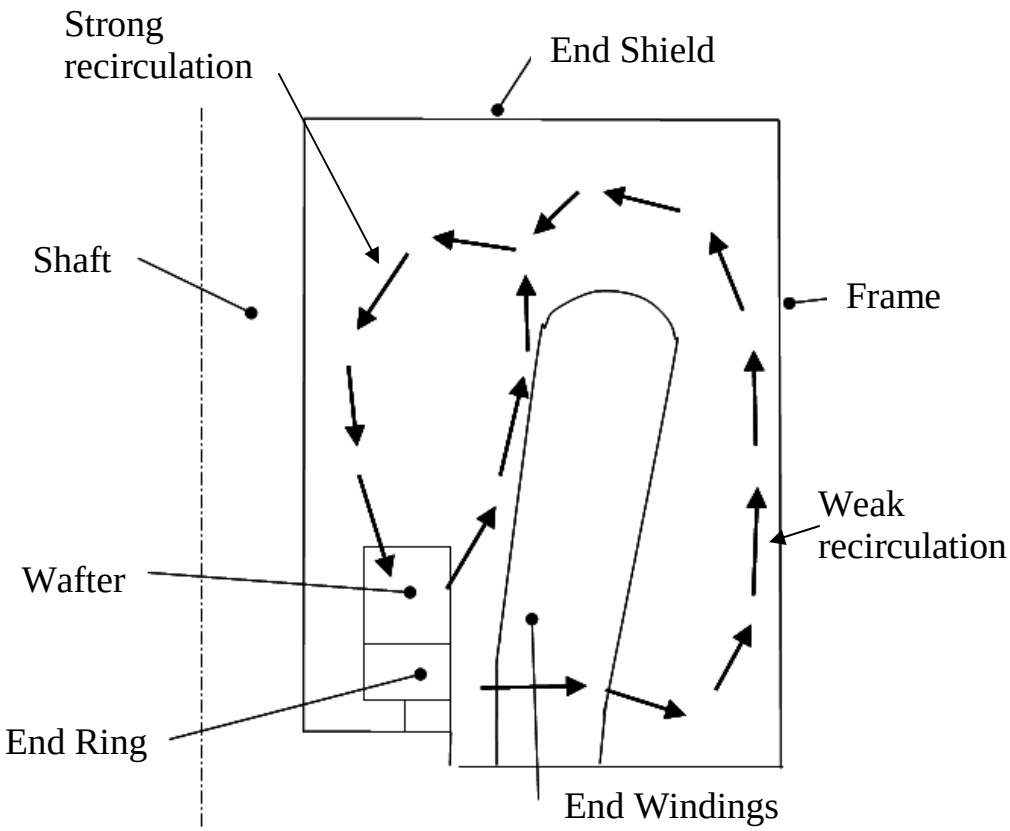

Figure 5.8 - General flow field in the End Region

5.2 Validation of CFD data

In this section, the experimental results presented in the previous sections will be compared to the data calculated from the CFD model used for the validation phase. Through this exercise, the capabilities and deficiencies of the commercially available CFD techniques will be assessed. Additionally various turbulence models, solution methodologies and types of boundary conditions will be evaluated. Figure 5.9 illustrates one typical solid model which was used in the CFD analysis.

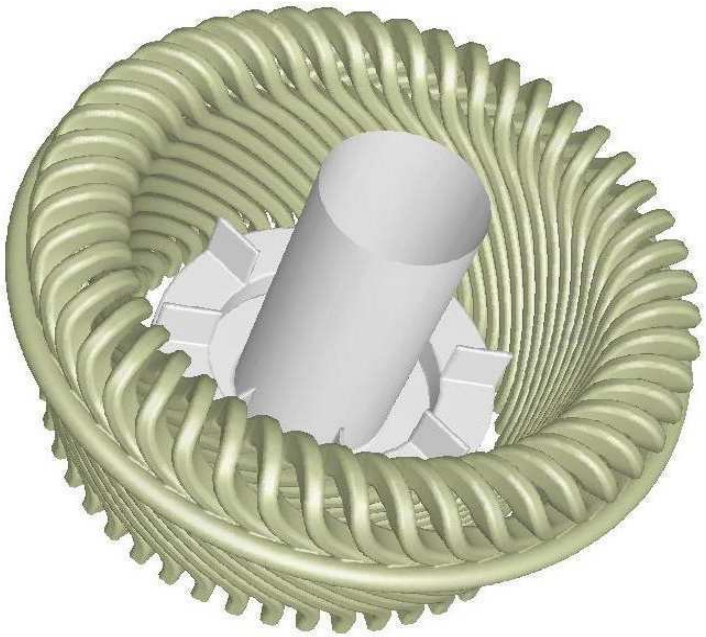

Figure 5.9 - Typical computer model of the end winding used for CFD analysis

5.2.1 Building the Solid Model

As mentioned earlier in Section 4.2.2, the grid generator approximates all curved edges of the solid geometry into a series of straight lines. The grid scale determines the length of these straight lines. Since the wall functions impose a minimum limit on the size of the cells in the vicinity of the walls, all rounded corners will be approximated into sharp edges. As illustrated in Figure 5.10 this will affect the fluid flow since the radius of curvature of corners dictates the extent of flow separation. Sharp corners tend to produce larger flow separations compared to smooth corners and thus place the reattachment point further away from the corner causing more blockage.

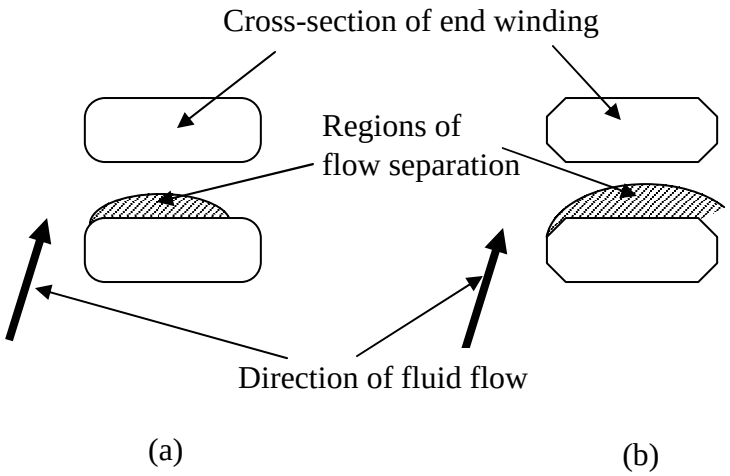

Figure 5.10 – Effect of sharp corners on flow separation.
(a**) original smooth corners creating moderate blockage (b) modeled sharp corners creating a larger area of flow separation where the reattachment point extends further away from the corner creating larger blockage effects.**

Allowance has to be made in order to allow for the anticipated higher blockage effect. To compensate the extra blockage effect, the end windings need to be made thinner so that the passage width is increased.

CFD techniques were used in order to verify this phenomenon. Figure 5.11 shows the cross-sections of the two end windings which were used in the CFD models. The left hand side shows the cross-section of the end windings having the same width as the ones on the experimental rig. The right hand side shows the cross-section of the slightly thinner end winding to compensate for the higher blockage effect.

(a) (b)

Figure 5.11 - Cross-section of End Windings (a) original size (b) thinner to compensate for higher blockage effect

Using CFD, an iterative process was employed to establish an end winding width which best represents the real end windings. The local heat transfer coefficients were used to assess the most appropriate CFD representation. Figure 5.12 shows the experimental results of the local heat transfer coefficients on the end windings alongside the results extracted from the CFD data. It is quite clear that the modelling philosophy employed to the end windings in order to compensate for the higher blockage effect was justified, since the heat transfer coefficient data using the thinner representation of the end winding matches more closely to the experimental results.

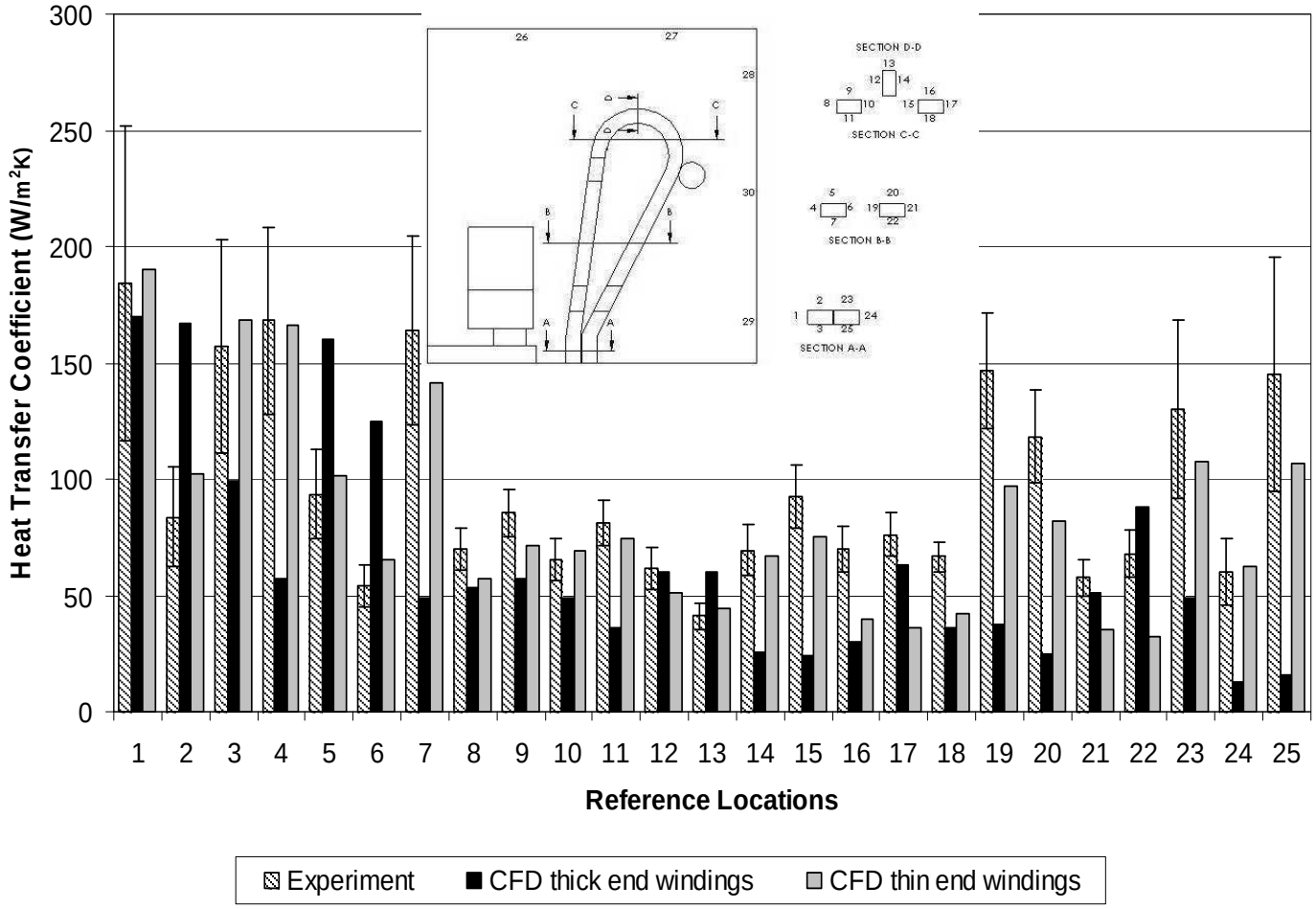

Figure 5.12 – Effect of sharp corners on the Local Heat Transfer Coefficients on End Winding

The objective to increase the through flow by reducing the end winding width was achieved, as illustrated on the velocity vector plots shown in Figure 5.13. The left hand plot shows velocity vectors taken from the model having end winding dimensions the same as the experimental rig, while the right hand plot shows velocity vectors taken from the model having thinner end windings. In the left hand plot the air is contained in the space above the wafters and the resistance to flow through the end windings is considerable, inhibiting the through flow. Velocity vectors in this area are short indicating that their direction is perpendicular to the plane of the paper (circumferential swirl). The resistance to flow in the right hand plot is much less, allowing more air to penetrate the end windings. Velocity vectors in this plot are relatively longer indicating the flow to be now in the plane of the paper.

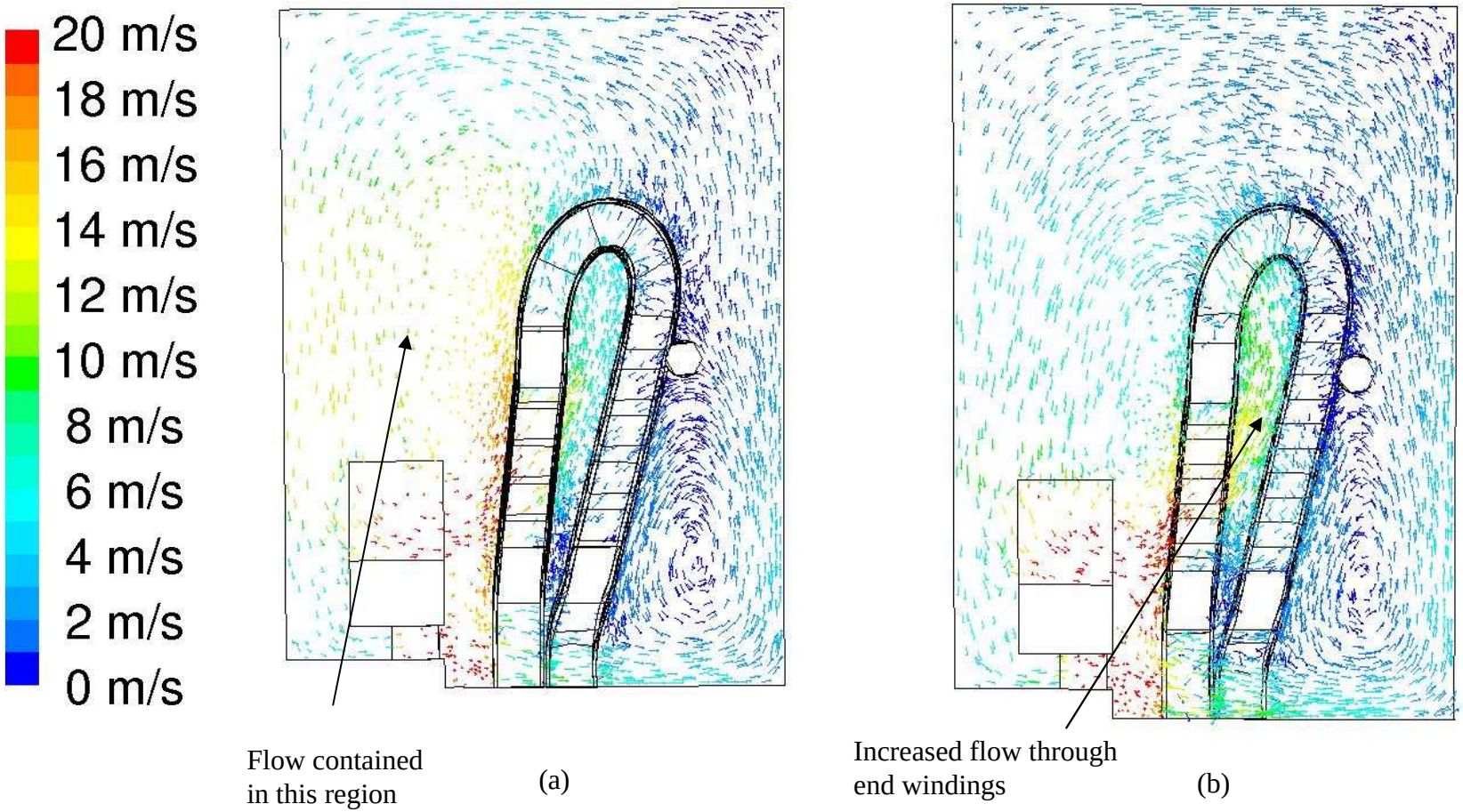

Figure 5.13 – Velocity vector plots showing more flow though end windings as a result of thinner end windings (a) CFD model using original size end windings (b) CFD model employing thinner end windings

5.2.2 Velocity profile

In this section the velocities predicted by the CFD calculations will be compared with the experimental results. Circumferential averaged velocity profiles on reference planes 1 and 2 (Figure 5.1) will be used for this analysis.

Velocity profile midway between wafter and end windings

Velocity magnitudes along reference plane 1 are plotted in Figure 5.14 for various cases employing different turbulence models and compared to experimental results.

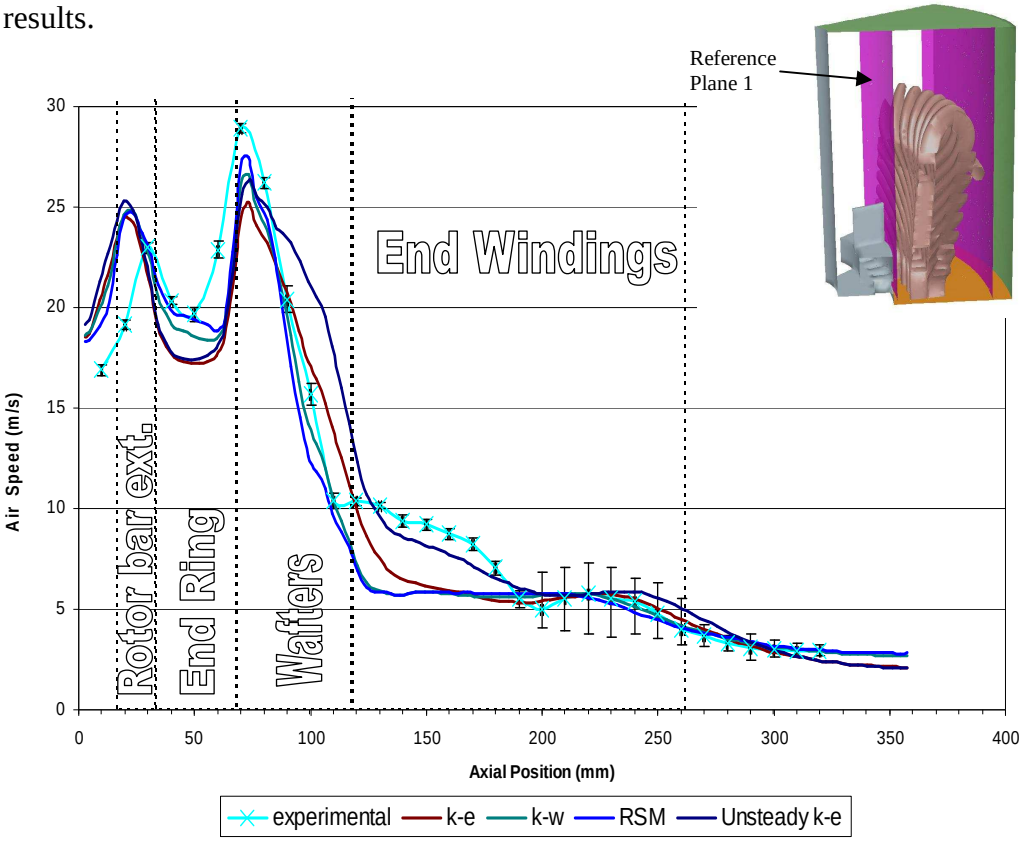

Figure 5.14 - Velocity magnitudes along reference plane 1

It is interesting to observe that, in general, all turbulence models predict the velocities quite well. However, in the wake area above the wafters blades, predictions of velocity magnitude are not satisfactory for steady state solutions.

When using the time dependent solver (unsteady k-ε), the predictions were far better. Therefore one may conclude that the mismatch in velocity magnitudes, in the wake area above the wafter blades, is due to the unsteady nature of the flow which the steady state solver is unable to resolve. A time dependent solution however takes much longer (of the order of ten times longer) to converge than a steady state solution. This time factor outweighs the benefits of predicting the velocity magnitudes more accurately, by employing a time dependent solution. As will be shown in the following sections, predictions of the heat transfer coefficients are acceptable even when using steady state solvers.

It is also interesting to note the level of agreement between the k-ω and the RSM models. The k-ω turbulence model is simpler and requires less time to solve than the RSM turbulence model, which makes it superior to the RSM turbulence model in this situation.

Velocity profile behind the end windings

Velocity magnitudes on reference plane 2 are plotted in Figure 5.15 for various cases employing different turbulence models along with experimental results.

This time none of the turbulence models predict the velocities in the region behind the end windings well, especially near the end winding tips where the secondary recirculating flow mixes with the primary swirling flow.

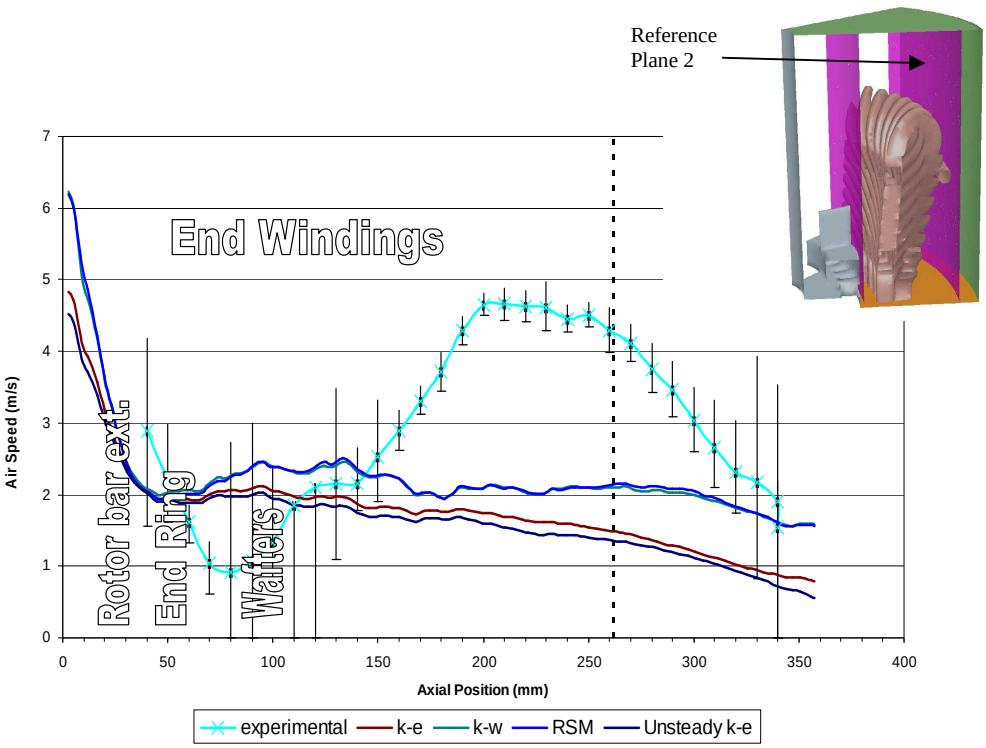

Figure 5.15 – Velocity magnitudes along reference plane 2

Various attempts were made to try to overcome this problem by constructing the CFD model with a geometry as close as possible to that of the experimental rig. Unfortunately all attempts were unsuccessful. The only geometrical factor which influenced the flow pattern considerably was the position of the lower spacers separating the end windings from each other. This will be dealt in more detail in Chapter 7. All other improvements made to the geometry of the model (such as twist angle of end windings, profile of end winding, etc) did not give rise to a closer match between the experimental results and the CFD data.

Although it is quite difficult to explain why the CFD code was unable to adequately predict velocities behind the end windings, it is thought that this may be due to the inability of the RANS turbulence models employed, to model the highly turbulent nature of the flow present in the region. Wang et al.[32] and Sun et al.[33] also experienced similar problems when using RANS turbulence models.

The computer resources and time available for this research did not allow for more advanced turbulence models, such as LES turbulence model which was described in Section 4.1.2, to be employed.

5.2.3 Local Heat Transfer Coefficients

In this section the local heat transfer coefficients predicted by the CFD calculations are compared to the experimental results. The next two sections will detail this comparison for the end windings and the frame respectively.

The average relative deviation from the experimental results is used to quantify how good the CFD data matches the experimental results. As illustrated in Figure 5.16, relative deviation from the experimental result was defined as equal to zero if the CFD prediction is within the experimental uncertainty band otherwise it is equal to the ratio of the absolute minimum difference between the CFD prediction and the upper and lower limits of the experimental uncertainty band to the experimental mean.

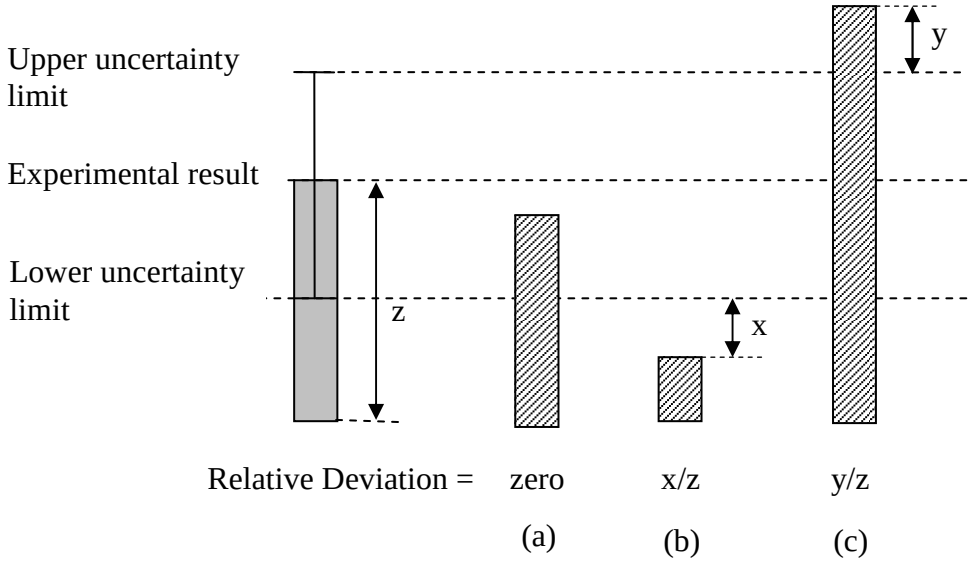

Figure 5.16 – Definition of deviation from experimental result
(a**) Within experimental uncertainty – Relative deviation = 0**
(b) Below experimental uncertainty – Relative deviation = x/z
(c) Above experimental uncertainty – Relative deviation = y/z

Local heat transfer coefficient on the end windings.

The local heat transfer coefficients on the end windings calculated using CFD techniques are plotted alongside the corrected experimental results (with heat transfer due to radiation removed) in Figure 5.17. Overall the local values agree well with the experimental results.

Final choice of turbulence model

Figure 5.18 shows that the case having the minimum average relative deviation was that employing the standard k-ε turbulence model. This strengthened the decision taken earlier to employ the k-ε turbulence model in the rest of the CFD work.

The model employing the k-ε turbulence model was the fastest to converge. Moreover, the grid required by the k-ε turbulence model, to obtain grid independent solutions, was coarser than that required by the other turbulence models. Therefore since the majority of time was dedicated to testing modifications to the end region in order to assess any improvements in the heat transfer, the time factor was important and it was decided to employ the k-ε turbulence model in all further work.

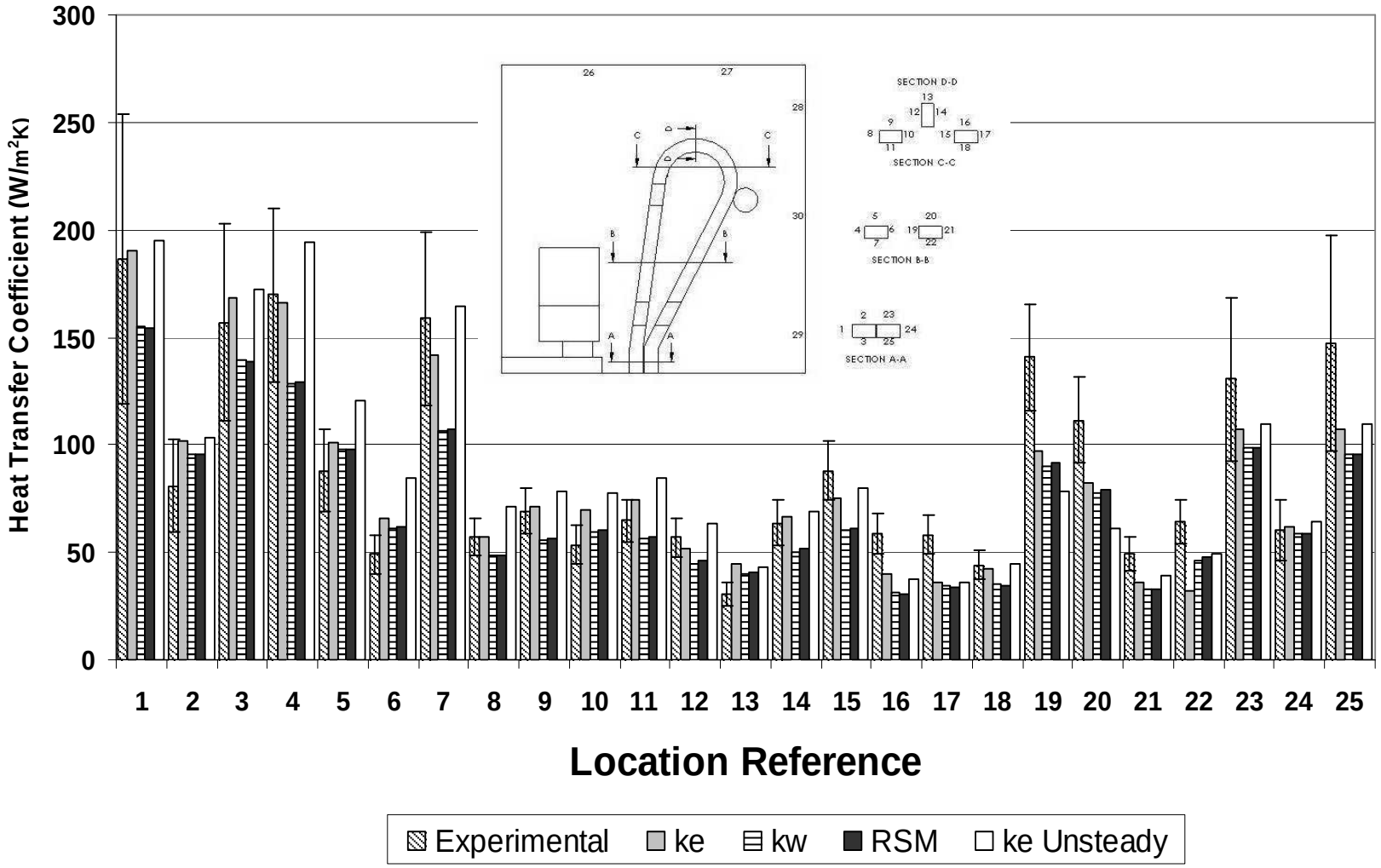

Figure 5.17 - Local Heat Transfer Coefficients on End Winding

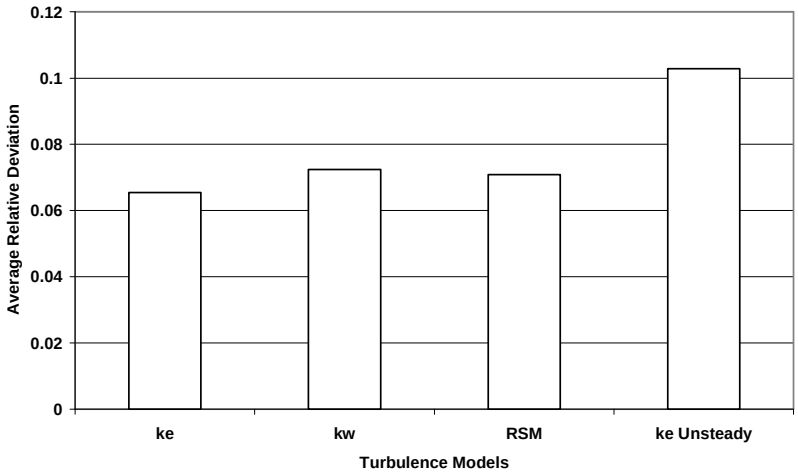

Figure 5.18 – Average relative deviation of CFD predictions of local heat transfer coefficients on the end winding with respect to experimental results using various turbulence models.

Effect of boundary condition

The boundary condition that best represents the real situation was also assessed. Three different boundary conditions were compared for the end winding surface; one model having the end winding surface at constant temperature, another emitting a constant heat flux and a third in which conduction in the end winding copper was also modelled. The copper was made to generate heat in each cell that varied linearly with its temperature. The first model was the most simple whilst the last model, which modelled also conduction through the solid end winding, was the most complex.

The results of this analysis are shown in Figure 5.19 and there was little difference in the reported heat transfer coefficients. This result was as anticipated because turbulent heat transfer at high Reynolds number is mainly dependent on the fluid flow and not the thermal conditions.

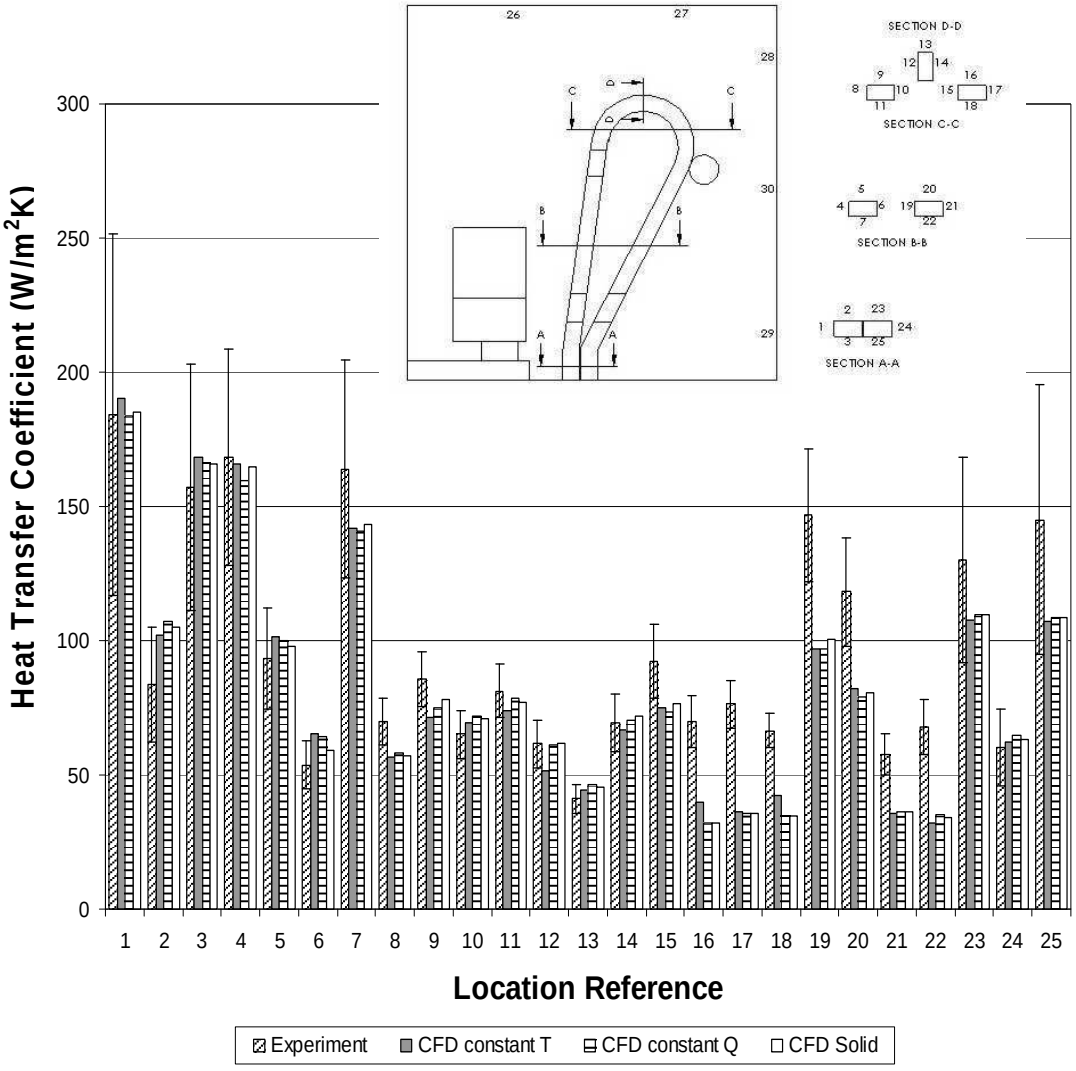

Figure 5.19 - Local Heat Transfer Coefficients on End Winding

In order to get a better picture of the local heat transfer distribution on the end winding, a contour plot of the heat transfer coefficient on an end winding is depicted in Figure 5.20.

Further analysis of Figure 5.20 reveals that the heat transfer coefficients are high in areas where the velocity is high (inner surfaces of end windings). Although this seems fairly obvious, it is a very important feature worth noticing for end region design purposes.

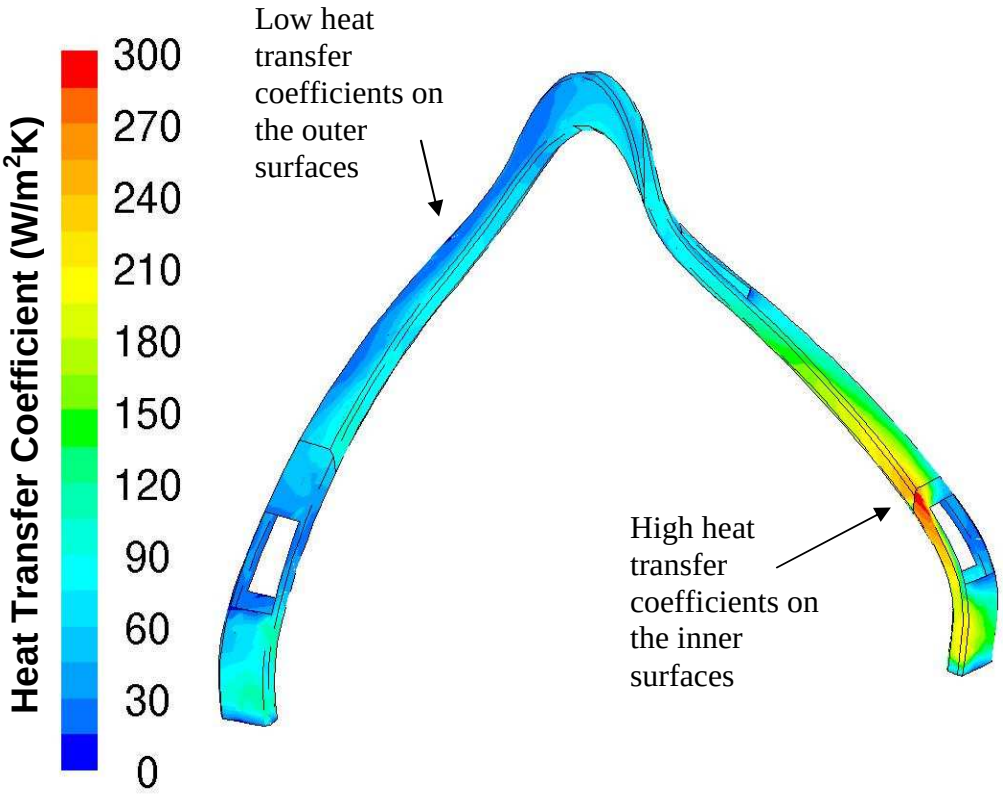

Figure 5.20 - Contour plot of local Heat Transfer Coefficient on End Winding

Local heat transfer coefficients on the frame and end shield

The experimental local heat transfer coefficients for the frame and end shield are plotted in Figure 5.21 alongside the heat transfer coefficients calculated from the CFD data for cases employing different turbulence models. The CFD predictions have a large discrepancy when compared with the experimental data. This may be attributed to the flow behind the end windings not being predicted correctly by the CFD since the velocity profile behind the end winding also showed a high level of disagreement (refer to Section 5.2.2). It may also be due to different heating arrangements between the experimental model (refer to section 3.2.2) and the CFD model.

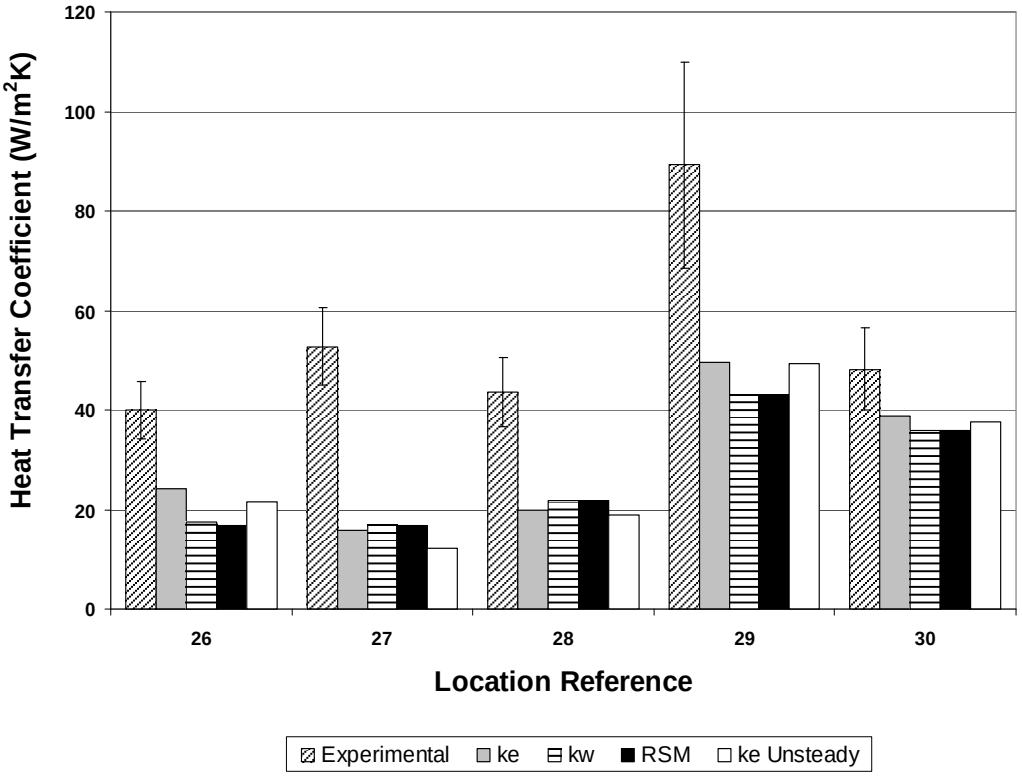

Figure 5.21 - Local Heat Transfer Coefficient on Frame/End Shield

In order to assess further the latter probable cause for this mismatch a simple study was performed using CFD to assess the effects of the different heating arrangements on the heat transfer coefficients. Thus CFD cases were set up to model a frame having a heat flux flowing towards the end region space. It emerged that the heat transfer coefficients were not influenced by the way the heat was flowing.

Having eliminated one of the suspected causes for this mismatch, it was concluded that the CFD code was not resolving the flow field accurately enough behind the end windings. This deduction is strengthened by the fact that the velocity profile behind the end windings was also not being predicted to a desired level of

accuracy. Again the k-ε turbulence model gave the best results as shown in Figure 5.22.

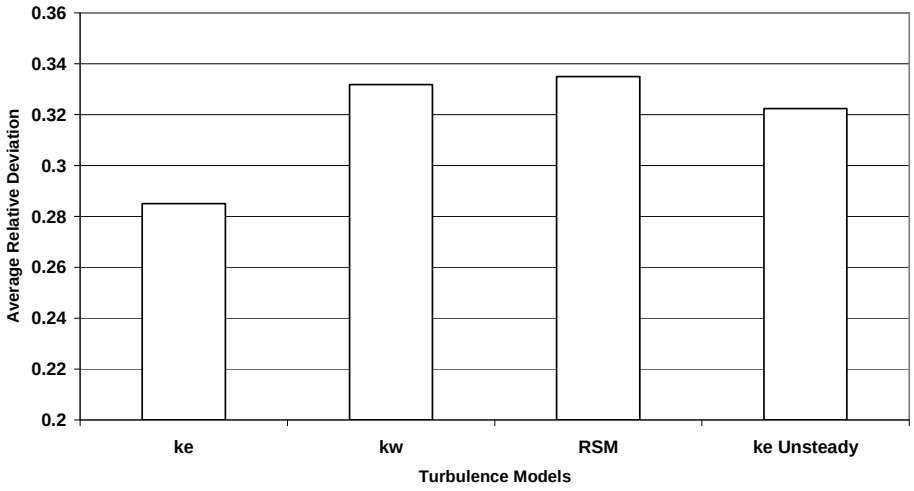

Figure 5.22 – Average relative deviation of CFD predictions of local heat transfer coefficients on the frame and end shield with respect to experimental results using various turbulence models.

General Comments

As with the velocity profiles, when local heat transfer coefficients are considered, it is found that the k-ε turbulence model gave results closest to the experimental and also achieved grid independence on a coarser grid (therefore faster to converge). Moreover this study highlighted the fact that CFD employing commonly available RANS turbulence models is unable to resolve the flow field behind the end windings. This gives rise to large discrepancies in the heat transfer coefficient of the frame and end shield. Although a number of methods were implemented to try to rectify this problem a solution was not found. However a decision was taken to continue the research bearing in mind the inability of the CFD to solve the flow field in the region behind the end windings may affect some of the data for that region. It was decided that a final validation of the results

achieved through the CFD enhancement exercise had to be employed in order to experimentally confirm such enhancement.

5.2.4 Trends in Overall Heat Transfer Coefficients

In order to understand how CFD predictions might be used to assess further developments, the study was extended to investigate trends in overall heat transfer coefficients. This was done by performing experiments and solving CFD models with different wafter lengths (since the wafters were the main driving force). Consequently, two more models (both experimental and CFD) were used, one having no wafters at all and another having eight 100mm long wafters. The area weighted method described in Section 5.1.4 was used to calculate values of overall heat transfer coefficients.

Overall Heat Transfer Coefficient of the end windings

Figure 5.23 compares experimental results with results calculated from CFD data for heat transfer coefficients on the end windings when different wafter lengths were used. The results from the CFD data are all within the experimental uncertainty band. The trends in overall heat transfer coefficient on the end windings are also encouraging.

As there is good agreement between CFD and experiment, both in terms of prediction of absolute overall heat transfer coefficient and trends, this gives confidence in the use of CFD to model end windings.

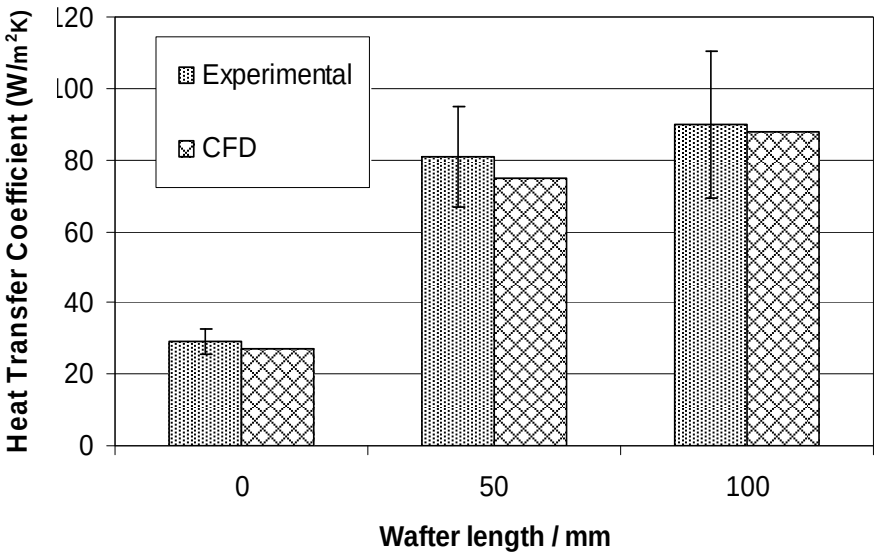

Figure 5.23 - Overall Heat Transfer Coefficients of End Windings

These results had no influence on the choice of area weighted method, which is simply based on areas in close proximity to each sensor, as outlined in section 5.1.4. In fact they were obtained after the area weighted method was chosen. The results therefore suggest that CFD accurately models the experimental values of overall heat transfer coefficient on the end windings, even when major features are altered.

Overall Heat Transfer Coefficient of the frame and end shield

Since the local heat transfer coefficients on the frame and endshield were not predicted very well, it was expected that the overall heat transfer coefficient would not be predicted with high accuracy. The discrepancy was quite large as shown in Figure 5.24. Trends are also not very well predicted. The only thing this data may be used for is to predict improvements but not their magnitude. It is suggested that

if this data is utilised in design, it should be validated through experiment in order to confirm its validity.

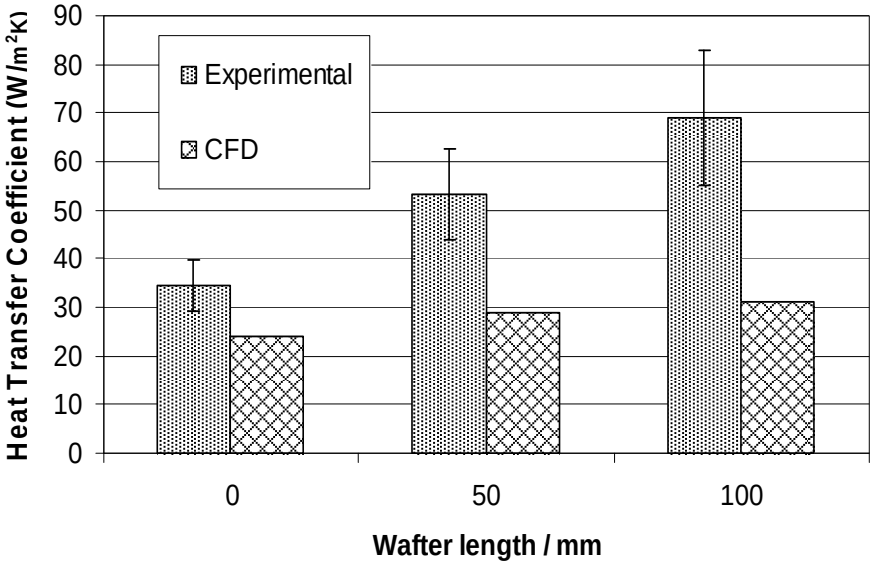

Figure 5.24 - Overall Heat Transfer Coefficient on Frame/End Shield

5.2.5 Assessment of steady state vs time dependent solutions

Figure 5.25 shows a typical monitor of the overall heat transfer coefficient of the end winding reported by the time dependent CFD solver while solving the model. The time dependent solver was started with initial conditions taken from a steady state solution. This plot shows that the steady state solver's heat transfer coefficient predictions are in agreement with the time dependent solution. Additionally it also shows the periodicity (wafter passing frequency) of the unsteadiness the time dependent solver is capable to resolve when the time step resolution is sufficiently smaller than the wafter passing frequency.

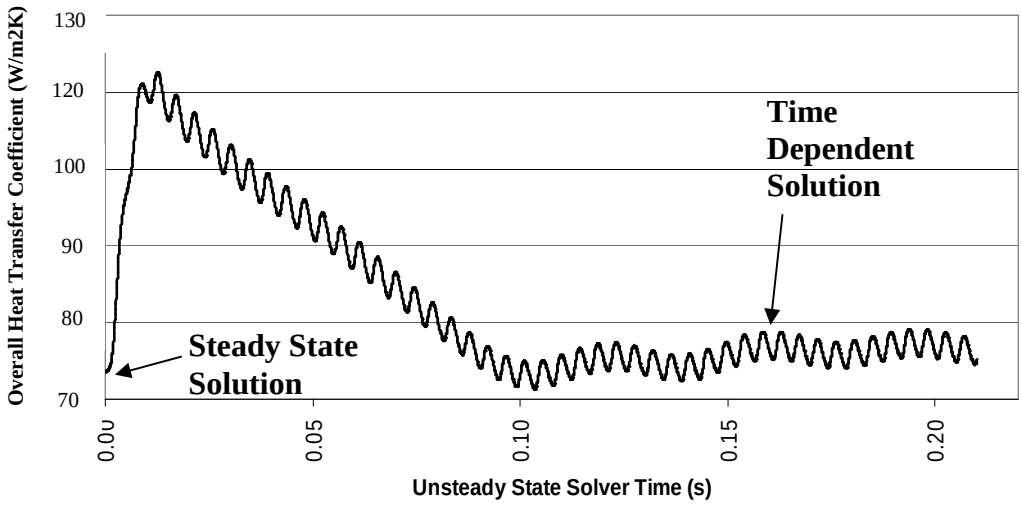

Figure 5.25 - Overall Heat Transfer Coefficient of End Winding vs Solver Time

A time dependent solution takes a long time (of the order 20 times longer than a steady state solution) to arrive at steady periodic conditions. As the steady state solution is so similar to that obtained using the time dependent solver, it was judged that there was little benefit in the expensive time dependent solution and steady state analysis was used for all subsequent investigation.

5.2.6 Windage Power Loss

The CFD models also predict windage power losses (due to drag). Figure 5.26 shows the measured mechanical losses alongside predicted windage losses.

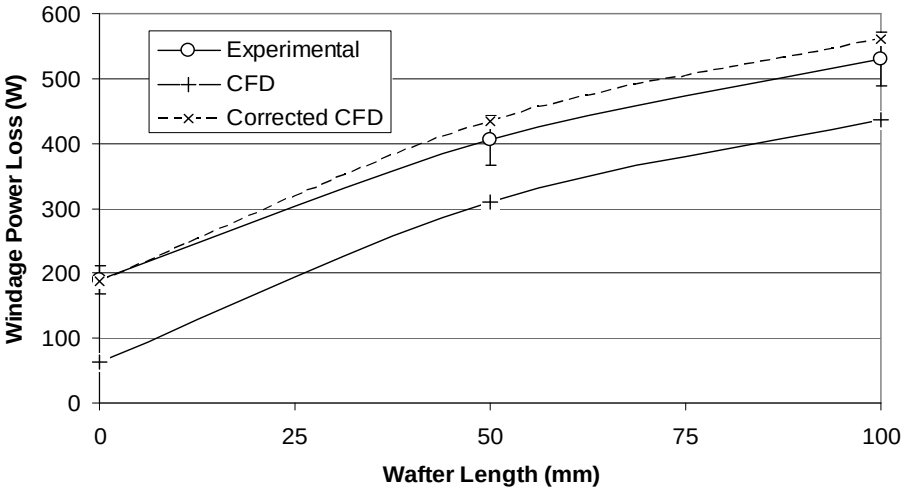

Figure 5.26 - Windage Power Loss

Figure 5.26 shows that both experimental and CFD data sets show the same trend but with an almost constant offset. This is due in part to the fact that the experimental data includes bearing losses. The case with no wafters can be used to estimate these losses and these are estimated to be 125W. When these estimated bearing losses are added to the CFD data the resulting corrected CFD data falls within the uncertainty bands for the experimental data as illustrated in Figure 5.26. Essentially this confirms that the CFD can be used for windage power loss predictions.

5.2.7 Overview of Flow Field in end region

One of the most useful features of CFD modelling is the capabilities of the post-processing to show features of the flow field that are very difficult to observe experimentally. Figure 5.27 illustrates this. It shows a meridional velocity vector plot superimposed on path line tracks. This plot confirms the main flow characteristics which were investigated in the experimental part using cotton tufts.

Again there is a main recirculating flow over the wafters and another weaker recirculating flow past the end windings, up behind the end windings and then joining the first recirculating flow above the end winding space.

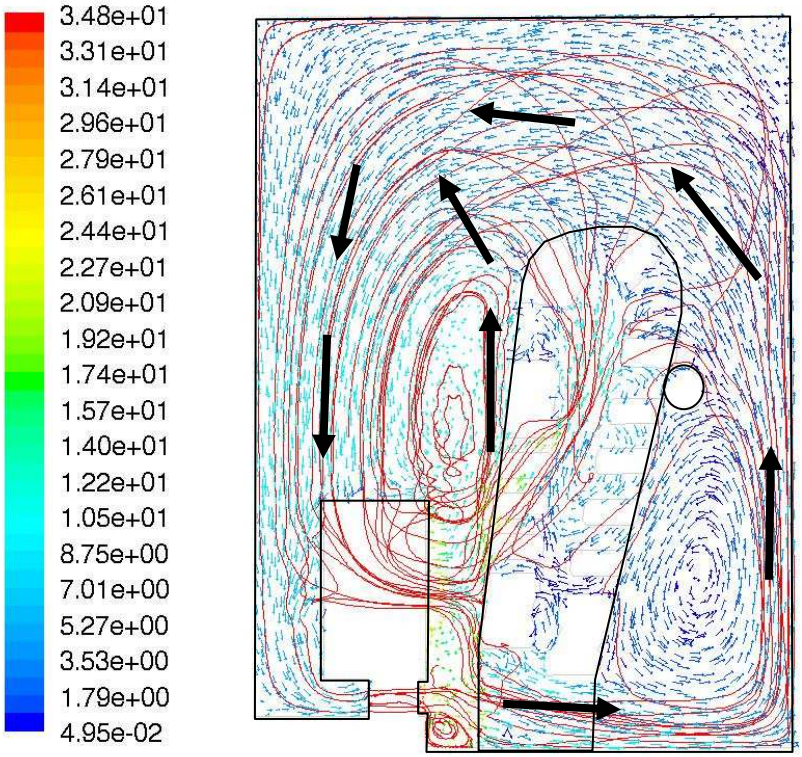

Figure 5.27 - Velocity vector plot including path lines

5.3 Conclusions

The main conclusions are:

1. End regions of TEFC induction motors can be successfully modelled using CFD by employing:

    - The standard k-ε turbulence models
    - Constant wall boundary conditions

- Moving reference frame technique.

2. Flow field predictions are reliable and help to visualise the flow field present in the end region of TEFC induction motors.

3. Overall heat transfer coefficients on the end windings can be predicted precisely (within the experimental uncertainty bands).

4. Overall heat transfer coefficients on the frame and end shield are not predicted well and therefore results should always be experimentally validated.

5. Windage loss predictions are precise (within the experimental uncertainty band).

In order to compare the overall heat transfer coefficient of the base case model (having 50mm long wafters) with the published literature, the end winding envelope area needs to be defined. Thus referring to Figure 5.28, the end winding envelope area may be defined as

$$A_{envelope} = (\text{End winding perimenter}) * (2\pi * (\text{End winding average radius}))$$

Then the corrected overall heat transfer coefficient may be defined as

$$htc_{corrected} = (\text{overall htc}) * (\text{area of end windings}) / (A_{envelope})$$

In the end winding used in this investigation, the area of the end windings was estimated to be $2.133m^2$ while the envelope area was estimated to be $0.852m^2$.

Therefore the corrected overall heat transfer coefficient of the base case model equates to 215W/m^{2}K.

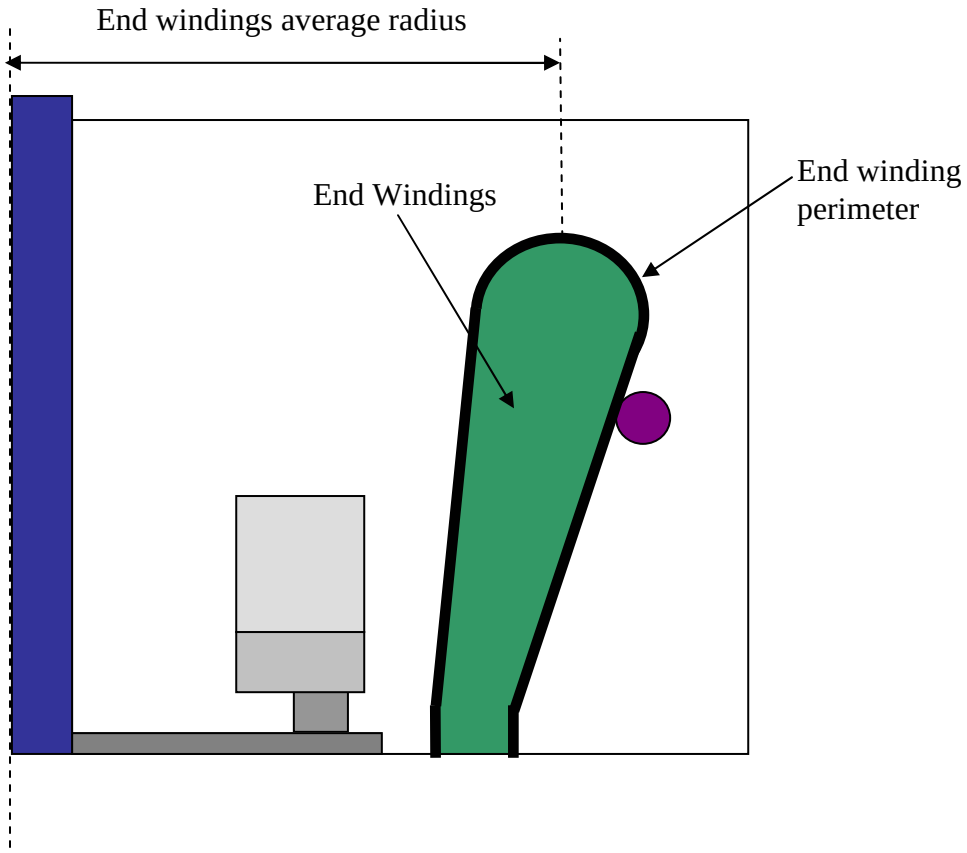

Figure 5.28 – Definition of end winding envelope area.

Using Scubert's[20] proposed correlation (refer to equation 3.1) for the end winding heat transfer coefficient, a value of 140 W/m^{2}K is obtained. Therefore the value obtained in this investigation does not compare well with the value calculated using this correlation. The main reason for this disagreement is due to geometric differences in the end windings. The end windings being investigated in this work are of the formed type (generally used in medium to high voltage applications) while the end windings used by Schubert[20] were of the wire wound type (generally used in low voltage applications). This emphasizes the fact that

end windings of large machines in particular, such as high voltage machines, require proper CFD or experimental analysis in order to arrive at a reasonable value for its heat transfer coefficient.

Thus as a final comment a great deal of confidence was gained in using the commercially available CFD techniques. Strengths and weaknesses have been identified which will help assess further development using CFD.

6 Parametric study of End Region Configuration Changes on Simplified Models

In this section, the end region of a TEFC induction motor is represented by simplified models. These models have been used to investigate the effect of end region configuration changes on the fluid and heat flow fields. These configuration changes were:

- Frame clearance
- Endshield clearance
- Oblique wafters
- Shrouded wafters
- End winding inclination in the radial plane

The simplifications employed in these models consists of two rows of columns replacing the end windings. Figure 6.1 illustrates one such model. These columns were 260 mm long and 15 mm wide in order to represent the same dimensions as the end windings present in the validation model. The outermost surfaces of the columns were at a radius of 211 mm and the gap between the two columns was 5 mm. The column dimensions were kept constant in all models. The temperature of the columns was set at 140^{o} Celsius while the frame and end shield temperatures were set at 20^{o} Celsius. All other walls were set adiabatic.

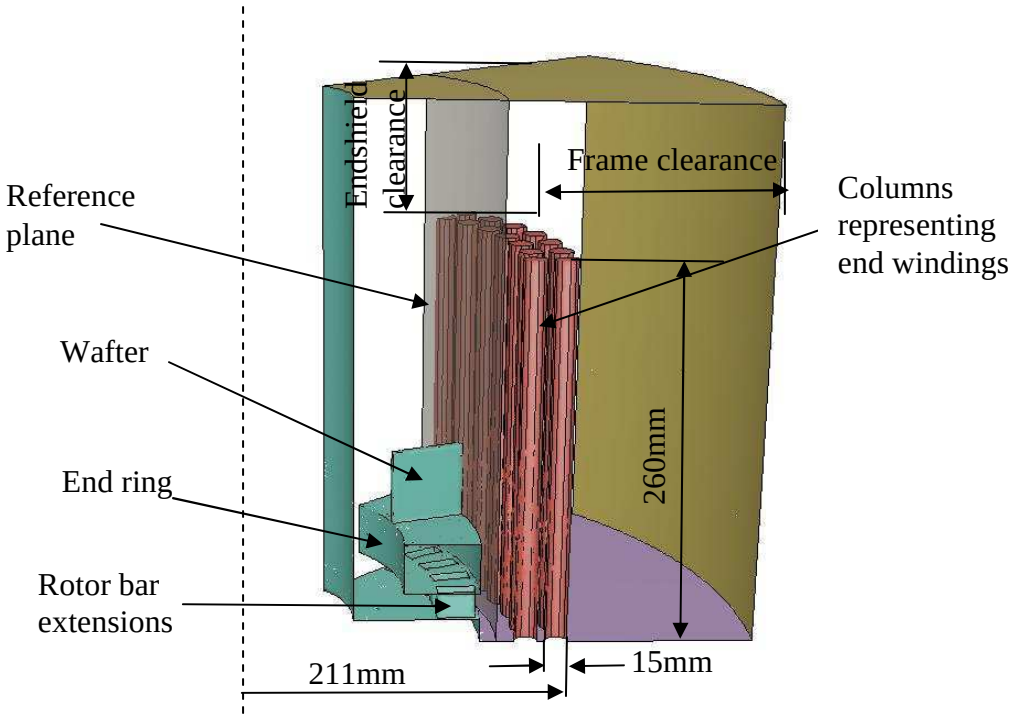

Figure 6.1 - Typical CFD model of simplified end region

Although this may seem to be an oversimplification, it gives an insight into the general understanding of the fluid and heat flow fields in the end region of TEFC induction motors.

The openness, defined as the ratio of the gap between columns to the pitch between column centers (Figure 6.2), was fixed to fifty percent for all models. This is a typical value used in induction motors and is imposed by the stator core magnetic design limitations (generally known as magnetic saturation, a point where the core cannot absorb a stronger magnetic field).

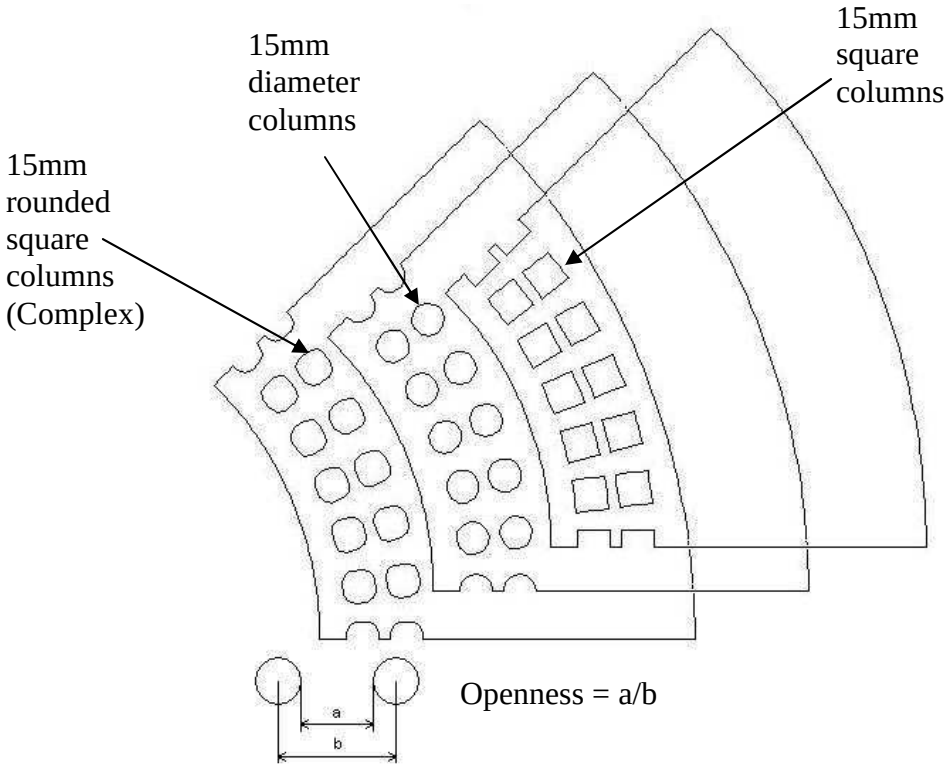

Figure 6.2 - Cross-section of columns and definition of openness

In order to simulate the end winding realistically, the cross-section of the columns which best represented the end windings had to be assessed. This was based on the velocity magnitude profile along a reference plane midway between the wafters and the columns representing the end windings as shown in Figure 6.1. Figure 6.2 shows the cross-sections that were assessed while Figure 6.3 shows the velocity magnitude profiles along the reference plane. Clearly the square cross-section did not represent the end windings well since the flow was contained within the end winding space (hardly any through flow). However both the circular and the rounded square cross-sections (referred to as complex) were quite good representations (some through flow was evident since the velocity magnitude decays rapidly through the columns). Finally it was decided to choose the complex

columns for the rest of the analysis since these best represented the actual end windings cross-sections.

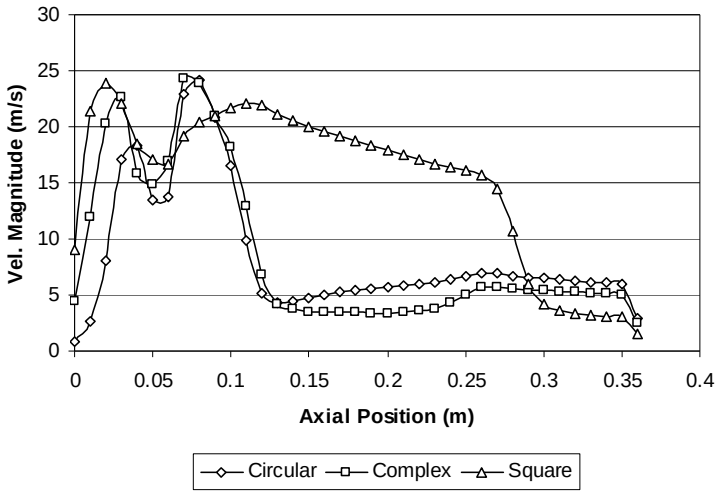

Figure 6.3 - Velocity magnitude profiles along reference plane

6.1 Frame Clearance

Frame clearance is defined as the radial clearance between the end windings and the frame as illustrated in Figure 6.1. The results show that for small endshield clearances (of the order of 25mm), increasing the frame clearance reduces the heat transfer. However for large endshield clearances (of the order of 100mm), the effect is exactly the opposite, i.e. increasing the frame clearance increases the heat transfer. This is shown graphically in Figure 6.4 where a surface plot is presented showing how heat flow varies with changes in frame clearance and endshield clearance. This shows that best heat transfer is present when the endshield clearance and the frame clearance are of the same order of magnitude.

The effect of the frame clearance was further investigated. Since in high Reynolds number forced convection, the heat transfer coefficient is independent of the

temperatures, and is highly dependent on the fluid flow field, the velocity magnitudes on a plane 5mm away from the end windings and the frame were analysed. The results showed that frame clearance did not affect the velocity magnitudes near the inner surfaces of the end windings (Figure 6.5).

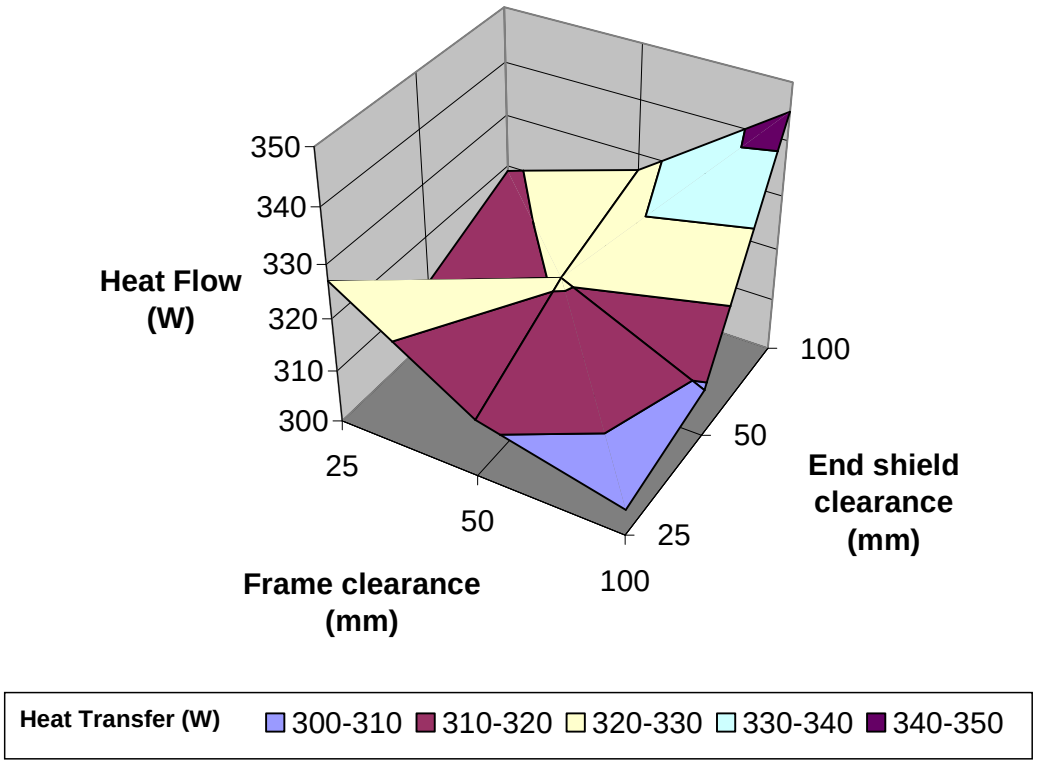

Figure 6.4 - Heat tranfer surface graph

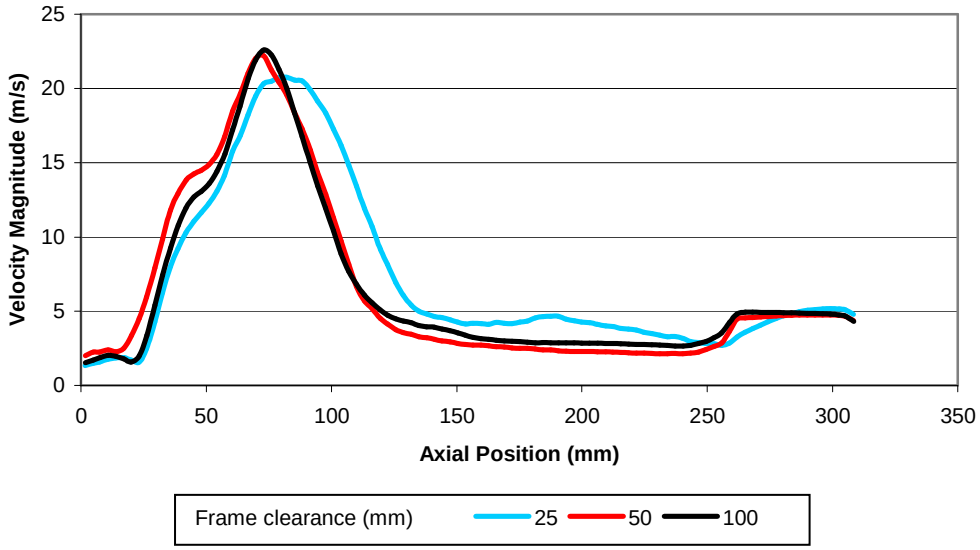

Figure 6.5 - Typical velocity magnitude in a plane 5mm away from the innermost column surfaces

A significant decrease in the velocity magnitudes in the vicinity of the outer end windings surfaces was observed as the frame clearance increased. When the frame clearance was further increased, its effect on the velocity magnitudes in the vicinity of the outer end winding surfaces was negligible. This is illustrated graphically in Figure 6.6.

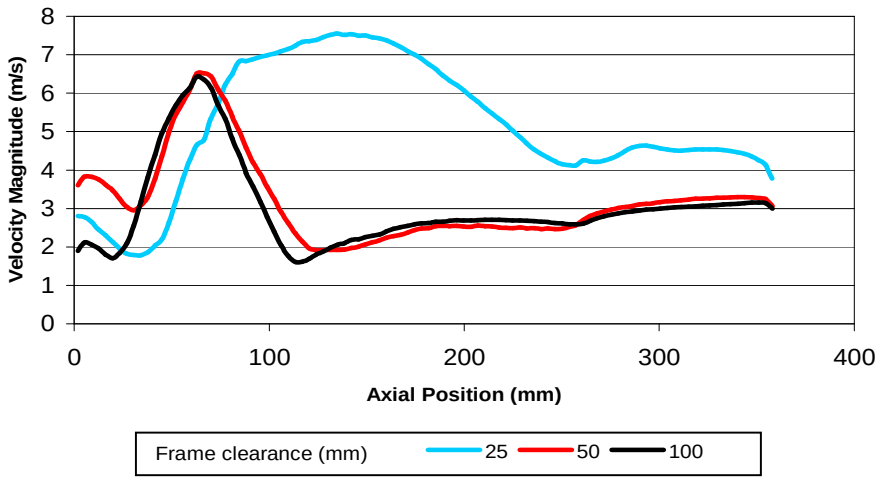

Figure 6.6 - Typical velocity magnitudes on a plane 5mm away from the outermost column surfaces

In the vicinity of the frame, the velocity magnitudes decreased with increasing frame clearance as illustrated in Figure 6.7. This gave rise to a decrease in the frame heat transfer coefficient. This does not necessarily mean that there is a corresponding decrease in the heat transfer. In fact the thermal resistance on the frame surface sometimes experience a decrease due to the increase in the surface area by increasing the radial clearance, thus increasing the heat transfer. This will be explained further in the general comments at the end of this chapter.

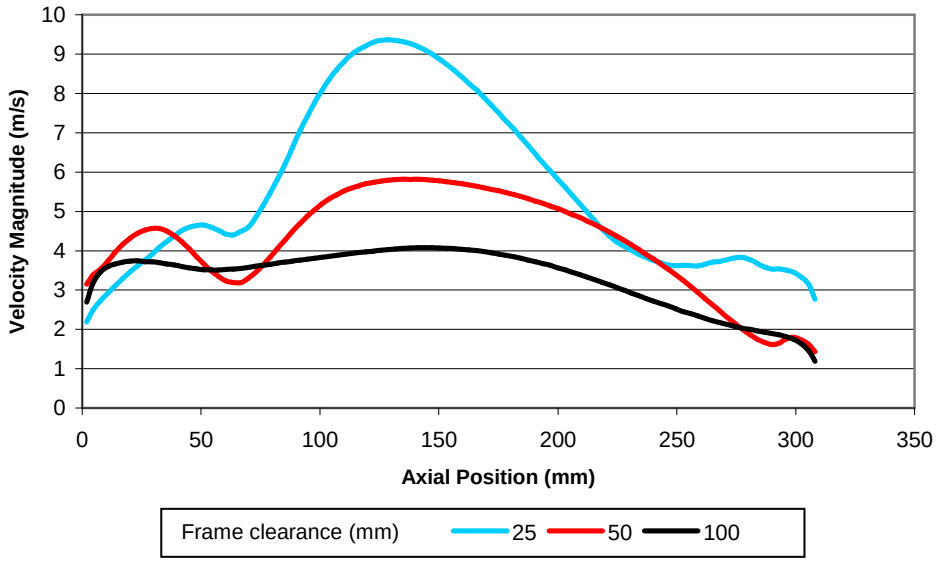

Figure 6.7 - Typical velocity magnitudes on a plane 5mm away from the frame surface

This demonstrates, however, that the frame heat transfer characteristics are not being utilised to their maximum capability since the thermal resistance is being lowered as a result of larger surface area rather than higher heat transfer coefficient.

In the vicinity of the endshield the velocity magnitudes were more or less unaffected by changes in the radial clearance. However, as a result of the increase

in the endshield surface area with increasing radial clearance, the heat transfer also increased.

Additionally, large frame clearance gives rise to vortices behind the end windings as shown in Figure 6.8. When these vortices are large enough they help in mixing the recirculating air with the air in the vicinity of the frame thus cooling it down. This provides better cooling characteristics.

On the other hand, when these vortices are weak, the air seems to be trapped inside these vortices which generate hot spots. Consequently, this hot vortex behaves just like an air curtain in the vicinity of the end windings which deteriorates the cooling performance of the area. This is illustrated in Figure 6.8.

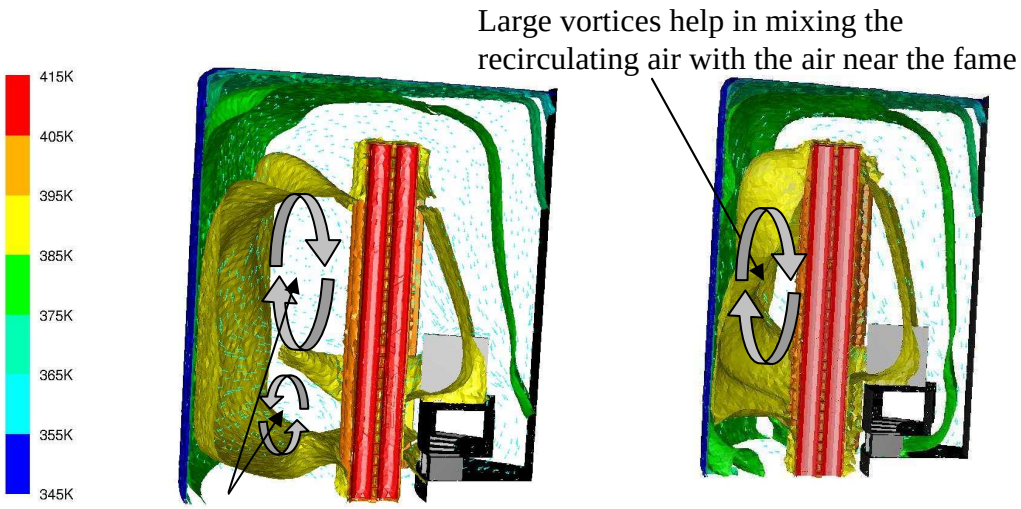

Figure 6.8 – Constant temperature surfaces showing the effect of vortices behind the columns.

Small frame clearances generally give rise to a blockage effect in front of the end windings. Thus secondary recirculating air is partially blocked from travelling through the windings. However, small frame clearances also give rise to higher

velocities behind the end windings. Therefore the frame heat transfer coefficients are higher.

6.2 Endshield clearance

Endshield clearance is defined as the axial distance between the top of the end windings and the endshield. The effect the endshield clearance has on the flow field and heat transfer in the end region of TEFC induction motors was also investigated. This was done by analysing the velocity magnitudes in the vicinity of the end windings with changes in the endshield clearance. The results show that no significant changes in velocity magnitude in the vicinity of the end windings were observed by changing the endshield clearance. This is shown in Figure 6.9.

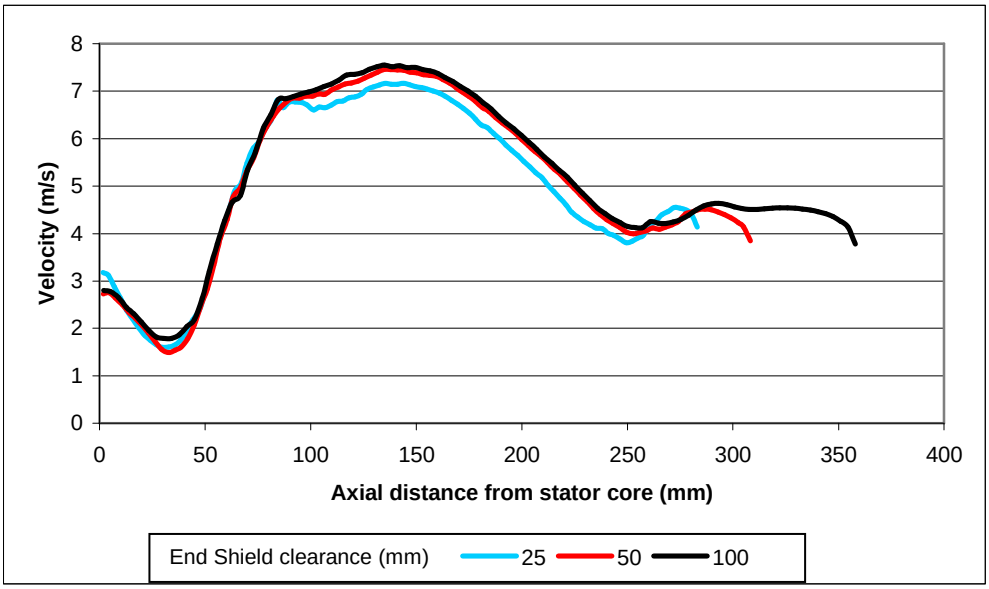

Figure 6.9 - Typical velocity magnitudes behind the columns (5mm away from the column)

Additionally the overall heat transfer coefficient on the frame decreased with increasing endshield clearance. This was attributed to the low velocity in the vicinity of the increased frame area (above the end windings height), giving rise to

a lower average velocity magnitude in the vicinity of the frame. The same argument which was applied to the previous section regarding frame surface area increase due to increased endshield clearance, holds even here. That is, the thermal resistance of the frame surface did not always decrease accordingly.

A general feature which was observed was that when the endshield clearance is much larger than the frame clearance, a strong swirl develops in the space above the windings in a horizontal plane as shown in Figure 6.10.

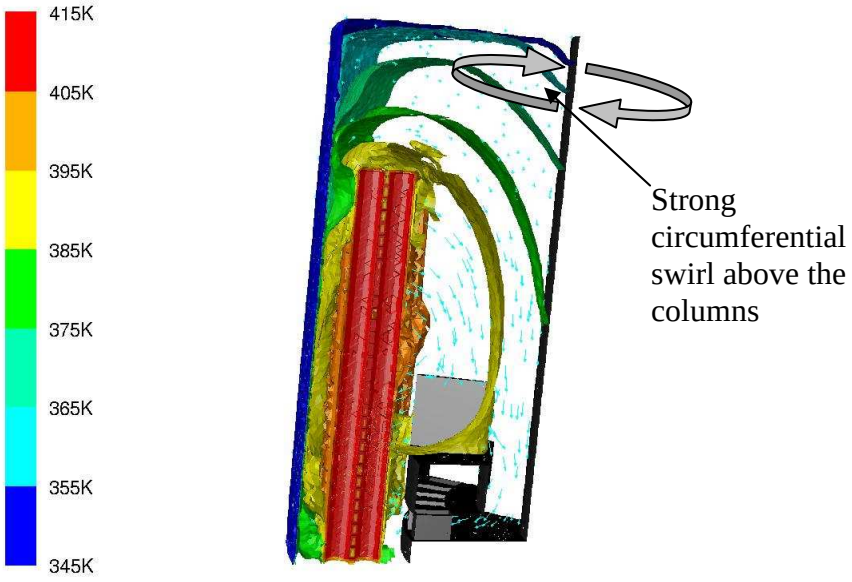

Figure 6.10 - Strong swirl in the space above the columns

6.3 Oblique wafters

Investigations on models with oblique plane wafters (refer to Figure 6.11) were also conducted. The angle of incident of the blade (28 degrees) was estimated using standard techniques in blade design commonly referred to as velocity vector diagrams and is only valid for this specific case. Oblique wafters were chosen due

to their improved aerodynamic efficiency. Oblique wafters however are only efficient at their designed rotational speed and this may be a problem in variable speed applications. Nonetheless, since a lot of these motors drive unidirectional pumps this disadvantage is not an issue in such unidirectional applications provided that the right motor is chosen for the right pump. The results indicate that the same heat transfer could be attained at seventy percent of fan power (compared to orthogonal wafters). When the length of the wafters was doubled, the heat transfer decreased.

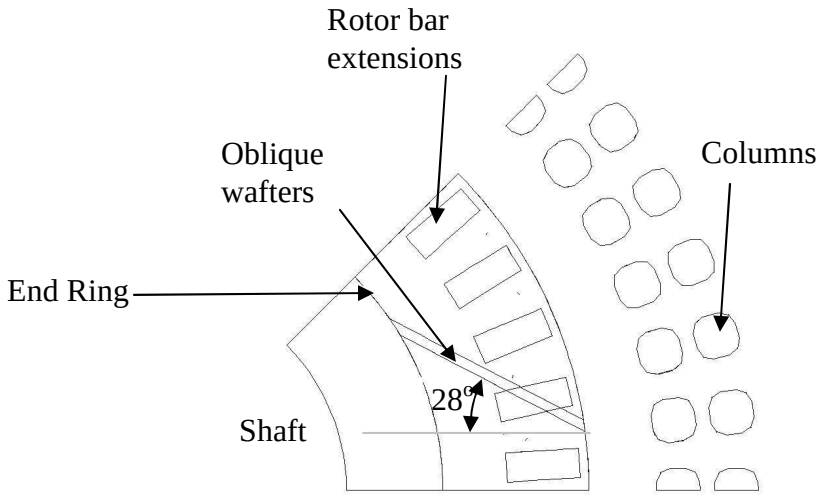

Figure 6.11 - Diagram showing oblique wafters

Detailed analysis of the situation revealed that there was a slight increase in the heat transfer coefficient of the end windings due to larger surface area affected by the jet emerging from the longer wafters. However, there is also a slight decrease of the heat transfer coefficient on the frame due to a decrease in the recirculation past the end windings. This resulted in a slight increase in the total thermal resistance. This was also exhibited by having a higher bulk temperature, indicating that the heat transfer to the frame was limiting the overall heat transfer. Figure

6.12 (c) & (d) illustrates this graphically by plotting temperature contours and velocity vectors in the plane of the wafters.

6.4 Shrouded wafters

A model having shrouded wafters (refer to Figure 6.12 (b)) was also investigated. In this model there was a nine percent decrease in heat transfer. However there was also a thirty five percent decrease in windage losses. This modification lead to a drop in the overall heat transfer coefficients of both the end windings and the frame due to the weakening of the jet emerging from the wafters. This was due to the shroud limiting the recirculation of the air.

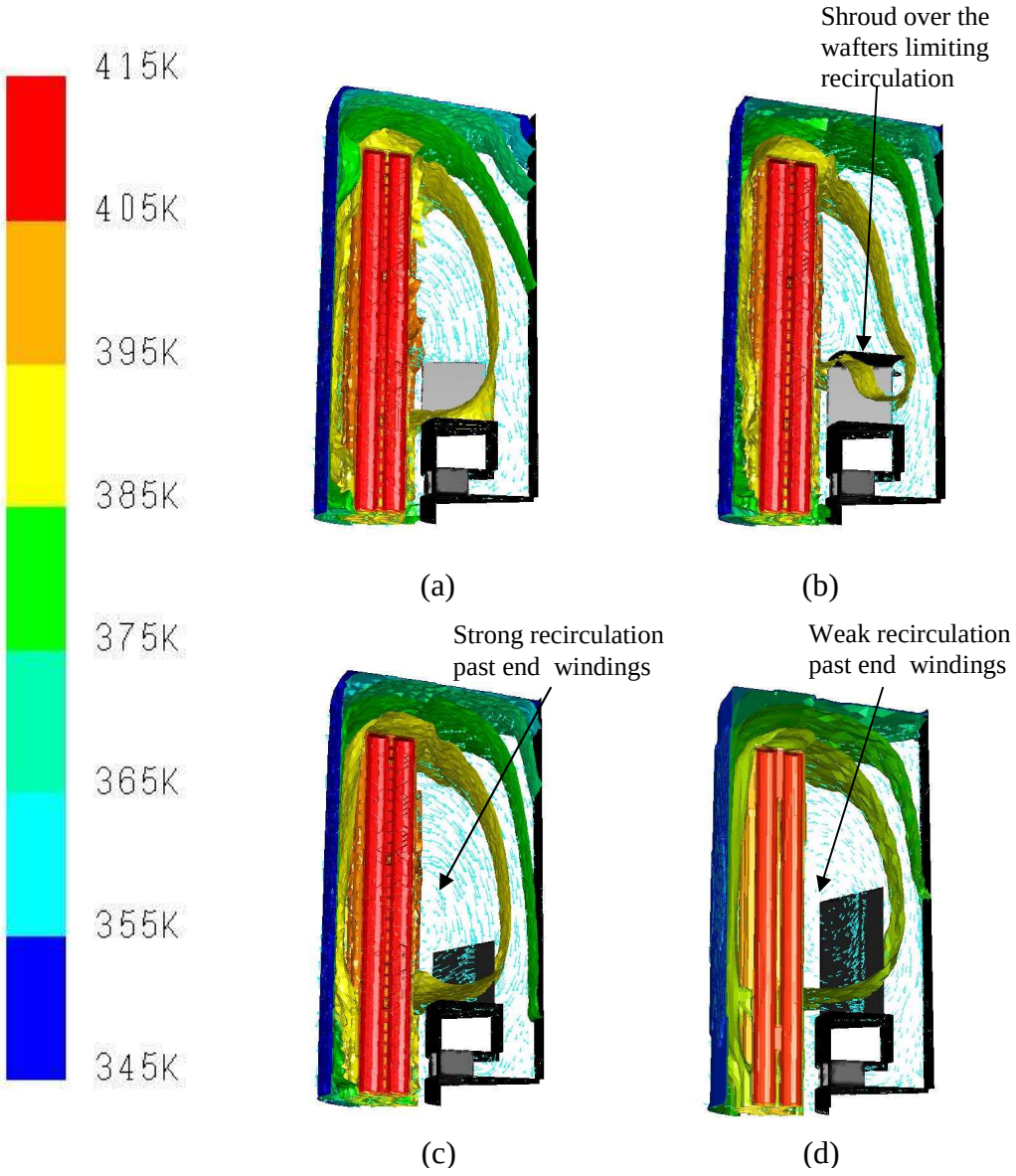

Figure 6.12 - Plots of velocity vectors in the wafter plane showing temperature contours for (a) 50 mm orthogonal (b) 50 mm shrouded (c) 50 mm oblique and (d) 100 mm oblique wafters

6.5 End winding inclination in the radial plane

The inclination of the windings in the radial plane was also investigated by varying the angle the windings make with the rotor axis. The capacity of heat transfer was reduced considerably (in the order of fifteen percent for every 5 degrees inclination). This was due to the recirculated air being hotter due to the

fact that the heat transfer coefficient on the frame side decreased considerably. Additionally the heat transfer coefficient of the end windings experienced a slight decrease. Detailed analysis of the flow fields showed that as the inclination was increased the flow became more localised in the vicinity of the wafters and end windings (Figure 6.13). This contributed to the lack of circulation of the enclosed air.

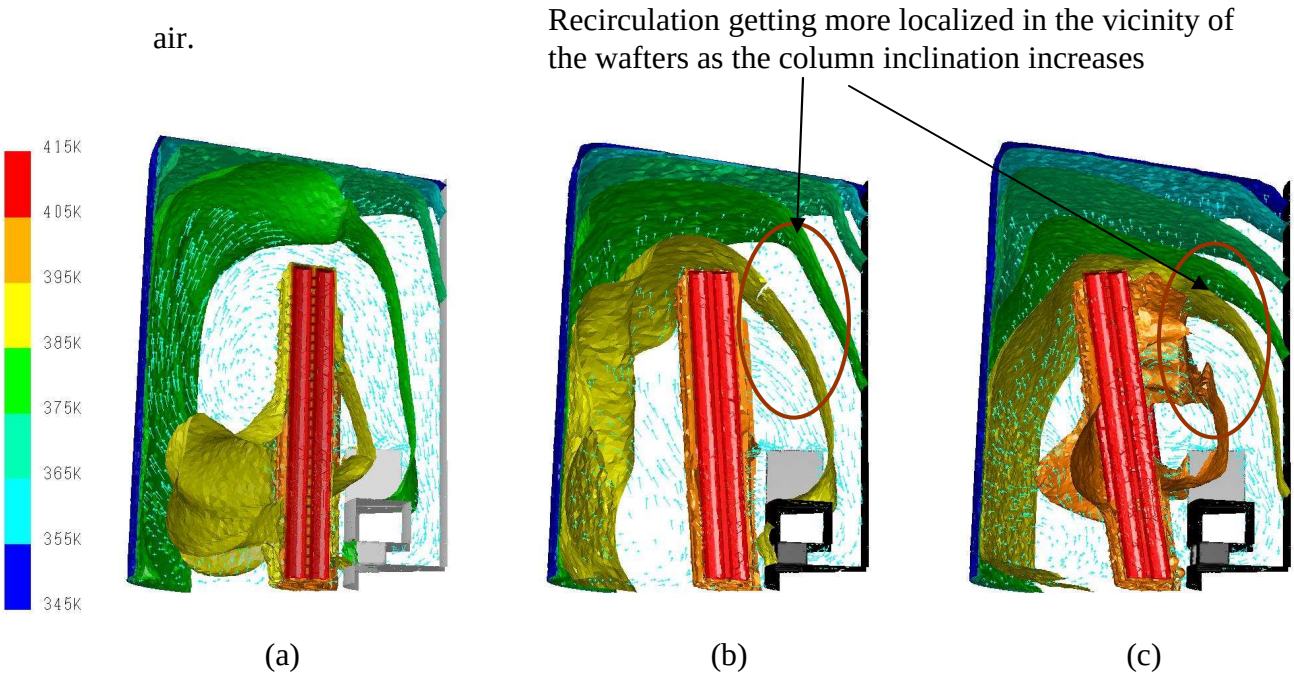

Figure 6.13 - Plots of velocity vectors in the wafter plane showing temperature contours for (a) 0 degrees (b) 5 degrees and (c) 10 degrees end winding inclination in the radial plane

6.6 Heat Flow in the End Region

From this study it has been observed that designing the end region of a TEFC induction motor is not an easy task since a lot of parameters affect the flow fields. Figure 6.14 shows a simple thermal resistance network representing the end region of a TEFC induction motor.

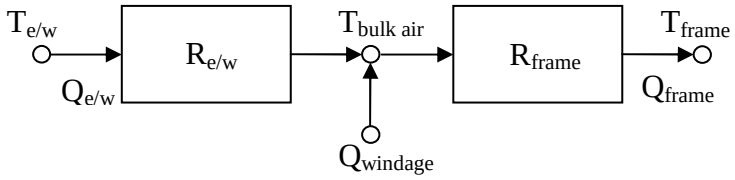

Figure 6.14 – Simple thermal resistance network of end region

Applying Fourier's Law of Conduction between each node gives;

$$Q_{e/w} = \frac{T_{e/w} - T_{bulk\ air}}{R_{e/w}} \qquad (6.1)$$

$$Q_{frame} = \frac{T_{bulk\ air} - T_{frame}}{R_{frame}} \qquad (6.2)$$

If the heat input due to windage loss is neglected then

$$Q_{end\ winding} = Q_{frame} \qquad (6.3)$$

and therefore

$$Q = \frac{T_{e/w} - T_{frame}}{R_{e/w} + R_{frame}} \qquad (6.4)$$

and

$$T_{bulk\ air} = \frac{T_{e/w}\dfrac{R_{frame}}{R_{e/w}} + T_{frame}}{\dfrac{R_{frame}}{R_{e/w}} + 1} \qquad (6.5)$$

Equation 6.4 implies that in order to maximise the heat transfer, the sum of the thermal resistances of the end windings and the frame (that is the total thermal

resistance) has to be minimized. Also, if the frame and end winding temperatures are fixed, then Equation 6.5 implies that the bulk air temperature depends only on the ratio $\frac{R_{frame}}{R_{e/w}}$.

When designing the end region of TEFC motors, the aim is to limit the end winding temperature and at the same time maximise the heat transfer. Consequently both the bulk air temperature and the heat flow rate are crucial to the design.

If equations 6.1 and 6.2 are plotted on a Q vs $T_{bulk\ air}$ graph, the point of intersection between the two lines would satisfy equation 6.3. This is illustrated in Figure 6.15 together with the aim being targeted (that is to increase the heat transfer and limit the temperature).

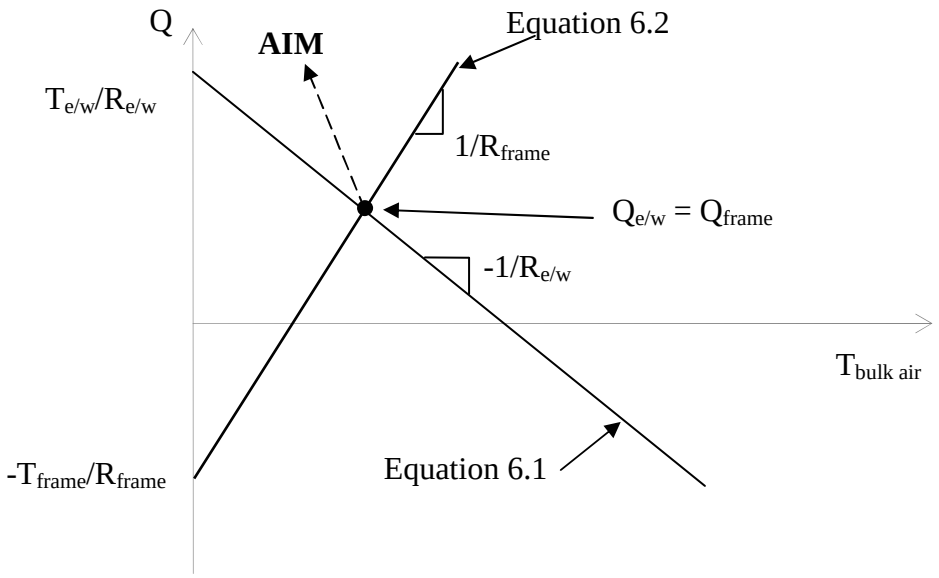

Figure 6.15 – Graph showing aim targeted by the heat transfer enhancement exercise

Using the thermal network shown above and keeping the end winding and frame temperatures fixed, a simple analysis may be performed as follows. If the heat transfer at the end winding is enhanced without a corresponding improvement in the heat transfer at the frame surface, the heat flow is increased since the total resistance to heat flow is decreased. At the same time the air bulk temperature is increased which decreases its cooling capacity. Therefore only a slight improvement results since the two phenomena are in conflict. This is shown in Figure 6.16.

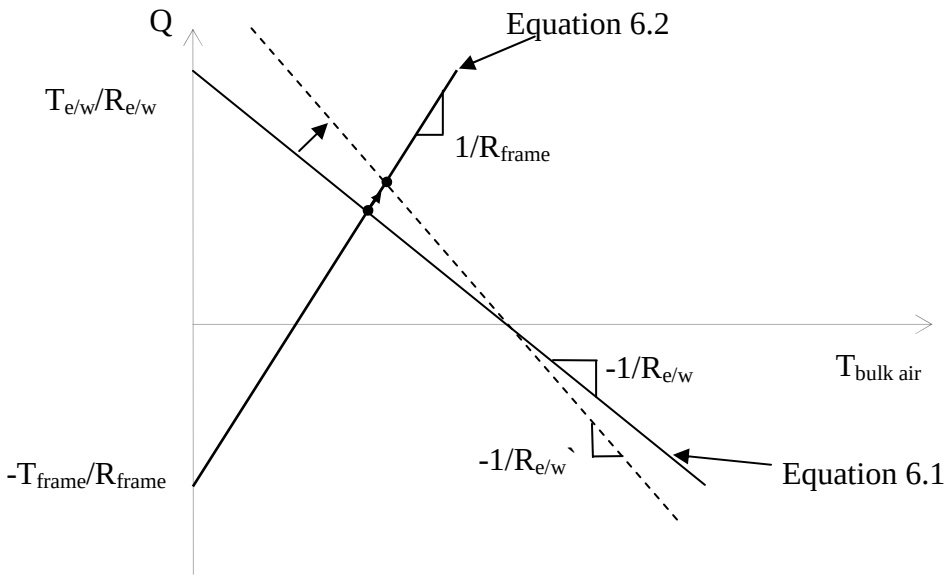

Figure 6.16 – Effect of enhancing only end winding heat transfer coefficient

On the other hand, if the heat transfer at the frame internal surface is enhanced without a corresponding improvement in the end winding heat transfer coefficient, the heat flow will increase once again. However, this time the bulk temperature is likely to decrease, thus improving its cooling capacity. Therefore, since the

changes complement each other a substantial increase in heat transfer is likely to occur. This is illustrated in Figure 6.17.

The main idea is that the total thermal resistance between the end windings and the frame has to be minimised. The relative magnitude of the thermal resistances of the end windings and frame dictates which of the two thermal resistances needs more attention.

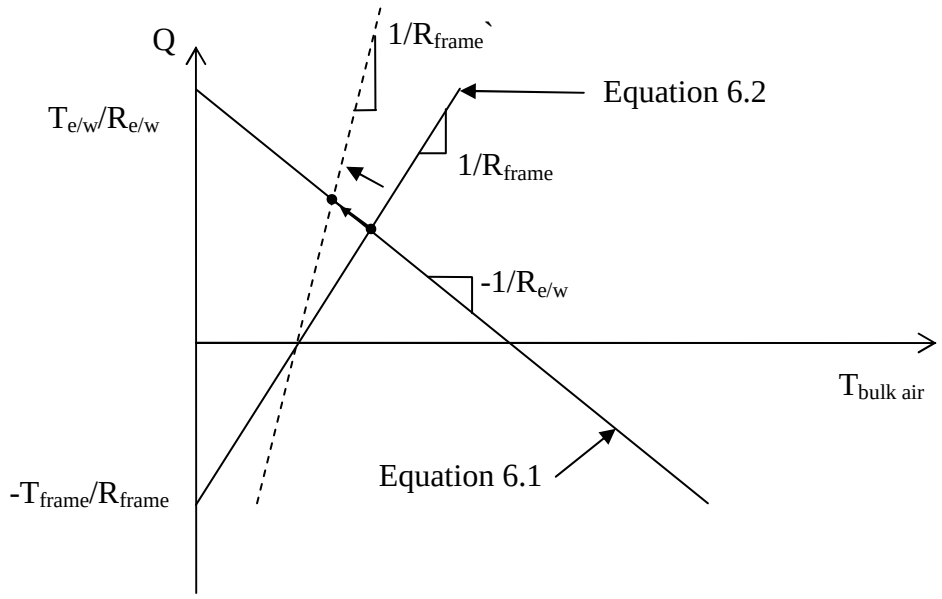

Figure 6.17 – Effect of enhancing only frame heat transfer coefficient

It is necessary to consider the end region as a whole, rather than trying to only improve the heat transfer at the end winding or at the frame. It is the total thermal resistance between the end winding and the frame which needs to be minimised for optimum heat transfer in the end region. If the heat transfer at the end winding is enhanced, neglecting the effect this will have on the frame, the overall effect can be negative. For example, if the end region is modified so as to increase the overall heat transfer coefficient at the end winding, this change may reduce the heat

transfer at the frame. This might lead to a decrease in the heat transfer from the end windings to the frame and is therefore accompanied by an increase in the enclosed air temperature, which means that the end windings may increase in temperature.

The frame of TEFC is therefore very critical and should be given appropriate attention. There are various ways in which the heat transfer in the end region across the frame may be improved. One method is to introduce extended surfaces (fins) on the inside of the frame or even cooling channels. The rest of this study however will not investigate such enhancements. It will concentrate on how the flow field may be altered to increase the heat transfer in the end region without altering the frame. This applies only to TEFC designs since in through ventilated machines the frame in the end region is not critical because the air carrying the heat away from the motor parts is exhausted to the ambient and heat transfer on the frame is not an important heat flow.

The thermal network illustrated in Figure 6.14 is only a simplified model. Usually there are other heat flow paths such as the flow of heat through the stator. However when the end windings are running hot, the heat flows from the end windings to the stator via the copper wires and thus serves as an additional path for the heat to escape. When the stator is running hot, the opposite happens and heat flows from the stator to the end winding. In the latter scenario it is the heat transfer across the stator which needs to be enhanced and not the end winding and as such is out of the scope of this work.

6.7 Conclusions and summary of results

Extensive modelling has been performed on simplified models representing the end region of a large induction motor. Table 6-1 summarizes the results from these investigations. It highlights the fact that generally the thermal resistance of the frame is much higher than the thermal resistance of the end windings.

Table 6-1 - Summary of Results

Wafter type	Wafter length (mm)	End Winding type	Frame Clearance (mm)	Endshield Clearance (mm)	Q (W)	End Windings htc (W/m2K)	Frame htc (W/m2K)	End Windings Thermal Resistance (K/W)	Frame and End Shield Thermal Resistance (K/W)
Orthogonal	50	Straight	24	25	327	83	52	0.076	0.265
Orthogonal	50	Straight	74	25	311	79	38	0.080	0.278
Orthogonal	50	Straight	124	25	305	81	30	0.077	0.286
Orthogonal	50	Straight	24	50	311	78	47	0.080	0.276
Orthogonal	50	Straight	74	50	321	76	38	0.083	0.266
Orthogonal	50	Straight	124	50	309	75	29	0.084	0.276
Orthogonal	50	Straight	24	100	319	70	45	0.090	0.260
Orthogonal	50	Straight	74	100	327	73	35	0.087	0.258
Orthogonal	50	Straight	124	100	345	77	30	0.082	0.244
Orthogonal	50	Inclined 5^o	124	100	257	68	22	0.094	0.330
Orthogonal	50	Inclined 10^o	124	100	221	64	20	0.099	0.372
Oblique	50	Straight	24	50	310	78	45	0.080	0.286
Oblique	100	Straight	24	50	300	83	43	0.076	0.299
Shrouded	50	Straight	24	50	284	68	42	0.092	0.307

The first 9 rows of the table relate to the analysis performed on frame and endshield clearances (refer to Sections 6.1 and 6.2). It was found that the highest heat transfer (equivalent to lowest overall thermal resistance) was present when both clearances were of the same order of magnitude since this provides a good flow path for the recirculating air which passes through the end windings.

This table also highlights the main outcome from this study is that it is really the overall thermal resistance ($R_{e/w} + R_{frame}$) and the relative magnitudes of $R_{e/w}$ and R_{frame} which needs to be addressed.

Additionally this investigation concludes that the inclination between the end windings and the rotor axes must be kept as small as possible, as results have shown that for every 5 degrees of inclination, a corresponding fifteen percent reduction in heat transfer is observed when using traditional wafters.

Vortices may be trapping air in regions which may develop into hot spots. These hot spot can be identified using commercially available CFD software (refer to Figures 6.8 and 6.10).

This work has already been published in [34].

7 End region enhancements through CFD

In this chapter, the model presented in Section 3, representing a typical end region of a TEFC machine will be used to investigate the impact of a series of modifications on heat transfer performance.

As detailed in Section 6.6, in TEFC configurations, the total thermal resistance to heat from the end winding to the frame can be simplified to two thermal resistances connected in series, one between the end winding and the air surrounding them and the other between the air and the frame internal surface. In order to reduce the total thermal resistance, both of the individual resistances have to be minimized.

In through-ventilated configurations, the thermal resistance between the air and the frame internal surface is not critical. This is because the air, which absorbs the heat from the various motor parts (including the end windings), is rejected to atmosphere and thus the air entering the machine is always at ambient temperature.

This investigation was performed using only CFD modelling techniques since enough confidence had been gained through earlier work to make further experimental work unnecessary. The same solution methodology employed in the previous sections was adopted: the standard k-ε turbulence model was used; constant temperature thermal boundary conditions were employed to both the heated end winding and the frame; the steady state solver was used together with the rotating reference frame technique.

7.1 Configuration changes investigated.

The configuration changes that were analyzed are highlighted below.

7.1.1 Location of the spacers near the base of the end winding.

The location of the spacers separating each end winding from its neighbours is one of the simplest changes which may be applied to in the end region. This was chosen as the starting point of the investigations.Air flow is driven by the wafters and to some extent the rotor bar extensions. Since these spacers separating the individual end winding coils from one another are in the vicinity of the wafters and rotor bar extensions, they block the air from penetrating the end windings. Therefore it is thought that their position is critical.

7.1.2 Inclusion of deflectors.

The main recirculating secondary air flow present above the wafters (refer to Figure 7.1) is not directly contributing to the heat transfer from the end windings to the frame. Deflectors were introduced to force the fluid emerging from the wafters to fully penetrate the end windings. In doing so it was anticipated that the heat transfer at the end windings would be enhanced.

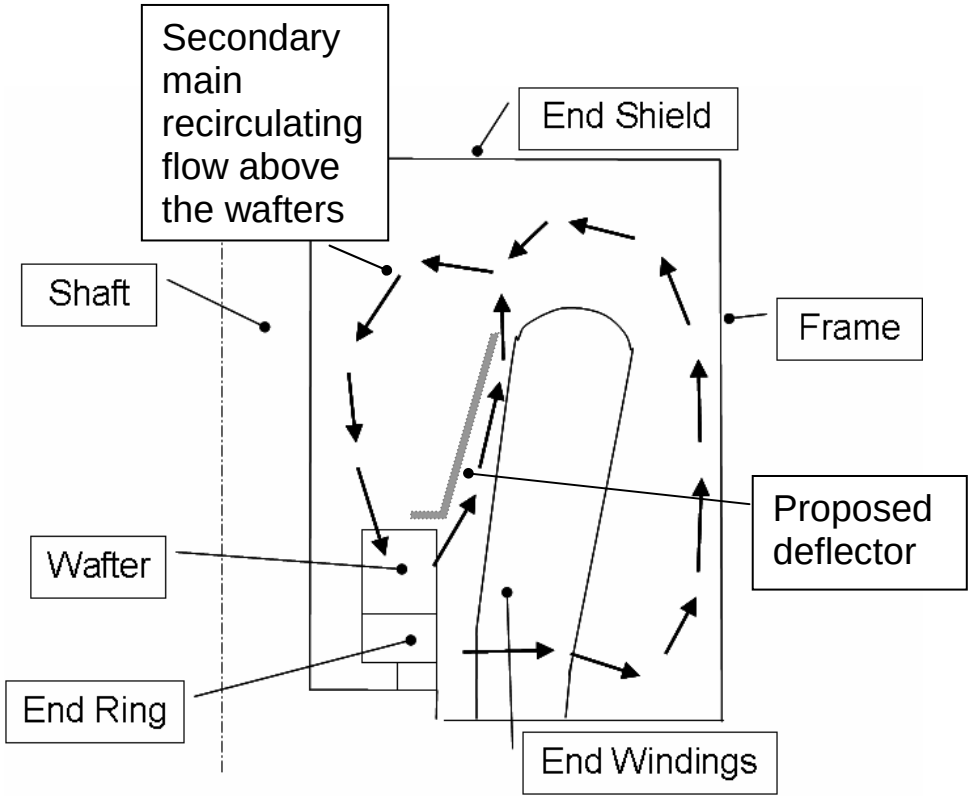

Figure 7.1 – Diagram showing proposed deflector to redirect the secondary main recirculating flow above the wafters

7.1.3 Long narrow shrouded wafters.

The investigation detailed earlier in Section 6 on simplified models of a typical end region of a TEFC configuration, showed that shrouded wafters may reduce the windage power loss by up to 33% compared to normal wafters. However since the air flow in that case was also reduced, giving rise to a reduction in heat transfer, longer narrow wafters were now used instead of the standard 50mm square wafters to compensate for the reduction in air flow. It was thought that this will lead to a substantial reduction in windage power loss but the effect this will have on the heat transfer was unknown.

7.1.4 Inclined wafters.

Due to the rotating nature of electric motors, the fluid enclosed in the end region of a TEFC motor swirls round the enclosure. Due to centrifugal forces the fluid will tend to disperse outwards creating a radial pressure gradient. Additionally, since the end windings are generally inclined slightly outwards and they offer high resistance to flow, the fluid will tend to follow the end winding profiles. Thus the fluid will tend to travel along the end windings (Figure 7.2).

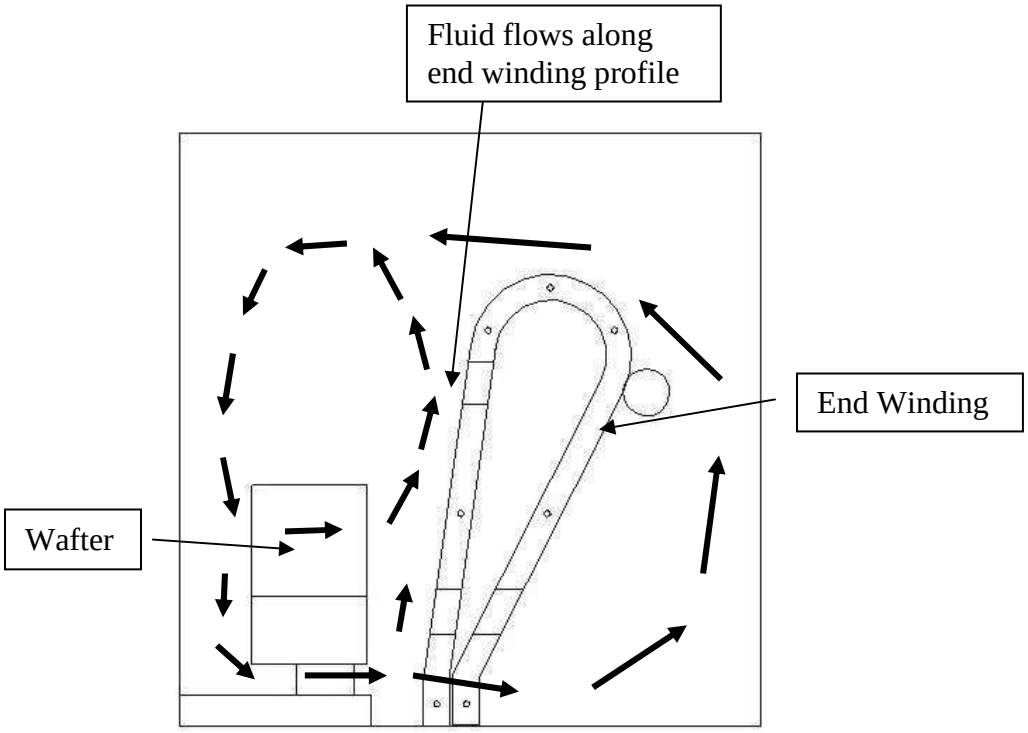

Figure 7.2 – Diagram showing how the air swirls out from the wafters and follow the end winding profiles.

In order to increase the proximity of the wafter blades to the end winding surfaces, the long narrow shrouded wafters were now inclined in order to increase their proximity to the end winding surfaces.

7.1.5 Wafters behind end windings.

The importance of the heat transfer across the frame was already highlighted previously in the study on simplified end regions. In order to improve the heat transfer characteristics on the inside frame surface, blades behind the end windings were investigated. Such blades will enhance the heat transfer on the frame side behind the end windings and also the outer end winding surfaces. The only problem this modification may have is the clearance necessary behind the end windings to connect these blades to the rotor. However, if this modification will enhance the heat transfer considerable, then it may easily be accomplished by slightly increasing the frame diameter. It is expected that the windage power loss will be increased by this change due to the larger radius of rotation of the blades. However the magnitude of the additional windage power loss is unknown.

7.1.6 Axial fan over the end windings.

The use of axial fans is also an interesting alternative which may be used in TEFC induction motors. An end region of a TEFC induction motor having an axial fan just above the end windings was modelled in order to investigate its characteristics. In order to eliminate recirculation over the blades, some stationary guides and vanes were also introduced.

Figure 7.3 shows a schematic of the configuration being investigated.

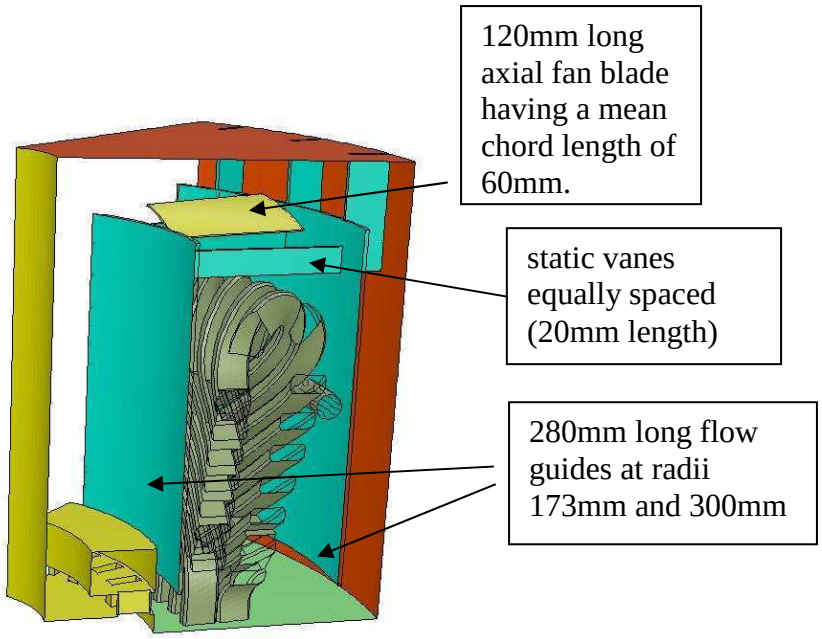

Figure 7.3 - Model including axial fan above end windings

It is anticipated that such a configuration will yield high velocities in the area of the fan blades. A strong recirculation is expected to be present with fluid emerging from the fan blades towards the base of the end windings and out of both sides of the base of the end windings. The interaction of this recirculation with the possible jet coming out of the rotor bar extensions is highly unpredictable. However it is expected that the heat transfer at both the end windings and the frame will be elevated. As will be shown later this provides interesting insight into the effect this configuration will have on windage loss, although it is anticipated that there will be high losses.

7.1.7 Rotor end design.

The rotor bar extensions act like a small centrifugal fan. This enhances both the heat transfer from the rotor bars themselves, as well as the base of the end windings. The end part of the rotor, although very difficult to implement any

modification upon, is an interesting area for investigating heat transfer enhancement and windage power loss reductions. Several configurations involving different rotor end designs were investigated in order to assess any improvement in heat transfer these changes will bring about.

7.1.8 Fan in close proximity to the end shield.

The end windings may be seen as a series of resistances to flow. The base and tips of the end windings both have a low resistance to air flow while the middle part has a very high resistance to air flow. Therefore, in order to circulate any fluid around the end windings (not necessarily penetrating the end windings) it is important to utilise the base and tip parts of the end windings as entry and exit of the fluid flow path. Also if any rotating blades or wafters are positioned in the vicinity of both the end winding surfaces and the frame surface, the heat transfer will be enhanced at both sides, thus lowering the total resistance to heat flow. In order to keep windage losses to a minimum, any rotating blades must be kept as close as possible to the shaft (minimum rotating radius).

A configuration which takes all these points into consideration is one having rotating blades attached to the shaft near the end shield. Such blades will be in close proximity to the end shield and the tips of the end windings thus enhancing the heat transfer in the area. Additionally the jet of fluid emerging from such blades will travel over the end windings and deflect at the frame surface towards the base of the end windings where it penetrates them to complete the path.

7.2 CFD Results.

CFD results for each of the configuration change described above will be presented in this section. Contour plots of heat transfer coefficients will be illustrated on end winding surfaces taken from CFD plots, thus the end winding will be divided as shown in Figure 7.4. Additionally, in order to present the contour plots of heat transfer coefficient as clearly as possible the scale is different in each of the plots and this should be taken into account when comparing figures.

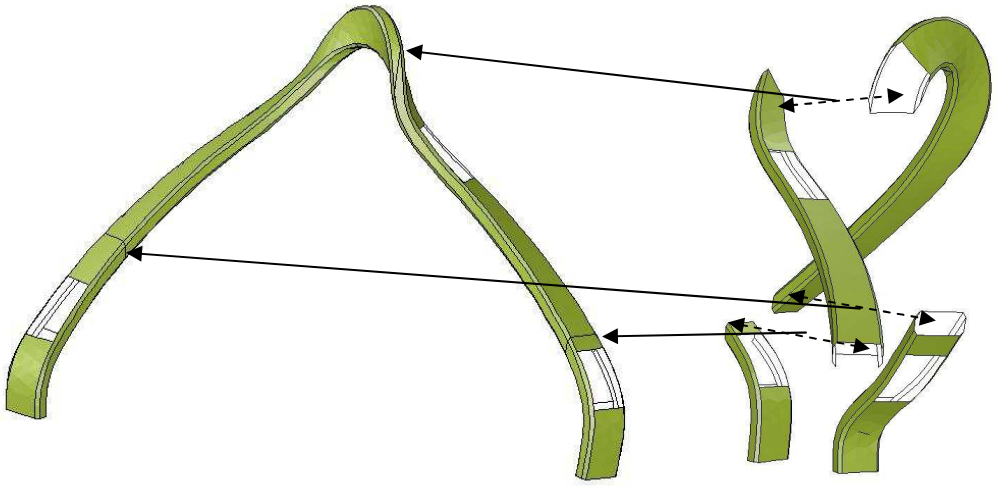

(a) (b)

Figure 7.4 – Division of end winding (a) into segments (b).

In order to model the experimental rig as close as possible, only one coil of the end windings was set to emit a heat flux. The CFD cases were made periodic with a periodicity of 45 degrees in order to decrease the model size. Therefore the CFD model actually represented an end region having 8 coils (out of 48) emitting a heat flux. The values of the thermal resistances presented in this section refer to this configuration and therefore if all end winding coils were to emit a heat flux the

thermal resistance of the end winding will decrease by a factor of 6 due to the increase in surface area.

All changes will be compared to a reference model shown in Figure 7.5 (b) since this model is the most accurate representation to the experimental rig.

7.2.1 Location of the spacers near the base of the end winding.

The experimental model being investigated has its end winding spacers which are situated opposite the end ring projecting 10mm above the end ring (refer to Figure 7.5 (b)). This part of the work investigated the position of these spacers, with respect to the end ring. In this investigation three models were created, one having the spacers exactly in line with the end ring and the other two having the spacers offset progressively by 10mm above the end ring. The cross sections of these models are shown in Figure 7.5.

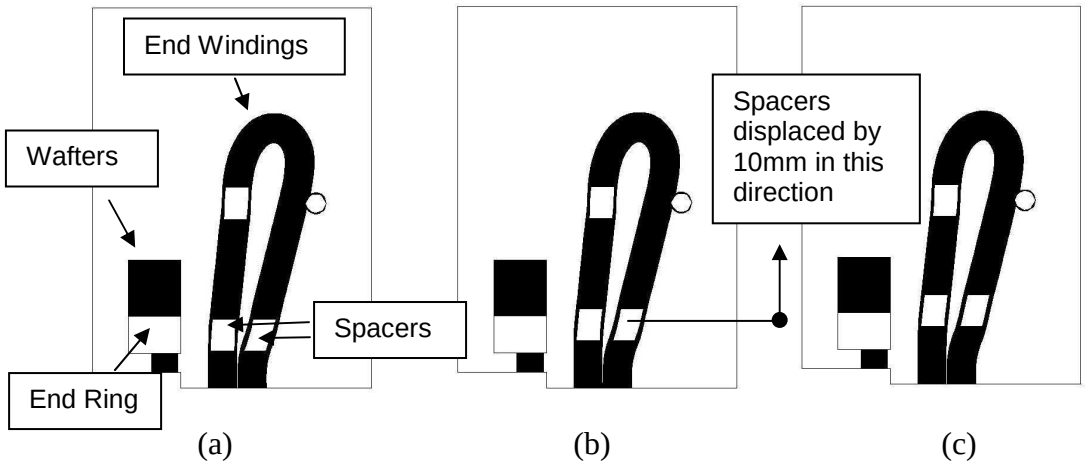

Figure 7.5 - Positions of spacers near the base of the end windings
(a) level with end ring (b) displaced away from the base of the end windings by 10mm
(c) displaced away from the base of the end windings by a further 10mm

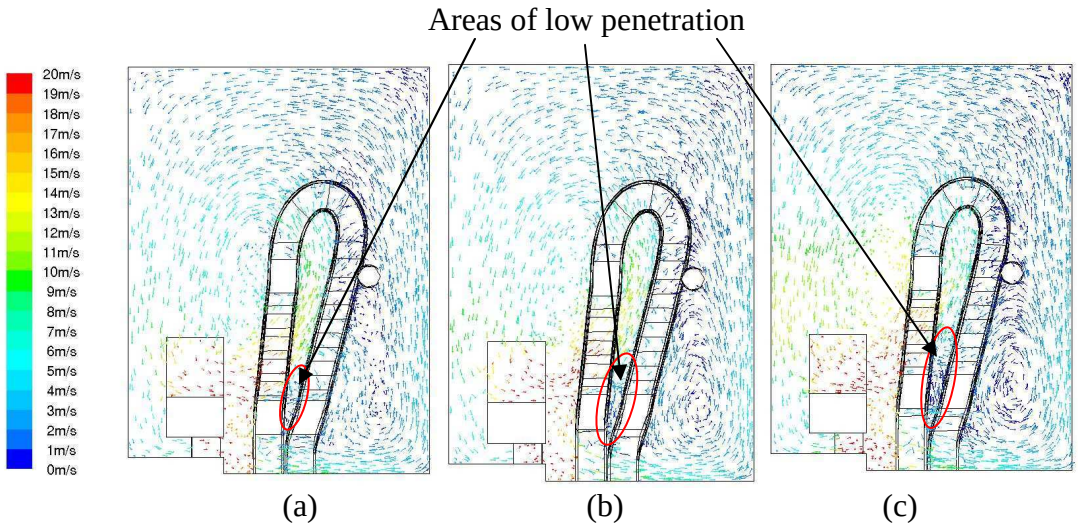

Figure 7.6 - Velocity plots for end windings having spacers near the base of the end windings (a) level with end ring (b) displaced away from the base of the end windings by 10mm (c) displaced away from the base of the end windings by a further 10mm

Figure 7.6 illustrates velocity plots projected meridionally onto one radial plane. As the spacers are moved upwards, less fluid emerging from the wafters penetrates the end windings as it is partially blocked by the spacers. As a consequence, the end winding thermal resistance experienced a progressive increase in magnitude as shown in Table 7-1 below.

Table 7-1 – Summary of results of models having different spacer locations

Model	Windage Loss (W)	Total Thermal Resistance (K/W)	Heated End Winding Thermal Resistance (K/W)	Frame Thermal Resistance (K/W)	End Winding htc (W/m^2K)	Frame htc (W/m^2K)
(a)	321	0.524	0.274	0.249	81	29.2
(b)	310	0.559	0.298	0.262	75	28.6
(c)	294	0.571	0.313	0.258	71	28.4

Since the air flow behind the end windings was little affected (weak velocities are present behind the end windings), the thermal resistance of the frame remained practically constant.

Something worth noticing is the fact that as the total thermal resistance decreases, due to the increased air flow through the end windings, the windage losses also increases accordingly. This was expected since work must be done to pump the additional air flow.

Figure 7.7 illustrates the distribution of the heat transfer coefficients on the end windings and frame for the models under investigation. The same lettering sequence as the previous Figures has been adapted. It is clear that the heat transfer is enhanced in the vicinity of the wafter base when the spacers did not interfere with the flow (red area on contour plot).

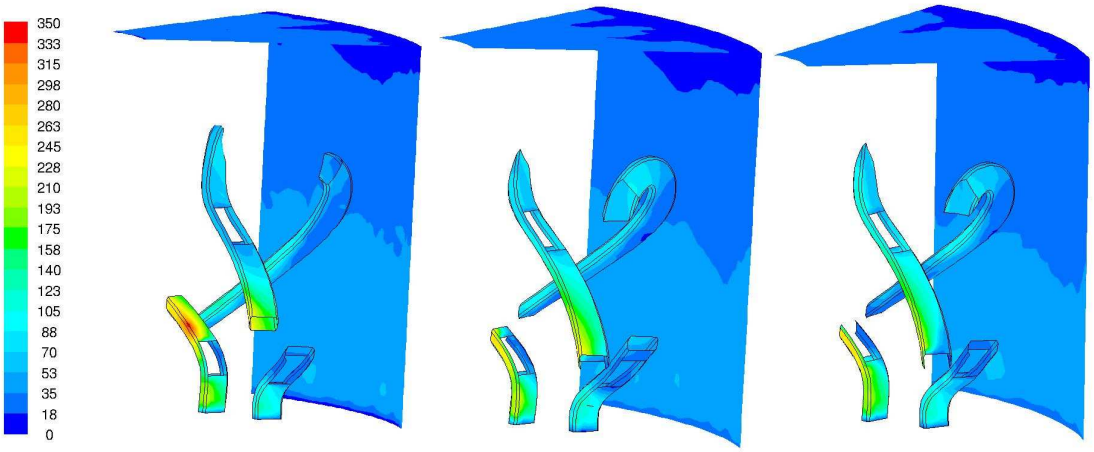

Figure 7.7 – Overall Heat Transfer Coefficients (W/m^{2}K) for end regions having spacers near the base of the end windings
(a) level with end ring (b) displaced away from the base of the end windings by 10mm
(c) displaced away from the base of the end windings by a further 10mm

7.2.2 Use of deflectors

The model being investigated here includes a 100 mm long inclined deflector over the wafters is shown in Figure 7.8 below.

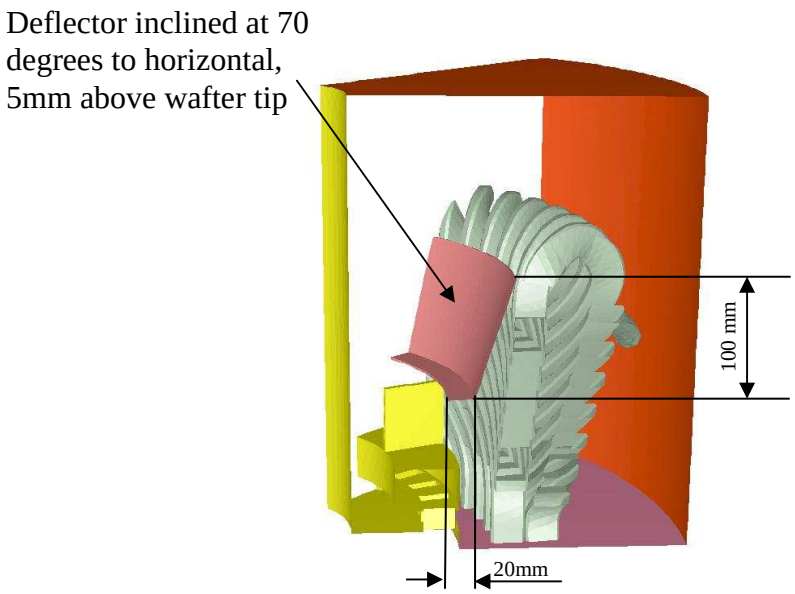

Figure 7.8 – Illustration of model employing a deflector over the wafters.

The computed flow field in Figure 7.9(a) shows that the aim to eliminate the recirculation above the wafters was achieved (compare with Figure 7.9(b)). A decrease in the amount of fluid emerging from the wafters was also experienced due to the high resistance to flow the middle part of the end windings present. This reduced recirculation gave rise to an increase in thermal resistance of both the end windings and the frame as summarized in Table 7-2. A minor reduction in windage power loss was also experienced.

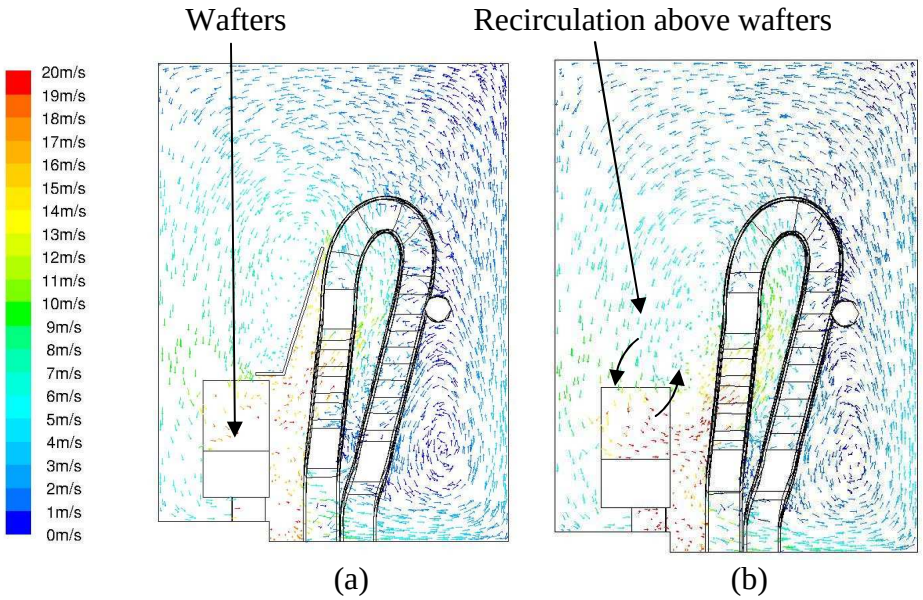

Figure 7.9 – Velocity plot in a radial plane in a model (a)with a deflector over wafters (b)without any deflectors

Table 7-2 – Comparison of results of model with deflector to base case model.

Model	Windage Loss (W)	Total Thermal Resistance (K/W)	Heated End Winding Thermal Resistance (K/W)	Frame Thermal Resistance (K/W)	End Winding htc (W/m^2K)	Frame htc (W/m^2K)
With deflector	291	0.631	0.342	0.289	65	25.3
Reference Case.	310	0.559	0.298	0.262	75	28.6

Figure 7.10 shows the distribution of the heat transfer coefficient on the end windings and frame surfaces.

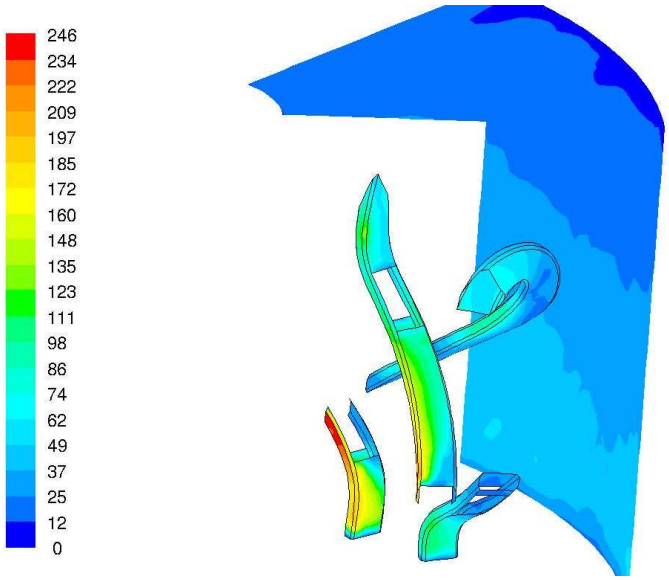

Figure 7.10 - Distribution of heat transfer coefficient (W/m^{2}K) on end windings and frame for model with a deflector.

7.2.3 Long narrow shrouded wafters

The model used for this investigation is shown in Figure 7.11 below, along with the velocity vector plot. The model utilised eight 195mm long by 10mm wide shrouded wafters. Table 7-3 summarizes the results.

Table 7-3 - Comparison of results of model with long narrow shrouded wafters to base case model.

Model	Windage Loss (W)	Total Thermal Resistance (K/W)	Heated End Winding Thermal Resistance (K/W)	Frame Thermal Resistance (K/W)	End Winding htc (W/m^{2}K)	Frame htc (W/m^{2}K)
Long narrow shrouded wafters	128	0.595	0.454	0.142	50	51.7
Reference case.	310	0.559	0.298	0.262	75	28.6

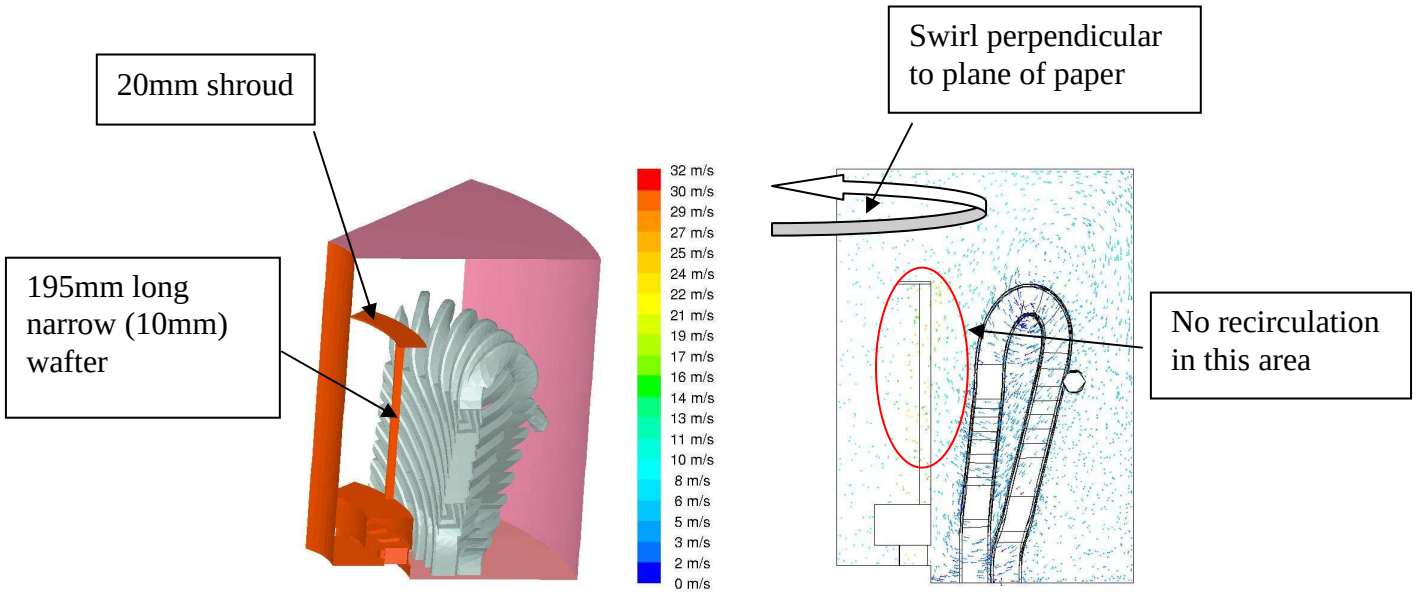

(a) (b)

Figure 7.11 - (a) model having 8 long narrow shrouded wafter (b) velocity vector plot

The aim to reduce the windage loss by reducing the mass of fluid flowing through the end windings was accomplished and the windage dropped by more than 50% (from 310W down to 128W). The velocity vector plot in Figure 7.11 (b) shows that the secondary recirculations typical in the end region of TEFC configurations were almost eliminated and the main swirl flow was the only one present. This swirl flow was also strong in the area behind the end windings.

Analysis of the heat transfer from the end windings shows that the thermal resistance of the end windings experienced an increase from 0.298K/W to 0.454K/W (52%). On the other hand the thermal resistance of the frame experienced a decrease of 46% (from 0.262K/W to 0.142K/W). This means that while the heat transfer capability on the end windings side was substantially

reduced, that on the frame's side was substantially improved. However the total thermal resistance from the end winding to the frame was increased by 6%.

Figure 7.12 shows the distribution of the heat transfer coefficient on the end windings and frame. It is clear that the heat transfer has been highly intensified on the end shield. Additionally the distribution of the heat transfer coefficient on the end windings is also more evenly distributed with peaks around the nose (furthest place from stator core). This is an additional improvement brought about by this modification.

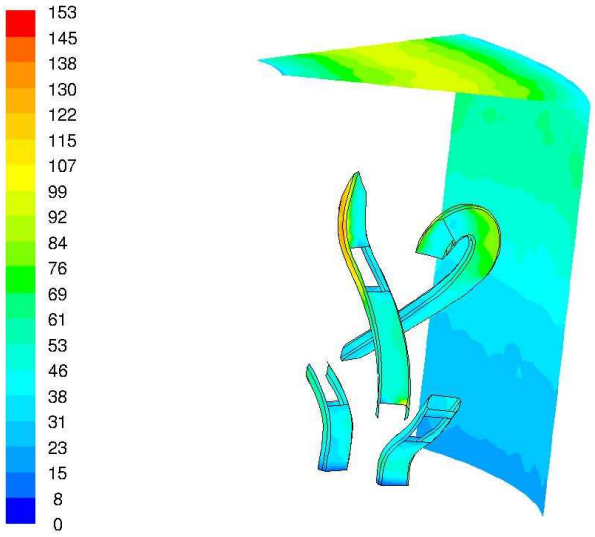

Figure 7.12 - Heat transfer coefficient distribution (W/m^2K) on end winding and frame for model having long narrow shrouded wafters.

Since the total thermal resistance was increased as a consequence of this modification, another model having 32 wafters instead of only eight was investigated. Figure 7.13 shows the velocity vector plot along with a contour plot of the heat transfer coefficients on the end windings and frame for this case. The

flow field around the end windings is stronger, especially above the end windings area, but the flow through the end windings is still very weak.

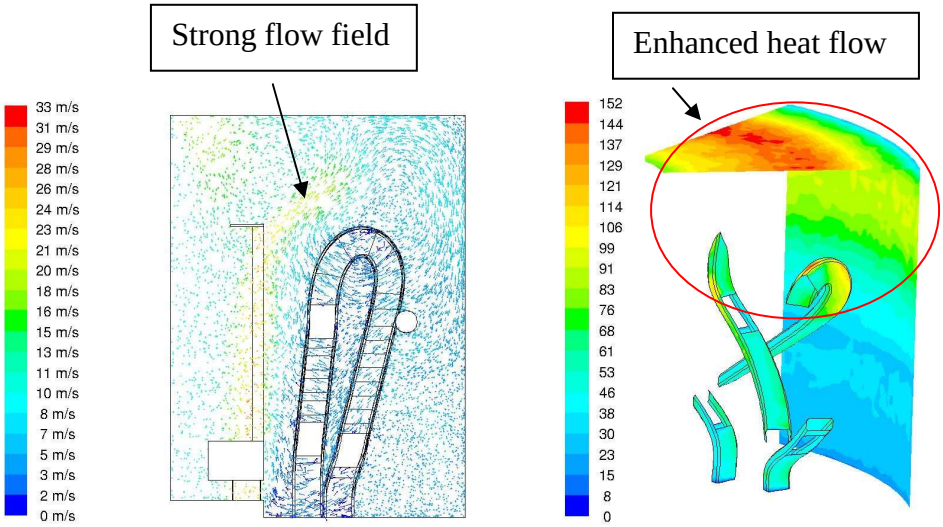

Figure 7.13 – Model using 32 long narrow shrouded wafters
(a) velocity vector plot (b) contour plot of heat transfer coefficient (W/m^{2}K)

Table 7-4 summarizes the results. The effect of increase in the number of wafters was overall positive. Both the end windings and the frame thermal resistances were improved compared to the model having 8 wafters. This was accompanied by a slight increase in windage power loss (from 128W to 159W) but is still considerable lower than the reference case (refer to Figure 7.5 (b)).

Table 7-4 - Comparison of results of models with different number of long narrow shrouded wafters to base case model.

No. of long narrow shrouded wafters	Windage Loss (W)	Total Thermal Resistance (K/W)	Heated End Winding Thermal Resistance (K/W)	Frame Thermal Resistance (K/W)	End Winding htc (W/m^2K)	Frame htc (W/m^2K)
32	159	0.505	0.398	0.107	68	56.6
8	128	0.595	0.454	0.142	50	51.7
Reference case.	310	0.559	0.298	0.262	75	28.6

The 32 wafter case was again changed by including fixed deflectors (stator vanes) just outside the wafter envelope. This is shown in Figure 7.14. The aim is to convert the circumferential kinetic energy to a pressure head. A pressure differential across the end windings will then force the fluid to penetrate the end windings.

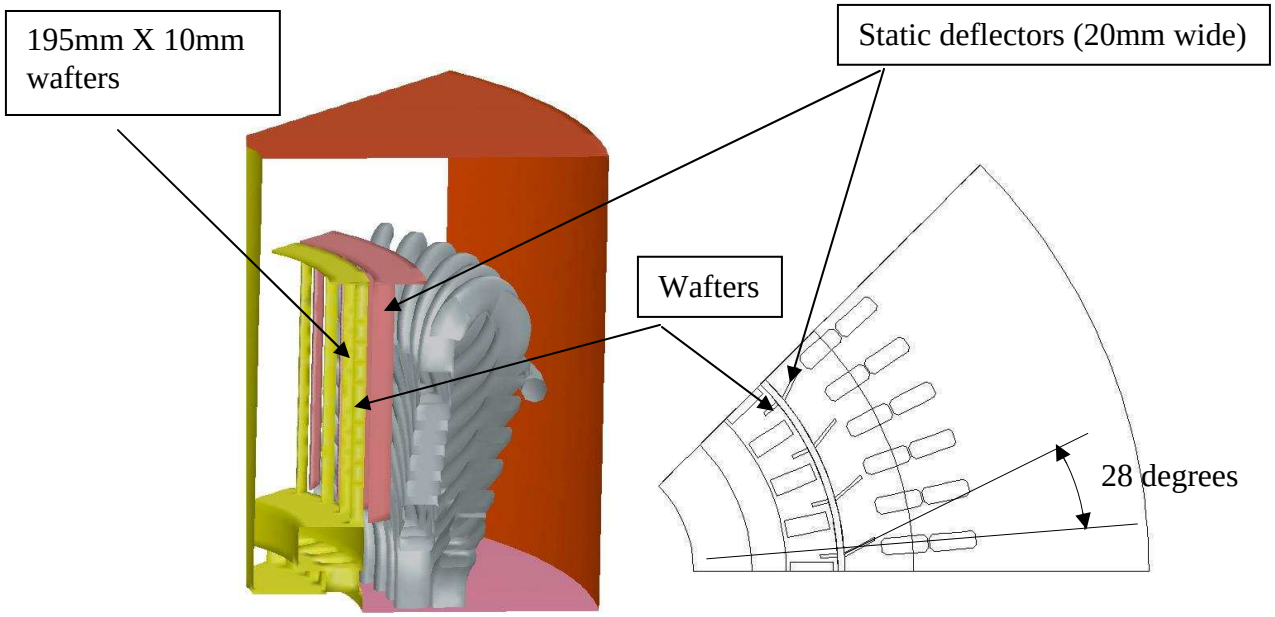

Figure 7.14 - Model including stator vanes

The objective of the stator vanes was achieved since the flow penetrated the end windings rather than swirled around them. This can be seen in the velocity vector plot in Figure 7.15 where the vectors are represented by lines indicating that they are in the plane of the paper rather than dots. The heat transfer fell substantially.

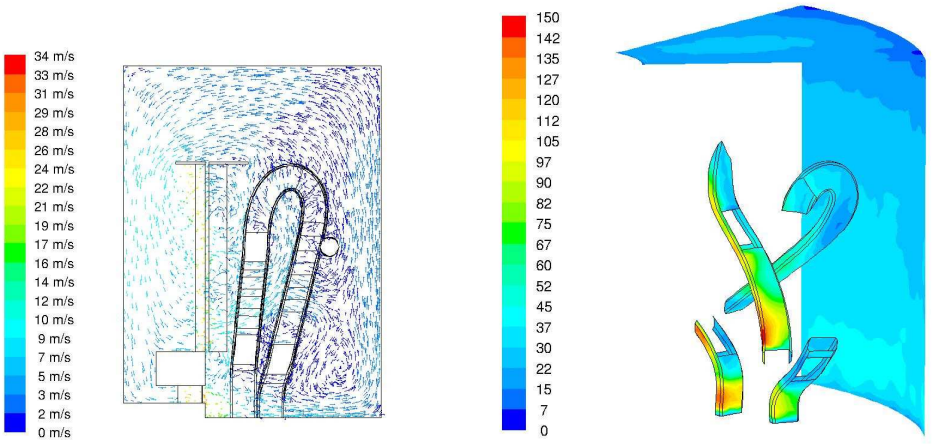

(a) (b)

Figure 7.15 - (a) velocity vector plot (b) contour plot of heat transfer coefficient (W/m^{2}K)

Referring to Table 7-5, both the thermal resistances of the end windings and frame increased substantially. Additionally the windage loss increased from 159W to 400W. The introduction of the stator vanes considerably reduced the heat transfer performance even when compared to the reference case (refer to Figure 7.5 (b)) therefore such stator vanes are of little benefit.

Table 7-5 - Comparison of results of model with stator vanes to model without stator vanes and base case model.

Model	Windage Loss (W)	Total Thermal Resistance (K/W)	Heated End Winding Thermal Resistance (K/W)	Frame Thermal Resistance (K/W)	End Winding htc (W/m^2K)	Frame htc (W/m^2K)
With stator vanes	400	0.733	0.447	0.287	50	25.5
Without stator vanes	159	0.505	0.398	0.107	68	56.6
Reference case.	310	0.559	0.298	0.262	75	28.6

7.2.4 Narrow shrouded inclined blades

Figure 7.16 (a) shows the model created for this investigation. The wafters used were 195mm long by 10mm wide and they were inclined so that their proximity to the end winding remains constant along the whole length. Seventy two inclined wafter blades were utilised.

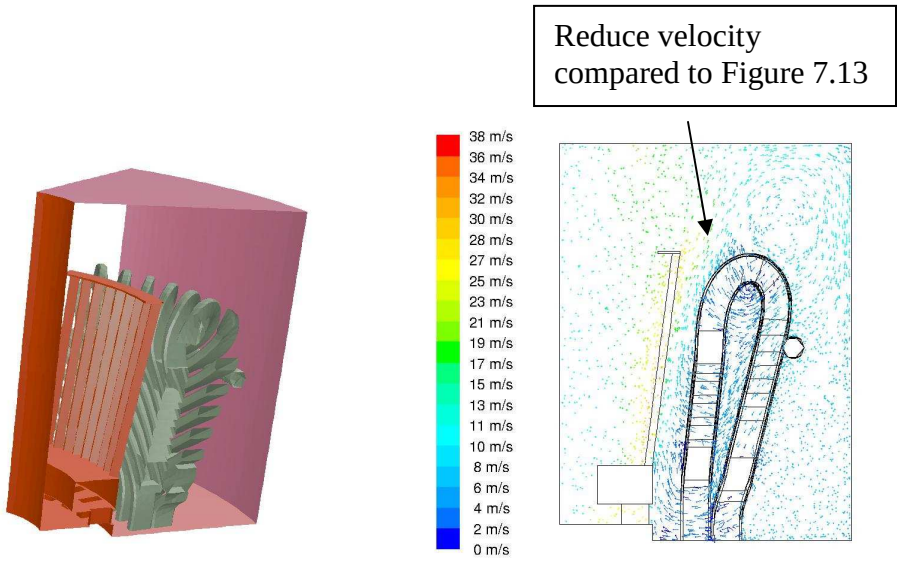

(a) (b)

Figure 7.16 - (a) model having long narrow shrouded inclined wafter (b) velocity vector plot

When comparing the results with the straight wafters (Table 7-6), it follows that the windage power loss is higher in the model using inclined wafters. The total thermal resistance from the end winding to the frame is marginally lower due to a slight decrease in the thermal resistance on the end winding side and a slight increase in the thermal resistance on the frame side. The slight decrease in the thermal resistance of the end windings is attributed to the close proximity of the wafters to the end windings. The slight increase in the thermal resistance of the frame is due to the reduced velocity magnitudes emerging out of the wafter tops above the end windings (Figure 7.16).

Table 7-6 - Comparison of results of model with long narrow shrouded inclines wafters to base case model

Model	Windage Loss (W)	Total Thermal Resistance (K/W)	Heated End Winding Thermal Resistance (K/W)	Frame Thermal Resistance (K/W)	End Winding htc (W/m^2K)	Frame htc (W/m^2K)
Inclined wafters	228	0.503	0.389	0.114	58	64.0
Straight wafters	159	0.505	0.398	0.107	68	56.6

It follows that inclined wafter blades do not contribute in enhancing the heat transfer in the end region of TEFC induction motors.

7.2.5 Blades behind end windings

Figure 7.17 (a) illustrates the model used for investigating a configuration having wafter blades behind the end windings at a radius of 300mm. For simplicity the blades behind the end windings were not connected to the rotor. However they were rotated at the same speed of the rotor.

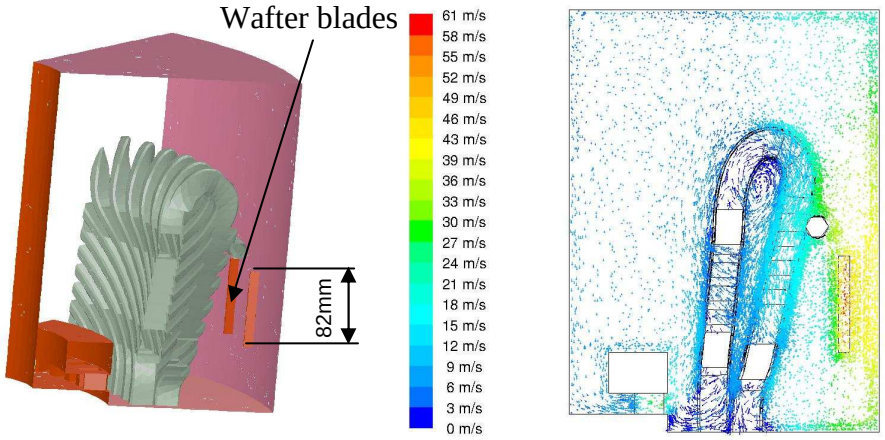

(a) (b)

Figure 7.17 - (a) model having rotating blades behind end windings (b) velocity vector plot

The fluid behind the end windings experienced a strong swirl due to the presence of the rotating blades. This contributed to enhancing the heat transfer characteristics of both the frame and the end windings in the region. Table 7-7 summarizes the results. The decrease in the thermal resistance of the end windings was 14% compared to the reference case while that on the thermal resistance of the frame was 73%. The total thermal resistance was decreased by 42% which is quite substantial. However this improvement in heat transfer was accompanied by a substantial increase in windage power loss which increased by a factor of 2.75. This is significant compared to the end winding losses and outweighs all the benefits this modification brings about.

Table 7-7 - Comparison of results of model with wafters behind end windings to base case model.

Model	Windage Loss (W)	Total Thermal Resistance (K/W)	End Winding Thermal Resistance (K/W)	Frame Thermal Resistance (K/W)	End Winding htc (W/m^2K)	Frame htc (W/m^2K)
Wafters behind end windings	853	0.326	0.255	0.071	87	104.1
Reference case.	310	0.559	0.298	0.262	75	28.6

Figure 7.18 gives a clear indication of the distribution of the heat transfer coefficients on the end windings and the frame. This shows that the heat transfer was substantially enhanced in the area behind the end windings.

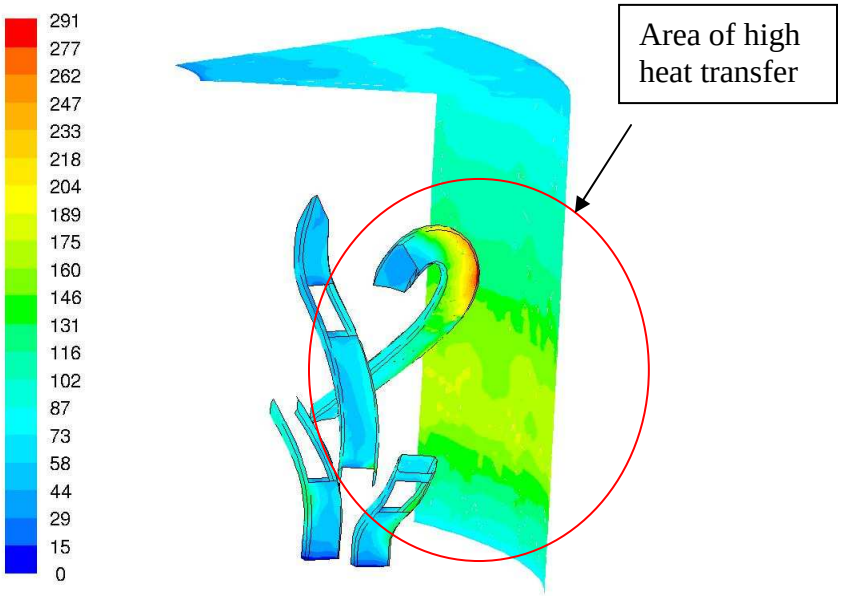

Figure 7.18 - Heat transfer coefficient distribution (W/m^2K)

The effect of reducing the number of blades from 32 to 8 was a decrease in both the heat transfer coefficients accompanied by an increase in windage loss.

7.2.6 Axial fan over end windings

Figure 7.19 shows the configuration being investigated. To keep the model as simple as possible the fan blades are not connected to the rotor in the CFD model but are being rotated at the same speed as the rotor.

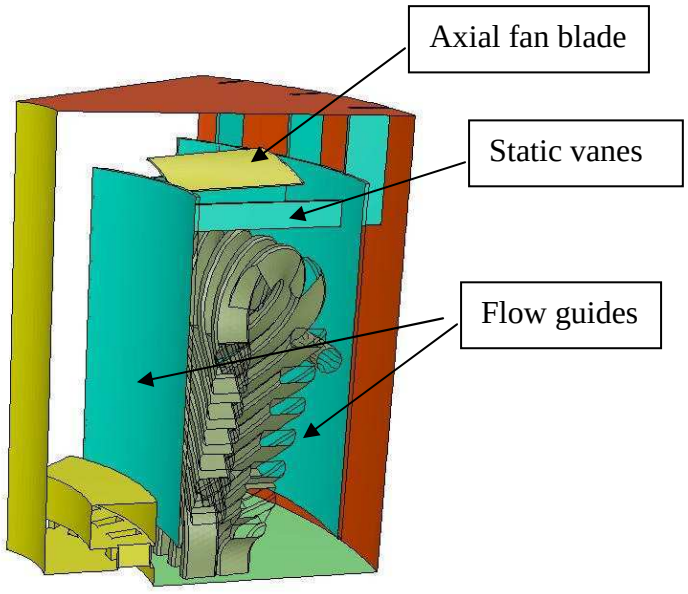

Figure 7.19 - Model including axial fan above end windings

Table 7-8 - Comparison of results of model with axial fan over the end windings to base case model.

Model	Windage Loss (W)	Total Thermal Resistance (K/W)	End Winding Thermal Resistance (K/W)	Frame Thermal Resistance (K/W)	End Winding htc (W/m^2K)	Frame htc (W/m^2K)
Axial fan	740	0.451	0.343	0.107	67	72.0
Reference case.	310	0.559	0.298	0.262	75	28.6

Figure 7.20 shows the resulting velocity vector plot and contour plot of heat transfer coefficients. The velocity vector plot shows that the fluid is flowing as anticipated, that is recirculating through the base of the end windings. High velocities (in the order of 11m/s) are present throughout the region. The total thermal resistance experienced a decrease of 19% compared to the reference case. The end winding thermal resistance increased by 15% while that of the frame decreased by 59%. Therefore the frame was much more affected by the change than was the end winding.

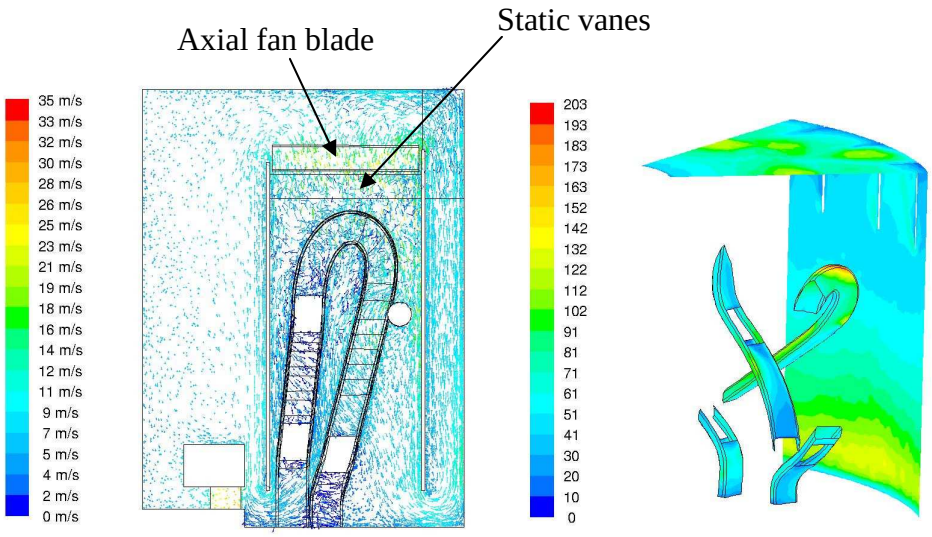

(a) (b)

Figure 7.20 - (a) velocity vector plot (b) contour of heat transfer coefficients (W/m^{2}K)

Unfortunately the windage loss calculated was very high (740W compared to 310W in the reference case) which makes this kind of configuration very unpractical.

7.2.7 Rotor end design

Rotor bar extensions

Despite the rotor bar extensions acting like a small centrifugal fan they also restrict the flow since they occupy a substantial volume under the end ring. Therefore a model having longer and thinner rotor bar extensions was analysed to predict any enhancements. It is important to note that this change will bring about an additional electric loss in the rotor bar extensions due to the additional Joule losses. However, these are expected to be negligible.

The model consisted of an exact replica of the base case model (8wafters measuring 50mm by 50mm) but with different rotor bar extensions. The cross-section of the new rotor bar extensions is shown in Figure 7.21. These new rotor bar extensions are 8mm wide by 30mm long whereas the base case model's rotor bar extensions were 10mm wide and 18mm long. The rectangular part of the cross-section was extended by a triangular part so as to decrease the eddies developing on the leading edges of the rotor bar extensions. CFD analysis of this model resulted in an improvement in the heat transfer coefficients for both the end windings and frame at an expense of 33% increase in windage loss (refer to Table 7-9).

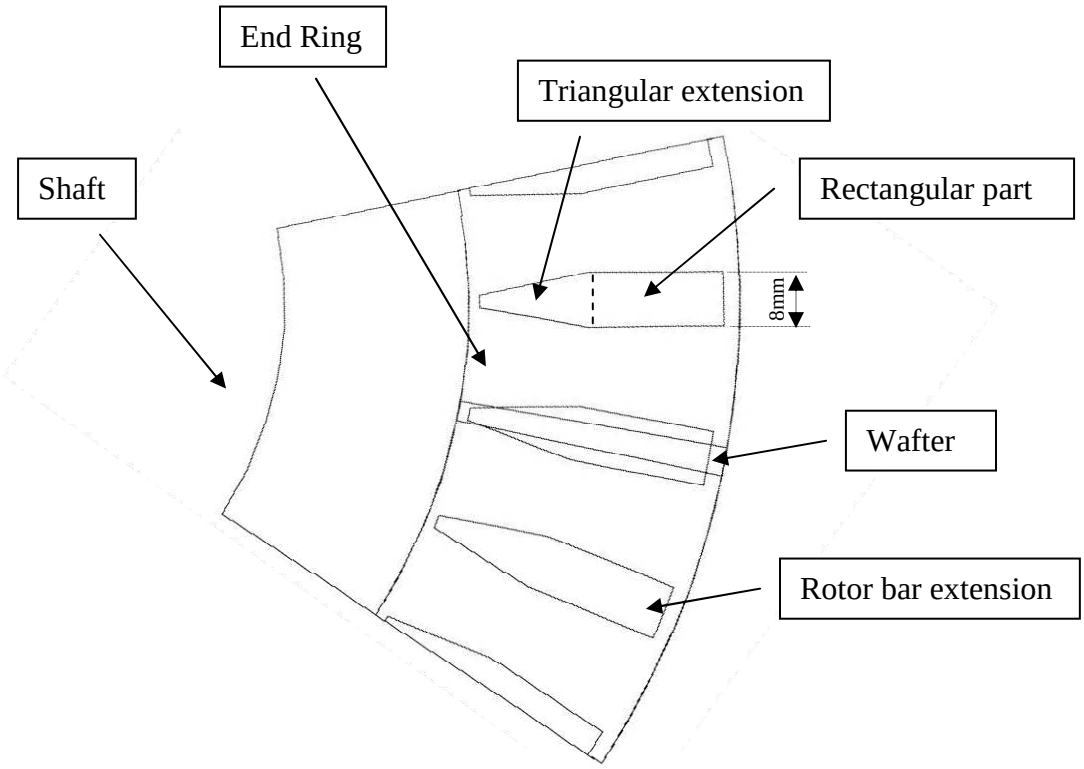

Figure 7.21 – Cross-sections of rotor bar extensions

Table 7-9 - Comparison of results of model with long rotor bar extensions to base case model.

Model	Windage Loss (W)	Total Thermal Resistance (K/W)	End Winding Thermal Resistance (K/W)	Frame Thermal Resistance (K/W)	End Winding htc (W/m^2K)	Frame htc (W/m^2K)
Long rotor bar extensions	412	0.500	0.343	0.107	80	32.7
Reference case.	310	0.559	0.298	0.262	75	28.6

End Ring

Since the wafters are a major source of windage loss in the end region, a series of configurations with an elongated end ring replacing the wafters were also investigated. The first in this series consisted of a model having the same rotor bar extension shown above and an elongated end ring as shown in Figure 7.22 (a). In this diagram the end ring is shown as hollow since the solid part was not modelled in CFD. The frame clearance and end shield clearance was also kept to a minimum in order to increase their proximity to the moving parts as much as possible.

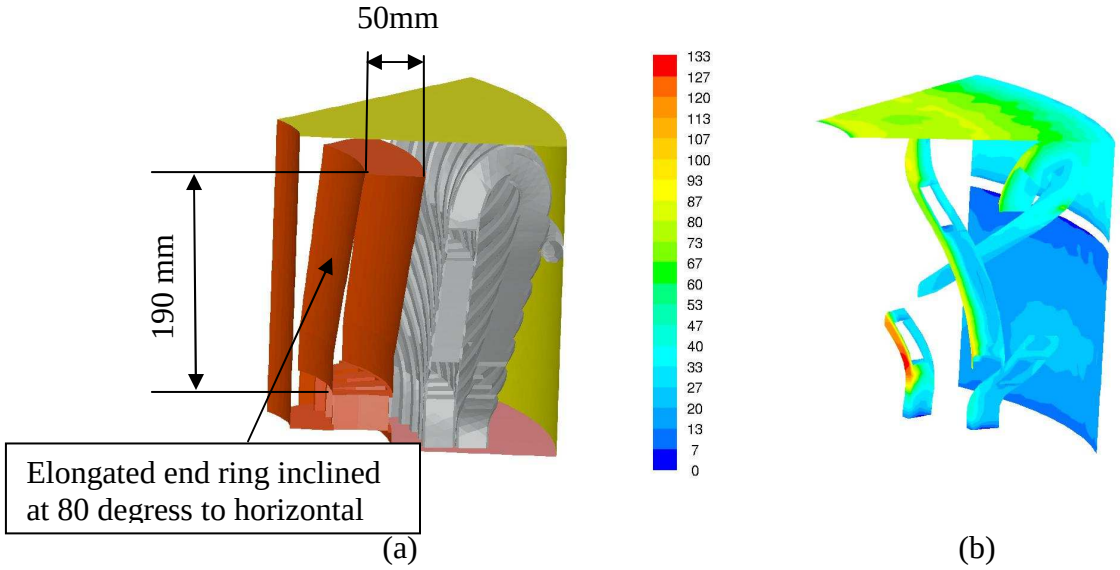

Figure 7.22 - (a) model with redesigned end ring
(b) contour of heat transfer coefficients (W/m^{2}K)

Referring to Table 7-10 which summarize the results it is clear that the windage power loss was significantly reduced (over 80%). The thermal resistances especially the end winding thermal resistance however experienced a substantial increase. The increase in the frame thermal resistance was due to the reduction in the frame surface area since there was an increase in the heat transfer coefficient at the frame surface. Such a change however has potential for further improvements.

Table 7-10 - Comparison of results of model with redesigned end ring to base case model.

Model	Windage Loss (W)	Total Thermal Resistance (K/W)	End Winding Thermal Resistance (K/W)	Frame Thermal Resistance (K/W)	End Winding htc (W/m^2K)	Frame htc (W/m^2K)
Redesigned end ring	55	0.906	0.612	0.294	37	37.8
Reference case.	310	0.559	0.298	0.262	75	28.6

Multiple changes

Since the windage loss in the model just analyzed was extremely low, eight small fins on the end ring surface opposite the end windings were introduced in order to enhance the heat transfer from the end windings. Additionally a screw pump between the end ring and the shaft was introduced to increase the air flow through the rotor bar extensions and the base of the end windings. Also the rotor bar extensions were aerodynamically shaped so as to improve their performance. The spacers adjacent to the end ring were protruded in the direction of the end ring serving as a static guide to the flow emerging from the rotor bar extensions. This is shown in Figure 7.23 (a).

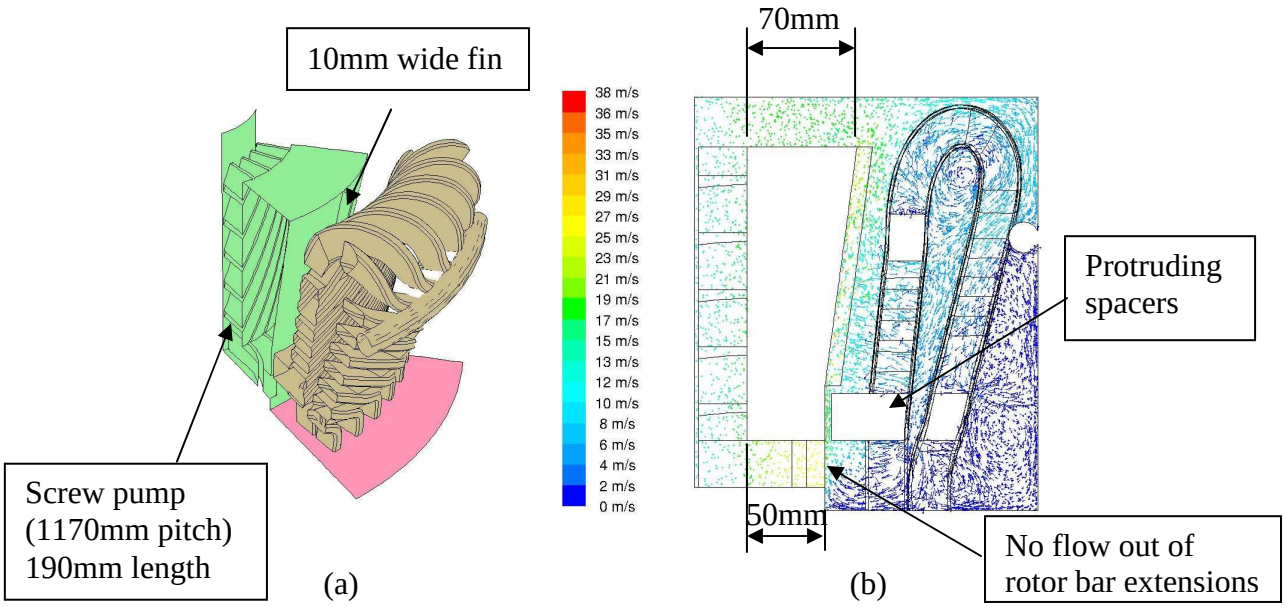

Figure 7.23 - (a) redesigned rotor end model (b) velocity vector plot

From the velocity vector plot in Figure 7.23 (b), it is clear that no fluid is emerging out of the rotor bar extensions since the fluid in this area is just swirling around with the rotor. This means that the screw pump and aerodynamically designed rotor bar extensions are not performing as intended. On further analysis of the pressure field in the end region (Figure 7.24(a)) it is evident that a high pressure is building up in the end windings area. The fluid in the rotor area is behaving like a rotating solid body with a radial pressure gradient due to the swirl.

Table 7-11 summarizes the results. The windage loss in this model is still low at a value of 121W (less than half the reference case model). The thermal resistance on of the end windings experienced a slight increase compared to the reference model. However this was compensated by a slight decrease in the thermal resistance of the frame (even though the frame surface area was substantially smaller than the reference case). The overall effect was a slight increase in the total thermal resistance of the end region. Figure 7.24 (b) shows that the main

improvement occurred in the area near the end shield where the heat transfer was enhanced in both the end windings and end shield. This is a positive aspect of this configuration since the tips of the end windings are usually the hottest.

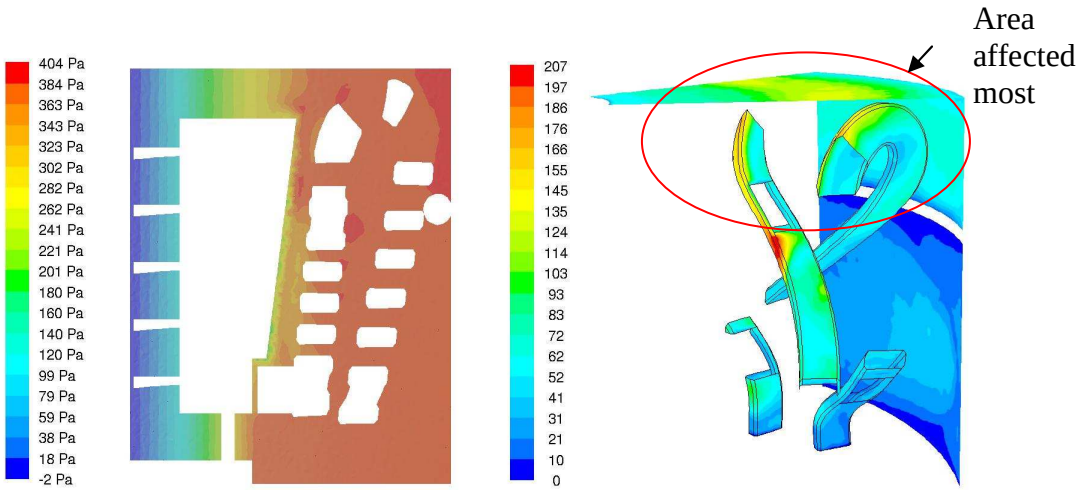

(a) (b)

Figure 7.24 - (a) pressure contour plot (b) contour of heat transfer coefficients (W/m^{2}K)

Table 7-11 - Comparison of results of model with multiple changes on rotor end to base case model.

Model	Windage Loss (W)	Total Thermal Resistance (K/W)	End Winding Thermal Resistance (K/W)	Frame Thermal Resistance (K/W)	End Winding htc (W/m^{2}K)	Frame htc (W/m^{2}K)
Multiple changes to rotor end	121	0.568	0.380	0.188	60	55
Reference case.	310	0.559	0.298	0.262	75	28.6

7.2.8 Fan in close proximity to the end shield.

The model created to investigate this configuration is shown in Figure 7.25 together with the resulting velocity vector plot. It is clear that the velocity circulating around the end windings is greater in magnitude compared to any of the previous models already investigated. Also a high speed jet of fluid emerges from the blades travelling over the end windings and continues behind the end windings, penetrating the end windings from the back side along the whole length of the end windings. This confirms the intended air flow pattern.

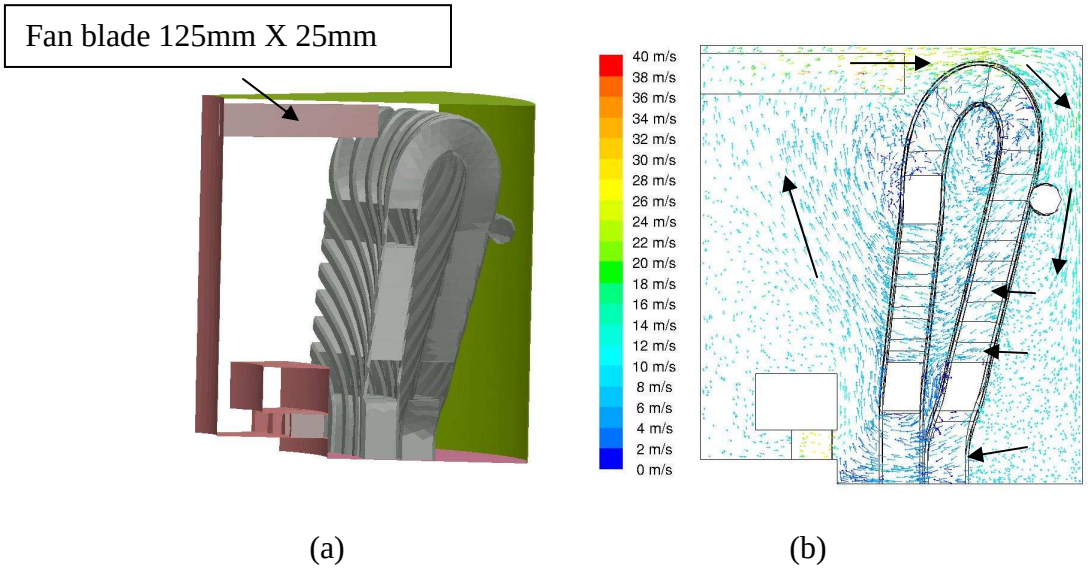

(a) (b)

Figure 7.25 - (a) model having upper fan (b) velocity vector plot

The summary of results (Table 7-12) shows that due to the high velocities in the vicinity of the end windings and frame, a heat transfer enhancement has been achieved. The total thermal resistance decreased by 33% compared to the reference case. This was mainly due to the reduction in the thermal resistance of the frame (65% reduction). The thermal resistance at the end windings experienced only a slight decrease; however the distribution of heat transfer coefficients on the

end winding (Figure 7.26) is far better than the reference case. This is because the heat transfer coefficients are more evenly distributed and the tips of the end windings, which usually suffer from hot spots, are being cooled much more effectively. The windage loss was slightly higher (19%) than the reference case.

Table 7-12 - Comparison of results of model with fan close to the end shield to base case model.

Model	Windage Loss (W)	Total Thermal Resistance (K/W)	End Winding Thermal Resistance (K/W)	Frame Thermal Resistance (K/W)	End Winding htc (W/m^2K)	Frame htc (W/m^2K)
Fan near end shield	368	0.376	0.283	0.093	79	108
Reference case.	310	0.559	0.298	0.262	75	28.6

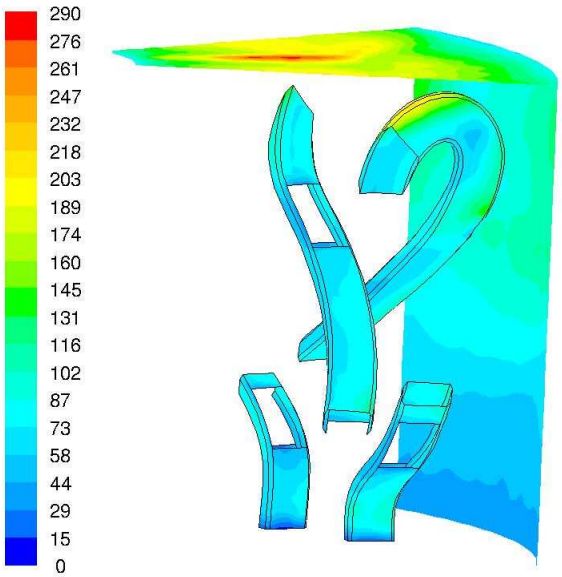

Figure 7.26 – Contour plot of heat transfer coefficients (W/m^2K) on end windings and frame of model with fan near end shield.

The only problem with such a configuration may be the reduction in cooling of the end ring due to the removal of the wafters. Apart from recirculating the air

enclosed in the end region, the wafters also act as cooling fins for the end ring. This problem may be eliminated by introducing a circumferential fin on the end ring as shown in Figure 7.27.

In order to check on cooling performance of the different configurations presented in this section, CFD models were generated having the end ring and the rotor bar extensions at the same temperature of the end windings. The results are shown in Table 7-13. The results clearly support the above discussion: the configuration having fan blades in the vicinity of the end shield and no fin on the end ring is the best option since the heat transferred from the end ring is of the same order as that obtained by the base case model and the heat transfer from the end windings is more than double that in the reference case.

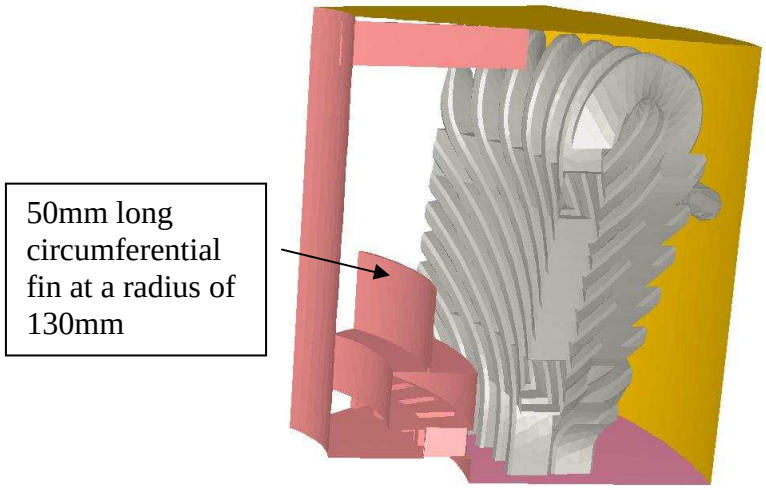

Figure 7.27 – Proposed fin on end ring to enhance heat transfer from end ring

Table 7-13 - Comparison of results of models with fan near the end shield with and without cooling fin on end ring to base case model.

Model	$Q_{\text{End Ring}}$ (W)	$Q_{\text{End Windings}}$ (W)	End Ring htc (W/m^2K)	End Winding htc (W/m^2K)
Reference case.	21	16	115	56
With fin	22	37	76	62
Without fin	27	36	67	63

7.3 Experimental verification

In order to verify the CFD analysis for the new configurations, an experiment was conducted with a configuration consisting of a fan mounted on the shaft near the end shield (Figure 7.28). Figure 7.29 compares values of the heat transfer coefficient on the end winding obtained through experiment and CFD. The CFD predictions were quite close to the experimental results implying that heat transfer enhancement designs may be investigated with confidence using CFD techniques.

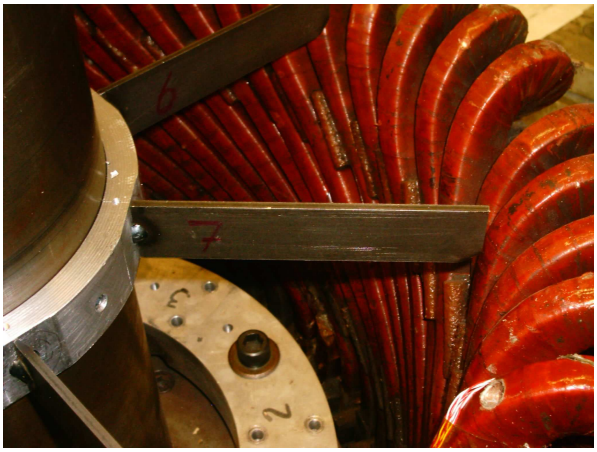

Figure 7.28 - Picture of experimental rig with fan near end shield (not shown)

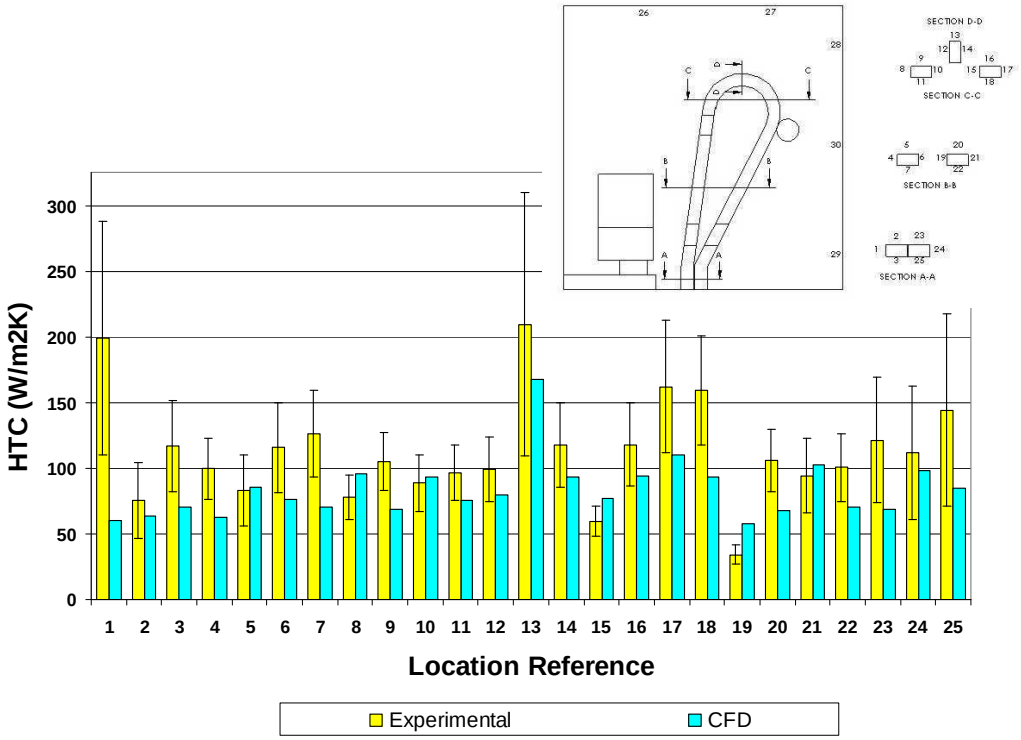

Figure 7.29 - Comparison of heat transfer coefficients on end winding

Figure 7.30 illustrates the distributions of heat transfer coefficients on the end windings for the reference case and the model having the shaft mounted fan in the vicinity of the end shield. The heat transfer coefficients are more evenly distributed in the latter model. This is in agreement with the CFD data.

The experimental area weighted average of the end winding overall heat transfer coefficient was estimated to be 103±27W/m^{2}K, while that of the frame was 90±30W/m^{2}K. This compares very well with the CFD results (Table 7-12) of 108W/m^{2}K and 79W/m^{2}K for the overall heat transfer coefficients of the frame and end winding respectively.

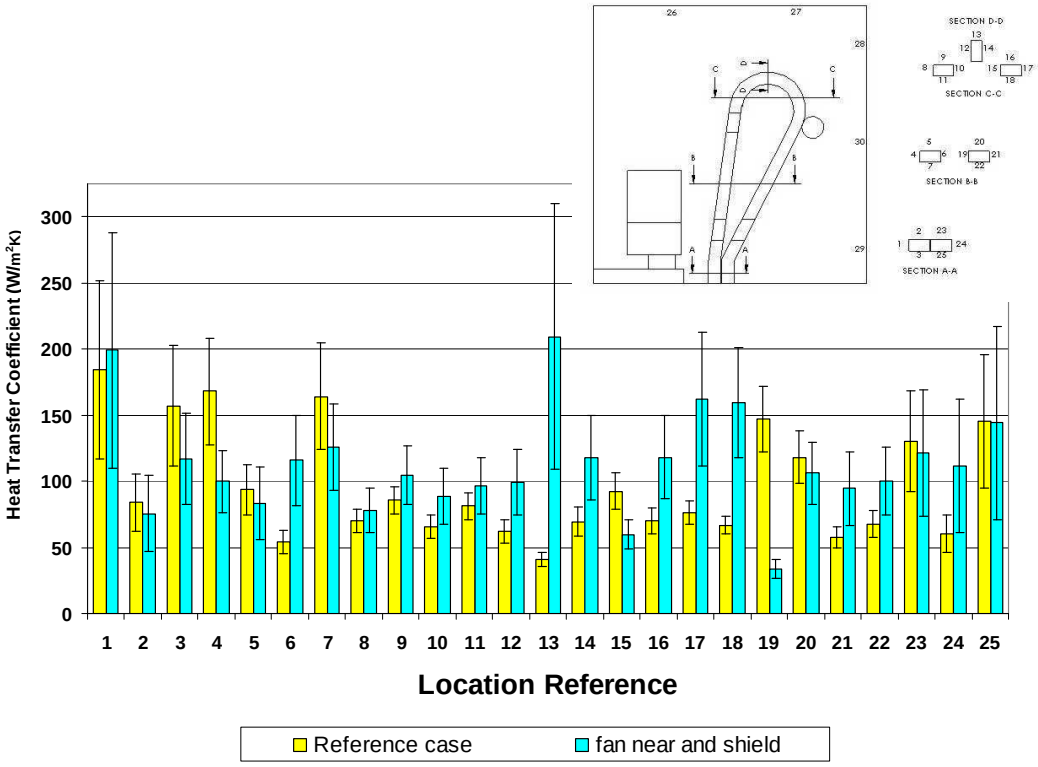

Figure 7.30 - Comparison of heat transfer coefficients on end ring between reference case and model with fan near end shield.

Using cotton tufts to visualize the flow, it was shown that the experimental velocity field matched the CFD predictions. The air was flowing over the end windings, behind the end windings and back to the centre of the end region penetrating the end windings from the back. The bulk of the flow was penetrating the base of the end windings. The rotor bar extension fan was not contributing anything in the formation of the major flow patterns. The flow present was highly swirling in nature which was also predicted in the CFD results.

7.4 Conclusions

Table 7-14 summarizes the main CFD results.

Table 7-14 – Summary of main results

Model No.	Windage Loss (W)	Total Thermal Resistance (K/W)	End Winding Thermal Resistance (K/W)	Frame Thermal Resistance (K/W)	End Winding htc (W/m^2K)	Frame htc (W/m^2K)
1	310	0.559	0.298	0.262	75	28.6
2	291	0.631	0.342	0.289	65	25.3
3	159	0.505	0.398	0.107	68	56.6
4	400	0.733	0.447	0.287	50	25.5
5	288	0.503	0.389	0.114	58	64.0
6	853	0.326	0.255	0.071	87	104.1
7	740	0.451	0.343	0.107	67	72.0
8	121	0.568	0.380	0.188	60	55
9	368	0.376	0.283	0.093	79	108

1. **Reference case – standard 50mm wafters.**
2. **Model employing deflector over wafters.**
3. **Long narrow shrouded wafters.**
4. **Long narrow shrouded wafters including static guide vanes.**
5. **Inclined long narrow shrouded wafters.**
6. **Blades behind end windings.**
7. **Axial fan over end windings.**
8. **Rotor end design changes.**
9. **Shaft mounted fan near end shield.**

The fact that the CFD predictions were quite reliable even though the end region experienced a substantial configuration change gives even better confidence in this

type of virtual design. This is an important outcome from this work since further development may take place without the extended need for experimentation, with a substantial reduction in development costs.

The configuration employing a shaft mounted fan in the vicinity of the end shield is the best method of cooling of the end region out of all the configurations investigated. However there remains scope for improvement in the end part of the rotor.

From this work the following general design suggestions were established:

- Keep rotating parts as close as possible to the shaft in order to minimise windage power loss.
- Place wafter blades near thermally critical surfaces (eg tips of end windings).
- The end winding consists of three main parts; the tips and the base offer very low resistance to fluid flow while the middle part offers a substantial resistance to fluid flow. If the fluid is allowed to flow around the end windings (without penetrating the middle part of the end windings) the velocity of the fluid is likely to be high everywhere. Therefore it is likely that heat transfer is enhanced around all the end windings.

Finally, a design compromise needs to be found so that the whole motor will not heat up above its critical value, keeping in mind that critical temperatures for different parts might be substantially different. In general a full thermal analysis

using resistance networks needs to be performed on every motor design, in order to predict which part needs more attention in terms of cooling performance. It might be the case that some parts need to be sacrificed to enhance heat transfer on other parts (such as reducing the cooling performance of the end ring so as to reduce the heat input in the end region).

8 Conclusions and Recommendations

This work contributes to the area of the thermal design of the end regions of TEFC induction motors. This is done by:

1. Establishing the nature of the complex flow field in the end region;
2. Establishing the features governing this flow field;
3. Highlighting the desirable and undesirable configuration changes which might be considered at the preliminary design stage;
4. Describing how CFD techniques may be used to model the end regions;
5. Presenting a new concept for thermal management.

8.1 Use of CFD to model end regions of TEFC machines

The majority of the work presented utilizes CFD techniques. A detailed description of the most suitable CFD methodology for modeling the end regions of TEFC induction motors was presented in Chapter 4. If these methods are followed the results can be sufficiently accurate. During this research, as the author gained experience, the results obtained increased in accuracy and successfully modelled the complex flows in the end regions of TEFC induction motors.

This research study has also shown that the CFD technique employed in this thesis is unable to resolve to an acceptable level of accuracy areas where the flow is turbulence driven. These include areas away from the pumping source (wafters)

particularly the area behind the end windings. However investigations into enhancement in heat transfer may be still investigated reliably.

8.2 Flow patterns

The flow fields predicted in all the CFD models analyzed agreed well with experimental results. This gave insight into what might be expected by each modification. It also assisted the author in deciding what further changes might bring about better heat transfer in the end region. During analysis of simplified models, it was found that when wafters are used on the end ring, the flow field becomes unstable as the wafter length increases and at a certain point the secondary recirculating flow behind the end windings changes direction. It emerged that if the wafter length approaches that of the end windings, the circulating air flow behind the end winding reverses direction and tends to flow over the tips of the end windings towards the base of the end windings.

8.3 New concept in thermal management

Data gathered from all the CFD models investigated gave a new insight into methods to improve the heat transfer from the end windings. Previously investigators have tried to increase the amount of air penetrating the end windings in order to achieve better cooling performance. However, a new concept for better thermal management of end region is now proposed in which the velocities in the vicinity of the end winding surfaces are maintained as high as possible. This is in order to achieve increased heat transfer coefficients on the end winding surfaces

without the need for the circulating air to penetrate through the end windings. Since the middle part of the end winding offers a high resistance to flow while the lower and upper parts of the end winding offer much less resistance, the aim is to circulate the air around the entire end winding by placing the wafters/blades appropriately. Additionally since the major recirculation in the region is the circumferential swirl, present due to the rotating nature of the electric motors, it plays a major role in the heat transfer characteristics of the region. This was clearly illustrated by analyzing a model employing a fan at the upper part of the end region. This increased the circumferential swirl behind the end windings and as a consequence both the end winding and frame heat transfer coefficients were improved.

8.4 Frame vs End Windings heat transfer coefficients

Both the frame and end winding heat transfer coefficients are important in TEFC induction motors. The total thermal resistance to heat flow from the end windings to the frame consists of two resistances in series. These are the convective thermal resistance from the end windings to the surrounding air and the convective thermal resistance from the air to the frame surface. In order to attain high heat transfer rates from the end windings to the frame, it is this total thermal resistance which needs to be minimized. Consequently, both convective thermal resistances need to be optimized.

If the end winding heat transfer coefficient is improved without a corresponding improvement in the frame heat transfer coefficient, the total thermal resistance will

decrease and therefore the heat transfer rate will also be increased. However, since the frame heat transfer coefficient is unaltered, the air surrounding the end windings will be hotter and therefore its cooling capacity is decreased. The total effect is likely to bring about only a slight improvement.

If on the other hand the heat transfer coefficient of the frame internal surface is improved, again the total thermal resistance will decrease. Therefore the heat transfer rate will also be increased as was experienced before. However, since the end winding heat transfer coefficient is kept the same, a decrease in the surrounding air temperature will result, which will further complement heat transfer.

Consequently, although it is important to enhance the heat transfer at both the end windings and frame surfaces, the latter is more important than the former. Suggestions on how the frame heat transfer can be enhanced are given in the section on future work at the end of this chapter. Again CFD modeling provides the most effective approach to investigate this.

8.5 General design suggestions

The following design guidelines are established from this work.

8.5.1 Rotating Surfaces

The radius of rotation of any rotating surface must be kept to a minimum in order to minimize the windage loss. Additionally it is better to position rotating surfaces

as close as possible to both the end windings and the endshield/frame in order to improve the local heat transfer coefficients on both surfaces.

8.5.2 Flow deflector / Air guides

The use of flow deflectors generally results in additional restrictions to the flow and they are thus not recommended for use in TEFC designs.

8.5.3 Endshield / Frame clearances

Usually the power rating and frame size of the motor dictate the endshield and frame clearances and not much can be done about them. However, if a complete design exercise is being conducted, then the following suggestions are worth considering at the design stage.

1. Small frame clearances create a blockage effect to the flow circulating around the end windings. However small frame clearances also give rise to higher velocities behind the end windings, thus increasing the heat transfer coefficients locally.

2. Large frame clearances substantially reduce the velocities behind the end windings, thus reducing the heat transfer coefficients on the end winding and frame surfaces. However large frame clearances also increase the cooling surface area of the frame. Therefore a balance has to be found between the two.

3. The overall end shield/frame heat transfer coefficient decreases with increasing end shield clearance. However the cooling surface area increases with increasing end shield clearance. Thus a balance should be sought between the two.

4. As a general rule, the end shield clearance and the frame clearance must be kept at the same order of magnitude.

8.5.4 Flow field

Air flow penetrating the middle part of the end windings must be avoided in order to decrease the pumping power required for circulation. On the other hand flow circulating around the end winding must be encouraged in order to improve the heat transfer characteristics of the end windings and frame.

Although these rules of thumb are suggested, it is recommended that a full CFD analysis is undertaken in order to ascertain any improvement in heat transfer. This is due to the complex geometry of the end region leading to a complex fluid flow field. In addition to this, a thermal model of the full motor needs to be analyzed in order to verify critical thermal paths and critical heat sources.

8.6 Future Work

Suggestions for future work include:

1. Analyzing other types of motors such as through ventilated models, which should be much simpler to analyze using CFD than confined flows present in TEFC designs.

2. Experiment with extended surfaces on the inside surface of the frame particularly behind the end windings.

3. Create a full lumped thermal network model to assist the CFD analysis.

4. Investigate the possibility to circulate the air enclosed in TEFC induction motors around the whole motor rather than keeping the flow confined to the end regions.

9 Appendices

9.1 Appendix A

Calibration Curves

9.1.1 Five hole probe calibration curves

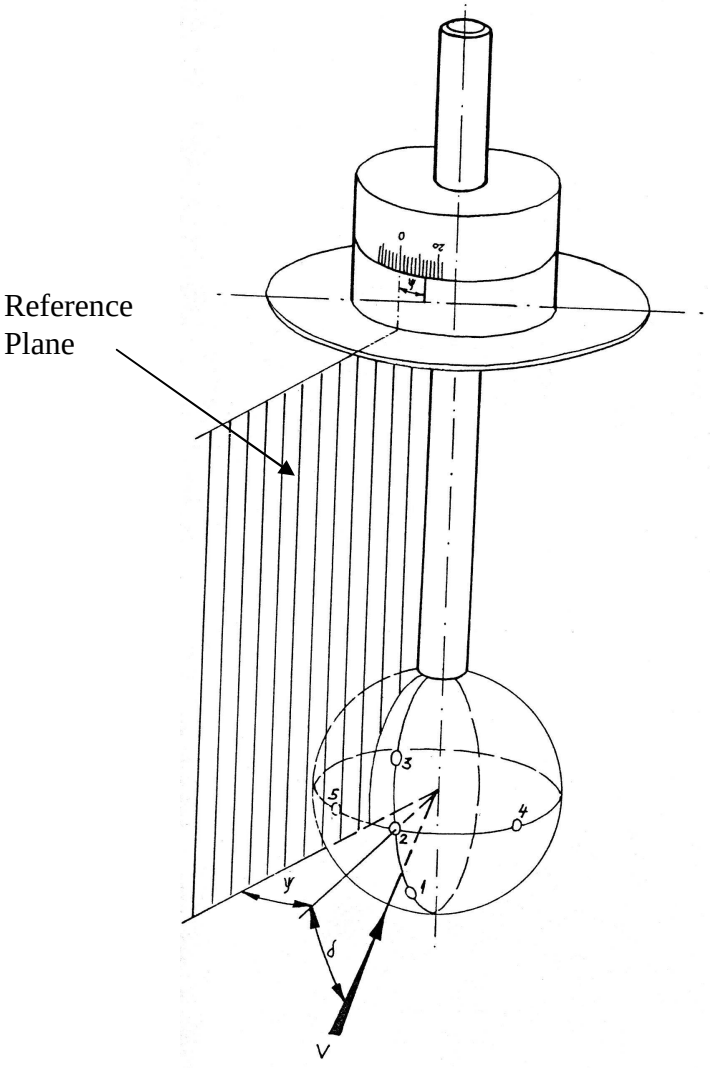

Figure 9.1 – Five hole probe used to measure velocities

The 5 hole spherical probe used to measure velocities is shown in Figure 9.1. It consists of dynamic hole in the front of the sphere (Hole No. 2), and 4 static holes equally spaced around the sphere.

The method used to measure the velocities is outlined below.

1. The probe is first aligned with the flow so that static holes 1 and 3 are in the plane of the flow and the differential pressure across static holes 4 and 5 (P_{45}) is zero. At this stage the angle Ψ is recorded.

1. The computer reads a sample of ten values of each of differential pressures across holes 2 and 4 (P_{24}) and holes 3 and 1 (P_{31}), averaged over one second at one second intervals. If the data exhibits a stable flow field (i.e. the scatter in the sampled data is small), the value of P_{24} and P_{31} are stored.

2. K_{1234} is then calculated by using the formula

$$K_{1234} = \frac{P_{31}}{P_{24}} \qquad (9.1)$$

3. K_{24} and the angle of attack δ are then interpolated from the calibration curve shown in Figure 9.2.

4. The velocity (v) is then evaluated using the formula

$$K_{24} = \frac{P_{24}}{\frac{1}{2}\rho v^2} \qquad (9.2)$$

Since the probe was out of calibration, it was necessary to recalibate it. This was done by means of a wind tunnel, where the probe was subjected to a series of tests so that a new calibration chart (refer to Figure 9.2) was produced. Each test was run at constant air speed while the angle of attack was varied by inclining the probe. Several tests were performed, each having a different speed and results were averaged to produce the calibration chart shown below.

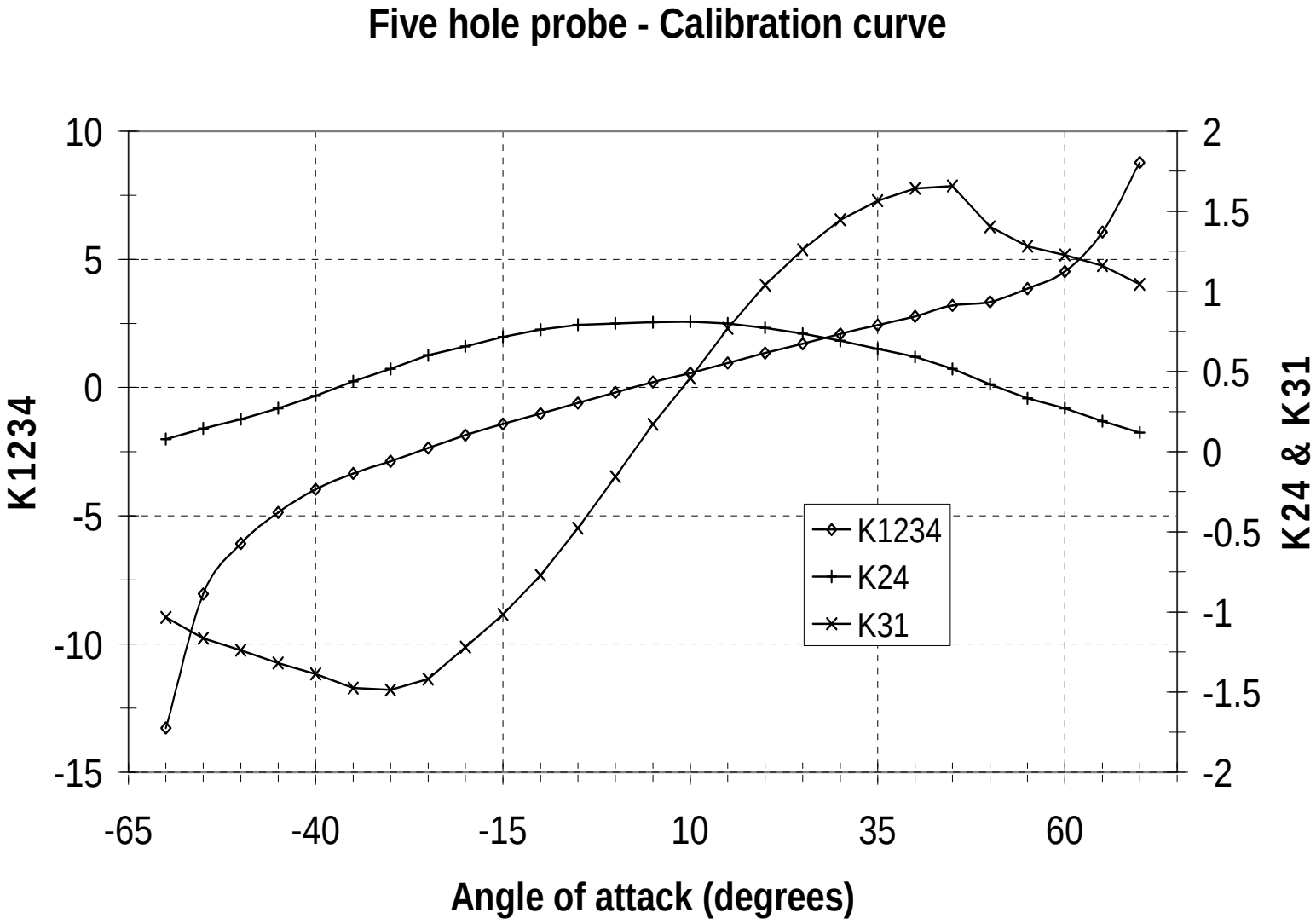

Figure 9.2 – Calibration curve for 5 hole probe

9.1.2 Calibration curve for beam used to measure Windage

Windage power loss was measured using a calibrated beam which deflects a distance proportional to the output torque of the driving shaft. The windage power loss was then evaluated by multiplying this torque by the speed of rotation of the rig. Figure 9.3 shows the calibration curve for the beam.

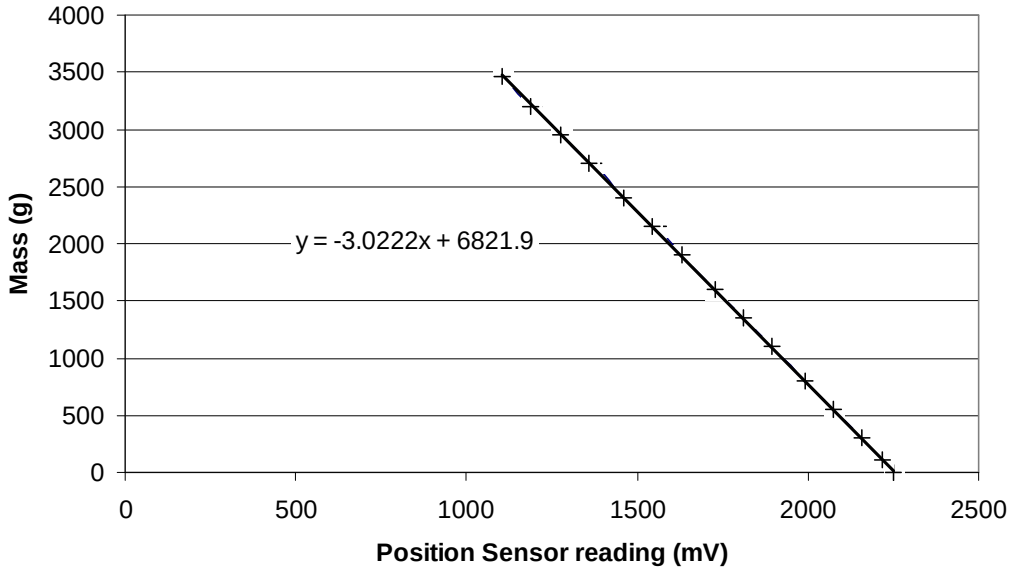

Figure 9.3 – Calibration curve for beam used to measure windage power loss

9.2 Appendix B

Guidelines for using CFD in end regions of electric motors.

In this section an overview of the methodology employed in all the CFD analysis performed in this thesis is described. It also serves as a guide to anyone wishing to start investigating fluid flow and heat transfer in the end region of electric machines using CFD techniques. It is hoped that this will accelerate the learning curve of this somewhat complex task.

9.2.1 Planning the Model.

In order to avoid disappointment, it is essential that the model is well planned. Things such as periodicity, boundary conditions, rotor/stator domains identification, steady/unsteady analysis, etc. should be considered at the early stage of the analysis.

9.2.2 Creating the Solid Model

When a plan is available, a solid model has to be developed. Although most CFD packages have their own solid modellers, according to the author's experience, using dedicated solid modelling software will save time by a factor of ten or more. Solidworks™ was used to create the solid models which were then exported to the grid generator using IGES standard.

While creating the solid model it is important to keep in mind that it is the air surrounding the solid parts which needs to be modelled. In special circumstances

(for example when analysing the temperature distribution on the end winding surfaces) the solids needs to be modelled too.

Do not include too much detail, especially detail which is much smaller than the length scale of the mesh. The reason behind this will be explained in the following section.

9.2.3 Generating the Mesh

The solid model is then imported in a mesh generation software. Usually the CFD package will come with its own mesh generator. This does not mean that other mesh generators may not be used. However it is important to check on compatibility. Fluent's mesh generation package, Gambit, was used to generate the meshes described in this work.

There are various types of meshes, the most commonly used nowadays are either structured meshes or unstructured meshes. From the author's experience Fluent v6 handles unstructured meshes better than structured ones. This may be due to Fluent using an unstructured solver. Additionally with an unstructured mesh it is more probable that the solution will be mesh independent. The disadvantage of an unstructured mesh however is the huge number of cells the mesh will contain when compared to a structured mesh of the same length scale. Having said this, the topology of the complex shaped end windings may leave no choice but to use only unstructured meshes. With the introduction of hex core meshes, where the mesh consists of hexagonal cells in the core regions and tetrahedral cells near the walls, a mesh consisting of a structured mesh surrounded by an unstructured mesh may

also be generated. This considerably reduces the mesh size, especially if the region has a lot of core space.

Since the flow in the end region is generally highly turbulent, wall functions must be applied to near wall cells. Consequently, a coarse mesh near the wall and a denser mesh elsewhere is desirable. This may be achieved in different ways but the easiest and fastest way to achieve such a mesh is to generate a course mesh everywhere and then divide each cell away from the wall using adaption techniques in the CFD solver package itself. This may be done in Fluent using inverse boundary adaption masks.

The next thing to look for when the mesh is generated is the quality of the mesh. It is important not to have too many scewed cells. Screwed cells can decrease the accuracy of the solution or even worse destabilise the solution making convergence next to impossible. The author suggests aiming at a skewness factor of less than 0.9. However, this is sometimes very difficult to achieve and thus a mesh having just a few cells with a skewness of not more than 0.96 is acceptable.

Another point worth mentioning is that CFD uses up a large amount of memory. As a result one should avoid generating meshes which are excessively fine, otherwise there will be no more room for adaption and post processing. It is worth remembering that all edges in the mesh are straight lines. Thus all curved lines in the solid model will be approximated by a series of straight lines having common nodes. Consequently, a balance must be found so that the mesh is not too course to

conserve as much as possible the solid features and on the other hand not too fine to satisfy the requirements of wall functions.

The last step to finalise the mesh is to group surfaces into meaningful groups and define the boundary type of these groups. Thus periodic, inlets, outlets, walls, interface, etc. surfaces must be defined before exporting the mesh to a format readable by the CFD solver.

9.2.4 Solving the model

The imported grid needs to be scaled to SI units. Thus if the model was created in millimetres this needs to be scaled down by a factor of one thousand.

The solution process then follows:

- Specifying equations to be solved
- Choosing a modelling technique
- Applying Boundary Conditions
- Setting up monitors
- Solve

Setting up the equations to be solved

The equations to be solved need to be specified. Hence, the energy equation is switched on if a heat transfer analysis is required. Also the turbulence model being employed is selected together with an appropriate near wall treatment. The

turbulent model and wall treatment employed are usually the standard k-ε model and standard wall functions respectively.

Choosing a Modeling technique

There are two ways in which rotating machines may be modelled. If a steady state (time averaged) solution is required the Multiple (Rotating) Reference Frame (MRF) technique is used otherwise if a time dependent solution is required, the Sliding Mesh (SM) technique is used. There may be times were a steady state solution does not exist (for example when an unstable flow field is present or the rotor stator interaction is strong), in these cases there is no option but to employ the sliding mesh technique.

The rotating reference frame technique includes the acceleration of the coordinate system in the flow equations so that the fluid is steady with respect to the rotating (non-inertial) reference frame. Therefore a steady state analysis may be performed.

The Multiple Reference Frame technique divides the domain into separate rotating reference frames so that the fluid flow is steady with respect to its rotating frame of reference. Thus a typical end region configuration will consist of two frames of reference, a stationary reference frame for the stator domain and a rotating reference frame for the rotor domain. It is important not to include any non-rotating walls in the rotating reference frame otherwise physically impossible solutions may crop up. Despite this technique being an approximation, it gives quite good results when the rotor stator interaction is weak.

If an unsteady model is required the sliding mesh technique must be employed. Here the rotating reference frame is physically rotating. This is done by rotating the rotor mesh by a certain amount in each time step. Thus the grid interfaces slide relative to one another. Since this technique requires a lot more computing resources than the MRF technique, it is usually used as a last resource when steady state analysis does not converge (indicating that most probably an unstable flow exists).

If using the sliding mesh technique an interface zone must be created within the CFD solver. This maps the interface wall of the rotating frame with the interface wall of the stationary zone. Otherwise an interior zone separates the rotating frame from the stationary frame in the MRF technique.

Applying Boundary Conditions

Before solving the CFD model, the boundary conditions (BCs) need to be set up. BC of the fluid zones need to be set up first. This involves setting the type of fluid being modelled (usually air) and type of reference frame being employed (either stationary, MRF or SM). If a MRF or SM is being used the rotational speed and axis of rotation need to be entered.

Following this BCs need to be set up to each individual wall. Usually momentum BC is stationary relative to the reference frame. If performing a heat transfer analysis the thermal BCs also need to be applied. Walls may be either adiabatic, at constant temperature or constant heat flux. Since the flow field in end region of electric machines is generally turbulent, the heat transfer coefficients in the region

are temperature independent. Therefore constant temperature BCs are usually the most reasonable choice since these are the easiest to solve.

If heat transfer by conduction in the coils needs to be investigated, then no boundary conditions needs to be attached to these walls. These walls are often referred to as coupled walls where the fluid's side of the wall is coupled with the solid's side.

Setting up monitors

Monitors are set up to assess convergence while the model is being solved. Residuals are monitored to assess solution stability. Residuals are a measure of the error in the solution. Residual history must show a steadily decreasing value.

Other monitors worth setting up are the windage loss and heat transfer from the end windings. The former is done by monitoring the moment coefficient on the moving walls while the latter is done through a surface integral monitor where an area weighted average of the heat flow out of the end windings is monitored.

It is worth emphasizing at this point that residual monitoring on its own is not enough as a convergence criteria.

Solving the model

The main process is that of solving the model. The majority of the time this is an extensive process. To speed up convergence the relaxation factors may be altered. Relaxation factors control the amount of change between successive iterations. Thus a relaxation factor (α) is defined as

$$\alpha = \frac{\phi' - \phi_n}{\phi_{n+1} - \phi_n} \qquad (9.1)$$

Where ϕ' is the adjusted value of ϕ to be used in the n+1 iteration.

For example if the solution exhibits instability, the relaxation factors may be decreased. On the other hand if the solution is stable but slow, the relaxation factors may be increased.

Other methods to aid convergence exist (e.g. algebraic multi-grid), however, the author never experienced the need to use them in this work.

9.2.5 Grid independency

The first thing to be done before starting to analyse the solution is to check whether the solution is grid independent. This may be done by solving a denser grid and comparing the two solutions. If the solutions are similar then one may assume that the solution is grid independent.

The fastest way to create a denser grid is to adapt the current grid. Adaption techniques are very useful if used intelligently. Adaption masks are useful for combining adaption registers. Thus in order to adapt only the cells which are not touching the walls (due to wall functions requirements), a complement boundary adaption register may be combined with a volume change register.

This process must be repeated until the solution is grid independent.

9.2.6 Post Processing

Here the solution is analysed using post processing tools like vector plots and contour plots. A great deal of information can be extracted if these tools are used properly. One of the most useful tools is the ability to create iso-surfaces. An iso-surface is an imaginary surface having a constant value of a particular variable (for example a surface having the same velocity magnitude). These iso-surfaces may in turn be clipped to other constant values of other variables. Vector plots and contour plots may then be plotted on these imaginary surfaces.

Apart from graphical analysis of results, numerical analysis of the results may be performed by using surface and volume integration tools. For example to calculate the overall heat transfer coefficient, the area weighted average surface integral of the heat transfer coefficient on the end windings surfaces is calculated.

9.2.7 Validation

Unlike Finite Elements Analysis applied to structures, CFD techniques have not yet obtained a high level of confidence. This is usually due to the turbulent nature of the flow. Therefore CFD models need to be validated against experimental data before more detailed analysis may be performed on them.

10 References

1 Huai, Y., Melnik, R.V.N. and Thogersen, P.B., 2003. Computational analysis of temperature rise phenomena in electric induction motors. Applied Thermal Engineering, Vol. 23, 2003. pp 779-795.

2 Mugglestone, J, 1998. End Region Cooling in an Electric Motor. PhD Thesis, University of Nottingham, October 1998.

3 Chin, Y.K., Nordlund, E. and Staton, D.A., 2003. Thermal Analysis – Lumped-Circuit Model and Finite Element Analysis. IPEC 2003, The sixth International Power Engineering Conference, Singapore, 27-29 November, 2003. pp 1019-1024.

4 Mellor, P.H., Roberts, D. and Turner, D.R., 1991. Lumped parameter thermal model for electrical machines of TEFC design. IEE Proceddings-B, Vol. 138, No. 5, September 1991. pp 205-218.

5 Di Gerlando, A. and Vistoli, I., 1994. Thermal networks of induction motors for steady state and transient operation analysis. ICEM 1994, Proceeding of the International Conference on Electrical Machines, Paris, September 1994, pp 452-457.

6 Staton, D, Pickering S and Lampard, D., 2001. Recent advancement in the thermal design of electric motors. SMMA 2001 Fall Technical Conference “Emerging Technologies for Electric Motion Industry”, Durham, North Carolina, 3-5 October 2001.

7 Boglietti, A., Cavagnino, A. and Staton, D.A., 2005. Induction Motors Thermal Models: A Parameter Sensitivity Analysis. IEEE Transactions on Inductrial Applications, Vol. 41, No. 3, May/June 2005. pp 756-763.

8 Rajagopal, M.S., Aswatha Narayana, P.A., Quadir, G.A. and Seetharamu, K.N., 2002. Numerical and Experimental Heat Transfer Studies on Totally Enclosed Fan Ventilated Machines. Electric Power Components and Systems, Vol. 30, No. 8, August, 2002. pp791-806.

9 Mugglestone, J., Lampard, D and Pickering S.J., 1998. Effects of end winding porosity upon the flow field and ventilation losses in the end region of TEFC induction machines. IEE Proceedings Electrical Power Applications, Vol. 145, No. 5, September 1998. pp 423-428.

10 Pickering, S.J, Lampard, D., Mugglestone, J., Shanel, M. and Birse, D., 1999. Using CFD In The Design Of Electric Motors And Generators. Computational Fluid Dynamics: Technical Developments and Future Trends, 13-14 December, 1999.

11 Mugglestone, J., Pickering, S.J and Lampard, D, 1999. Effect of geometric changes on the flow and heat transfer in the end region of a TEFC induction motor. IEE Conference Publication, No. 468, 1999. pp 40-44.

12 Liao, C., Chen,C-L. and Katcher, T., 1999. Thermal Management of AC Induction Motors Using Computational Fluid Dynamics Modeling. IEMDC 1999, IEEE International Electric Machines and Drives Conference, Seattle, Washington, 9-12 May, 1999.

13 Maynes, B.D.J., Kee, R.J., Tindall, C.E. and Kenny, R.G., 2003. Simulation of airflow and heat transfer in small alternators using CFD. IEE Proceedings Electrical Power Applications, Vol. 150, No. 2, March 2003. pp 146-152.

14 Shanel, M., Pickering, S.J. and Lampard, D.,2000. Application of Computational Fluid Dynamics to the Cooling of Salient Pole Electrical Machines. ICEM 2000, International Conference on Electrical Machines, Finland, 2000.

15 Farsane, K., Desevaux, P. and Panday, P.K., 2000. Experimental study of the cooling of a closed type electric motor. Applied Thermal Engineering, Vol. 20, 2000. pp 1321-1334.

16 Hay, N., Lampard, D, Pickering, S.J. and Roylance, T.F., 1995. Air flow and heat transfer over the ribbed surface of an externally cooled electric motor. Proceedings of the ASME-JSME Thermal Engineering Joint Conference, Vol. 1, 1995. pp 321-326

17 Toth, K., 1980. Examination of heat transfer conditions of finned motor case for shell-heated motors. Periodica Polytechnica, Electrical Engineering, Vol. 24, No. 3-4, 1980. pp 169-178

18 Roberts, T.J., 1969-70. Determination of the thermal constants of the heat flow equations of electrical machines. Proceedings IMechE, Vol 184, Part 3E, 1969-70. pp84-92.

19 Zautner, F.L., Feigel'man, I.I., Andrezheiko, M.M. and Borisovich, V.I., 1965. Optimum length of cooling vanes in the squirrel-cage rotor of explosion proof induction motors. Elektrotekhnika, Vol. 36, No. 7, 1965. pp 47-49.

20 Schubert, E., 1968. Heat Transfer Coefficients at End Windings and Bearing Covers of Enclosed Asynchronous Machines. Elektrie, Vol. 22, April 1968. pp160-162.(Translation ERA/IB 2846).

21 Pickering, S.J., Lampard, D, Hay, N. and Roylance T.F, 1998. Heat transfer in a through-ventilated induction motor. IEE Proceedings – Electrical Power Applications, Vol. 145, No. 5, September, 1998. pp 429-433

22 Hay, N., Lampard, D., Pickering, S.J. and Roylance, T.F., 1994. Heat transfer from stator-nd-windings of a low-voltage lap-wound electric motor. Proceedings of 10th international Heat Transfer conference, 1994, Vol. 3. pp 197-202.

23 Pickering, S.J., Lampard, D., Hay, N. and Roylance, T.F., 1995. Heat transfer from the stator end-windings of a low voltage concentric-wound induction motor., IEE Conference Publication, No. 412, 1995. pp 477-481

24 Takahashi, K., Kuwahara, H., Kajiwara, K. and Obata, T, 2002. Airflow and Thermal Conductance in a Totally Enclosed Induction Motor. Heat Transfer – Asian Research, Vol. 31, No. 1, January, 2002. pp 7-20.

25 Hay, N., Lampard, D., Pickering, S.J. and Roylance, T.F., 1993. Convection heat transfer correlations relevant to cooling situations in electric motors. American Society of Mechanical Engineers (Paper), 1993. pp 1-17

26 Oslejsek, O. 1972. The cooling of the end windings of small enclosed electric machines. Elektrotech Obzor, Vol. 61, No. 10. pp 548-556

27 Mugglestone, J, Pickering, S.J. and Lampard, D, 1999. Prediction of the heat transfer from the end winding of a TEFC strip-wound induction motor. Proc of IEMDC'99 IEEE International Electric Machines and Drives Conference, Seattle, USA, May 1999. pp 484-486.

28 Schleussinger, A, Weickgenannt, A. and Arndt, A, 2005. Heat transfer measurements on crossing banks of noncircular bars in cross flow. 6th World Conference on Experimental Heat Transfer, Fluid Mechanics, and Thermodynamics, Matsushima, Miyagi, Japan, 17-21 April, 2005.

29 Kline, S. J. and McClintock, F. A., 1953. Describing uncertainties in single-sample experiments. Mechanical Engineering, Jan. pp 3-8.

30 Versteeg, H and Malalasekra, W. An introduction to computational fluid dynamics: the finite volume method approach. Prentice Hall. ISBN: 0582218845.

31 Fluent™ 6.2 Users Guide.

32 Wang, P., Bai, X. S., Wessman, M. and Klingmann, J, 2004. Large eddy simulation and experimental studies of a confined turbulent swirling flow. Physics of Fluids, Volume 16, No. 9. pp 3306-3324.

33 Sun, Z., Lindblad, K., Chew, J. W. and Young, C.,2006. LES and RANS investigations into bouyancy-affected convection in a rotating cavity with a central axial throughflow. Proceedings of GT2006, ASME Turbo Expo 2006: Power for Land, Sea and Air, Barcelona, Spain, May 2006.

34 Micallef, C., Pickering, S. J., Simmons, K. and Bradley, K., 2005. Improvements in air flow in the end region of a large totally enclosed fan cooled induction motor. Proc. of IEMDC'05 IEEE International Electric Machines and Drives Conference, San Antonio, Texas, USA, May 2005.